Lucas F. M. da Silva   *Editor*

Materials Design and Applications IV

Springer

Advanced Structured Materials

Volume 168

Series Editors

Andreas Öchsner, Faculty of Mechanical Engineering, Esslingen University of Applied Sciences, Esslingen, Germany

Lucas F. M. da Silva, Department of Mechanical Engineering, Faculty of Engineering, University of Porto, Porto, Portugal

Holm Altenbach , Faculty of Mechanical Engineering, Otto von Guericke University Magdeburg, Magdeburg, Sachsen-Anhalt, Germany

Common engineering materials are reaching their limits in many applications, and new developments are required to meet the increasing demands on engineering materials. The performance of materials can be improved by combining different materials to achieve better properties than with a single constituent, or by shaping the material or constituents into a specific structure. The interaction between material and structure can occur at different length scales, such as the micro, meso, or macro scale, and offers potential applications in very different fields.

This book series addresses the fundamental relationships between materials and their structure on overall properties (e.g., mechanical, thermal, chemical, electrical, or magnetic properties, etc.). Experimental data and procedures are presented, as well as methods for modeling structures and materials using numerical and analytical approaches. In addition, the series shows how these materials engineering and design processes are implemented and how new technologies can be used to optimize materials and processes.

Advanced Structured Materials is indexed in Google Scholar and Scopus.

Lucas F. M. da Silva

Editor

Materials Design and Applications IV

 Springer

Editor
Lucas F. M. da Silva
Department of Mechanical Engineering
Faculty of Engineering
University of Porto
Porto, Portugal

About This Book

This volume of *Advanced Structured Materials* contains selected papers presented at the 4th International Conference on Materials Design and Applications 2022 (MDA 2022), held in Porto, Portugal, during July 7–8, 2022. The goal of the conference was to provide a unique opportunity to exchange information, present the latest results as well as to discuss issues relevant to materials design and applications. The focus is on fundamental research and application areas in the field of the design and application of engineering materials, predominantly within the context of mechanical engineering applications. This includes a wide range of materials engineering and technology, including metals, e.g., lightweight metallic materials, polymers, composites, and ceramics. Advanced applications include manufacturing of new materials, testing methods, multi-scale experimental and computational aspects. Approximately, 110 papers were presented by researchers from nearly 25 countries.

In order to disseminate the work presented in MDA 2022, selected papers were prepared which resulted in the present volume dedicated to *Materials Design and Applications IV*. A wide range of topics are covered resulting in 11 papers dealing with metals, composites, additive manufacturing, design, forming, and joining. The book is a state of the art of materials design and applications and also serves as a reference volume for researchers and graduate students working with advanced materials.

The organizer and editor wish to thank all the authors for their participation and cooperation, which made this volume possible. Finally, I would like to thank the team of Springer-Verlag, especially Dr. Christoph Baumann, for the excellent cooperation during the preparation of this volume.

August 2022   Lucas F. M. da Silva

Contents

Part V   Forming

Part VI   Joining

Part I
Metals

Chapter 1
Microstructure and Strength Properties of the Mg-Zn-Ca-Er Alloy Produced by Spark Plasma Sintering (SPS) Method

Sabina Lesz, Bartłomiej Hrapkowicz, and Małgorzata Karolus

Abstract In this work, a novel Mg-Zn-Ca-Er alloy was prepared. A spark plasma sintering (SPS) technique was used to produce samples from powders synthesized by mechanical alloying (MA). Sintering temperature of 583 K and holding time of 4 min were used. These parameters allow to obtain the appropriate densification and compaction in the produced samples. Before and after sintering, microstructural changes were investigated by X-ray diffraction (XRD) and scanning electron microscopy (SEM) methods. The results of density measurements, microhardness, and compression strength tests are presented. Analyses showed that amorphous structure was achieved by mechanical alloying for milling times exceeding 20 h. A substantial increase in hardness values with increasing the milling time up to 70 h was attributed to the particle size decrease, and strong plastic deformations occur. The mechanical properties that can be achieved using SPS of the Mg-Zn-Ca-Er alloy are promising. Mechanical test results displayed reasonable improvements in compressive strength with decreasing porosity of the samples. Fracture morphology of the Mg-Zn-Ca-Er is the characteristic for brittle crystalline materials.

Keywords Mg-Zn-Ca-Er alloy · MA · SPS · XRD · SEM method · Microhardness · Compression strength tests

1.1 Introduction

Apart from the obvious biocompatibility, one of the most important properties of biomaterials is high strength and fracture toughness. Metallic implants may be superior to polymeric or ceramic materials, thanks to their high values of mentioned properties. (Niinomi 2007) However, the materials mechanical properties, when superior

S. Lesz (✉) · B. Hrapkowicz
Department of Engineering Materials and Biomaterials, Silesian University of Technology, 18a Konarskiego Street, 44-100 Gliwice, Poland
e-mail: sabina.lesz@polsl.pl

M. Karolus
Institute of Materials Engineering, University of Silesia, 75 Pułku Piechoty 1A, 41-500 Chorzów, Poland

to the human bone, may cause problems due to the stress-shielding phenomenon. This process is ensued from Wolff's law, stating the bone rebuilds itself and strengthens its tissue according to the applied load. The opposite is also true and is known as osteopenia. (Frost 1994; Razavi et al. 2010) Fortunately, magnesium (Mg) excels in that matter among many metals possible to be used as biomaterials. Its properties are closely related to those of the human bone, making it an excellent choice for implant materials (Murty et al. 2003; Datta et al. 2011; Lesz et al. 2018, 2021; Hrapkowicz and Lesz 2019).

Nowadays, commonly used materials such as titanium (Ti) and stainless steel (SS) are usually bioinert materials, meaning they do not interact with surrounding tissues and do not take part in metabolic processes. On the other hand, magnesium is a bioactive material actively assisting various bodily functions via interacting with the physicochemical environment surrounding the implant. The bioactivity of magnesium means it can be used as a biodegradable material (Hermawan et al. 2010; Witte 2010; Datta et al. 2011). Bioinert materials are usually the base of permanent implants, and such solutions usually mean there is a need for a second surgery, to remove the implant after the bone had been stabilized. That is not the case with biodegradable implants. Due to their design and appropriate corrosion behavior, they degrade over time, supplementing the body and removing the potential risks of a re-operation, as they completely disappear after the healing process. It has been proven that Mg^{2+} ions promote bone growth and reduce the overall healing time. (Rude 1998).

Unfortunately, pure Mg has a considerable drawback of corroding too quickly in physiological environments. That issue can be addressed by carefully selecting appropriate alloying elements that can enhance its properties. One of the best alloying elements which improve a plethora of properties is zinc (Zn). It not only improves the overall mechanical properties but at the same time lowers the degradation rate of the alloy (Boehlert and Knittel 2006); at the same time, it is an important metabolic microelement, which has been proven to have a positive effect on bones. (Yamaguchi 2010; Jin et al. 2014) Another element with a beneficial influence on magnesium alloys is calcium (Ca). Ca causes brittleness in Mg alloys thus reducing the failure strain. It contributes to the alloy via solution and precipitation strengthening; moreover, it can act as a grain refining agent. However, Ca addition exceeding the solubility in Mg causes a sharp drop of corrosion resistance by forming Mg_2Ca phases, although at the same time it increases the hardness of the alloy. Hence, both corrosion resistance and hardness may be controlled by the Ca content. (Kirkland et al. 2010; Harandi et al. 2013; Chen and Thouas 2015) As it is biocompatible and osteoconductive, it is a very appropriate choice for biomaterials; however, its corrosion products are insoluble and generally unfavorable; thus, the Ca quantity should not be excessive. (Drynda et al. 2010) Other interesting alloying elements are rare earth elements (RE). They have been known to tremendously improve Mg alloys since the 1930s, although their effect on biomaterials is still being extensively researched. They are usually divided into two groups: light RE (La, Ce, Pr, etc.) and heavy RE (Gd, Dy, etc.). The main difference between the two is their solubility in Mg. While light REs have very limited solubility, they form stable intermetallic compounds

mainly located on grain boundaries, whereas the heavy group forms intermetallic phases and it is possible to keep them in a solid solution. They quickly react with alloys' "pollutants" such as H, O, F, and Cl. The products of these reactions may have detrimental effects on the human health and corrosion resistance, as such the alloys should be ideally free of impurities. They have been, however, already in use as biomedical materials. In general, all the rare earth elements indicated a strengthening effect and may promote corrosion resistance at lower concentrations. (Ashida et al. 1992; Hampl et al. 2013; Li et al. 2015; Liu et al. 2017).

Along mentioned materials, erbium (Er) seems to be attractive as compared to other materials. It is not that vastly researched as the other rare earth elements (in terms of their applications in the biomedical field), although its corrosion products seem to be only mildly or in negligible degree toxic. In the magnesium alloys, erbium may be used as an addition which considerably strengthens the material, both in terms of mechanical properties and corrosion resistance. Moreover, as it can be seen in the Mg-Er phase diagram, erbium is soluble in magnesium up to around ~ 3–4%.

The mentioned alloying elements have very different melting temperatures, thus making the casting process more difficult. A very good solution to that is using mechanical alloying (MA), which is a powder metallurgy technique utilizing metallic powders and milling them to obtain a homogeneous alloy without melting them. It is possible via solid solution diffusion which appears during high-energy milling. The advantages of said process are numerous, but the most viable are the cost decrease and high control over the process parameters and resulting alloys. Via MA, it is possible to synthesize homogeneous powdered alloys and control their microstructure, such as supersaturated solid solutions, non-equilibrium crystalline, and crystalline phases as well as amorphous structures (Schultz 1988; Suryanarayana 2001; Polmear et al. 2017).

It was reported that the amorphous alloys exhibit higher strength, ductility, and corrosion resistance as opposed to the crystalline alloys (Murty et al. 2003; Witte et al. 2005; Gu et al. 2009, 2010; Datta et al. 2011). Moreover, via appropriate alloying addition, it is possible to reduce the hydrogen evolution during the corrosion process resulting from the interaction with surrounding tissues and fluids (Nagels et al. 2003; Razavi et al. 2010; Datta et al. 2011). The amorphous materials are very tedious and extremely hard to prepare when manufactured by standard methods. The conditions needed for such a process encompass very rapid solidification and appropriate critical thickness of the material. Fortunately, while using MA, those concerns are negligible. Both size and structure of the obtained powder are very refined, and it is possible to obtain not only the amorphous structures but crystalline too, by carefully tailoring the process parameters (Schultz 1988; Suryanarayana 2001).

The obtained powders, however, need to be consolidated. Nowadays, the rapid growth of additive manufacturing opens many doors to the shaping of powder materials. As such, methods like selective laser sintering (SLS) or spark plasma sintering (SPS) are capable of manufacturing products and details hard to obtain via conventional means. In contrast to other consolidation techniques, SPS allows for rapid densification, even at lower temperatures, hence making it possible to retain amorphous or nano-crystalline structure even after the consolidation process (Mardiha

et al. 2019, 2022; Mohammadnejad et al. 2021). Although the main advantage of the SPS method is the capability of producing ultra-fine structures with a very small number of pores in the material (Orrù et al. 2009; Straffelini et al. 2013; Trapp and Kieback 2019). This is very crucial for Mg-based biomaterials, as pores may induce local galvanic corrosion, lowering the overall corrosion resistance considerably.

This paper aims to investigate the morphology and mechanical properties of the Mg-Zn-Ca-Er alloy, obtained via high-energy ball milling and sintered via the SPS method. Hence, the presented results encompass XRD phase analysis, compression strength, density, and porosity of the samples, as well as their microhardness.

1.2 Material and Methods

1.2.1 Material

High purity powders of magnesium, zinc, erbium (99.9 wt%), and calcium chunks (99.9 wt%) were used as the basic starting mixture with the desired composition of $Mg_{65-x}Zn_{30}Ca_4Er_x$, where $x = 1, 2, 3$ at.%. Powders were mixed in stainless steel cylinders in argon atmosphere. Ball-to-powder ratio was 10:1. The powder alloys were prepared via high-energy mechanical alloying (HEMA) process in high-energy dual shaker ball mill SPEX 8000D (Metuchen, USA). The process was carried out at room temperature, using 10-mm stainless steel balls for varying time with 0.5 h interval. (Lesz et al. 2018, 2021; Hrapkowicz et al. 2022).

The sintering process was performed via spark plasma sintering by FCT SPS HP D 25 (Frankenblick, Germany). Synthesized alloys were placed in a graphite die toolset with 10 mm inside diameter. The toolset was lined with a graphite foil to prevent the alloy from sticking to the toolset and facilitate the post-process extraction. The pressure applied was kept at 51 MPa. The samples were sintered at 583 K, 323 K/min heating rate, with 4 min holding time and cooled to the room temperature. The samples were sandblasted after the process to remove any remaining graphite foil.

1.2.2 Experimental Procedure

The X-ray phase analysis was performed with the Empyrean diffractometer (PANa-lytical, Almelo, the Netherlands) with Cu-Kα radiation and PixCell counter via the step scanning method in 10 to 150° 2θ angle range. The phases were identified with the High Score Plus PANalytical software (version 4.0, PANalytical, Almelo, The Netherlands) and the ICDD PDF4+2016 database (International Centre for Diffraction Data, Newtown Square, PA, USA).

Density assessment of the sintered samples was performed on the helium pycnometer Micromeritics AccuPyc II 1340 (Norcross, U.S.A.). To obtain statistically valid data, each sample was tested 50 times. Consequently, the porosities of the obtained samples were measured via following Eq. (1.1):

$$P = \left(1 - \frac{\rho_c}{\rho_a}\right) \cdot 100\%,\tag{1.1}$$

where P—porosity, ρ_c—calculated value of density, and ρ_a—absolute density of the sample.

The compression tests to assess the deformation behavior of the samples were performed on ZwickRoell Z100 testing machine (Ulm, Germany). Samples were cylindrical with base-to-height ratio of approximately 1:1.5. The microhardness test was performed on the FM700 Vickers hardness tester (Future-Tech, Tokyo, Japan) with 15 s dwell time and with a load of 50 gf (HV 0.05).

The morphology details of both powder and sintered samples were characterized via scanning electron microscope (SEM) SUPRA 25, Carl Zeiss (Jena, Germany), equipped with an energy-dispersive X-ray spectroscopy (EDS). The fractographic investigation was carried out on the samples after compression testing, to determine the character of fracture.

1.3 Results and Discussion

Depending on the erbium content (1–3 at.%), a transition state has been observed in the selected samples (Er_1 and Er_2) after 20 h of milling and (Er_3) after 30 h. It is characterized by higher degree of amorphous structure as compared to alloys milled for both longer and shorter times. It is a state, where transition phases start to form in the material, although the processes happening due to the mechanical synthesis are not yet completed.

Figure 1.1a shows the X-ray diffraction pattern (XRD) for Mg-based samples with varying Er addition (1–3 at.%). In the milled materials, the identified phases were as follows: Mg ($P6_3$/mmc), $MgZn_2$ ($P6_3$/mmc)$_2$, Ca_3Zn (Cmcm), Zn (P63/mmc), and Er (Fm3m). Figure 1.1b features the XRD patterns for the sintered samples. The phases identified were Mg ($P6_3$/mmc), MgZn, Mg_7Zn_3, Mg_2Zn_{11} (Pm-3), $MgZn_2$ ($P6_3$/mmc), Ca (Im3m), and SiO_2 (Pa-3).

Figure 1.2 represents the SEM micrographs. The morphology of the powders of the alloys with varying Er addition can be seen as (a)—Er_1, (b)—Er_2, and (c)—E_3. Analogously, in Fig. 1.2d–f, the surface of the sintered samples after compression strength can be seen. The morphology of the samples clearly indicates brittle fracture, with various cracks, both intra- and trans-crystalline. Alongside the micrographs, Table 1.1 features the EDS results. The powder alloys results are in line with the assumed nominal compositions; on the other hand, the sintered samples compositions vary slightly, with the most prominent change in the Er_3 sample.
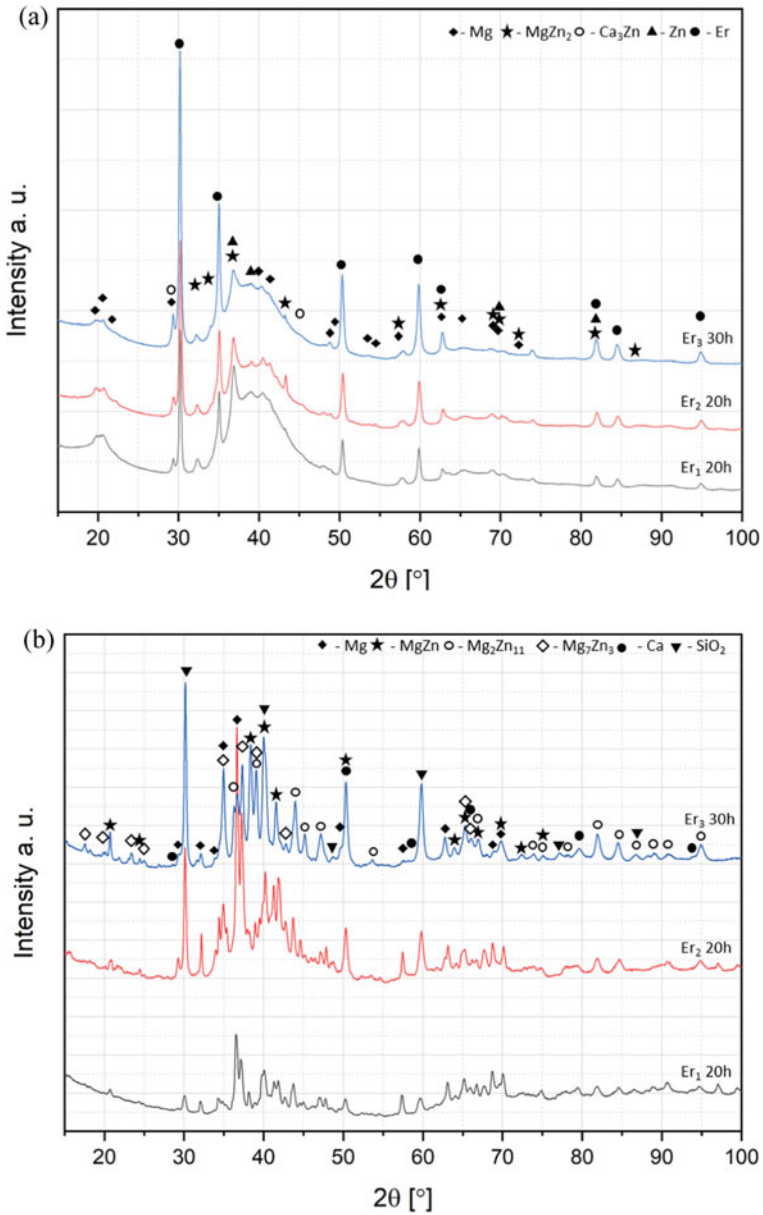
Fig. 1.1 XRD analysis graphs for Mg-Zn-Ca-Er samples with varying Er addition (1–3 at.%), **a** before sintering and **b** after sintering
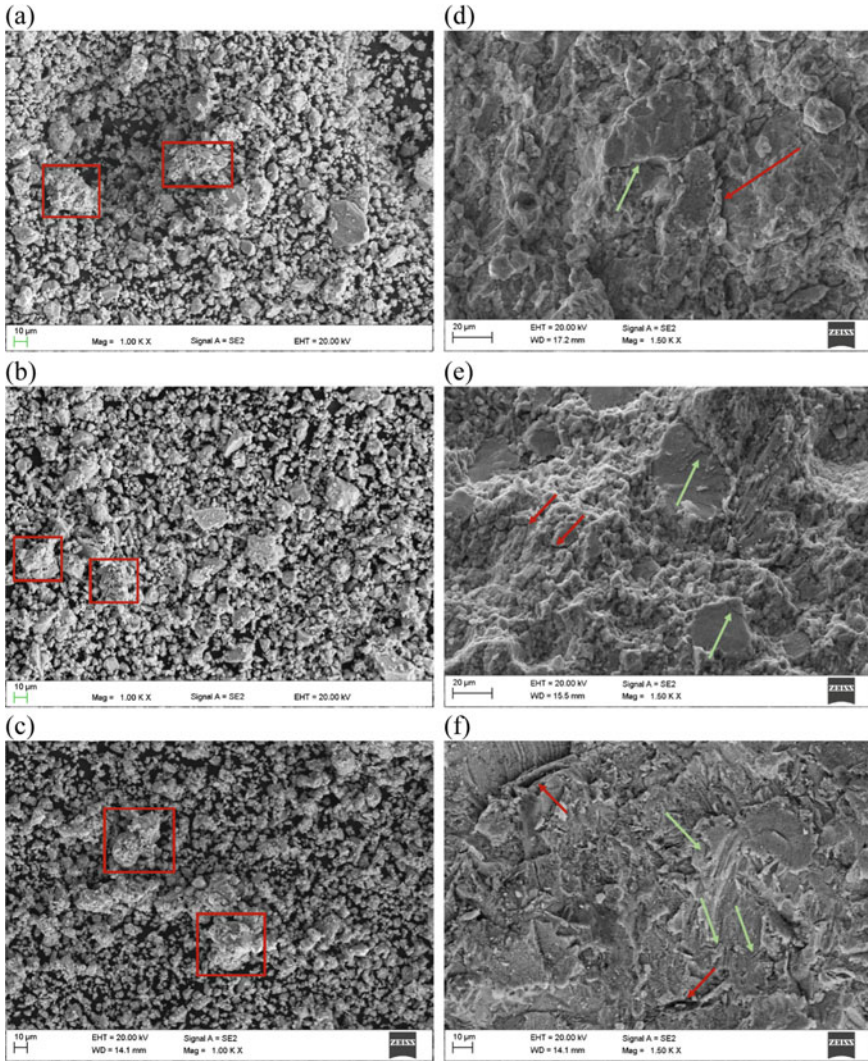
Fig. 1.2 SEM micrographs of the Mg-Zn-Ca-Er samples. Samples are presented side by side, before (**a–c**) and after sintering (**d–f**). **a**, **d**—$Mg_{65}Zn_{30}Ca_4Er_1$, **b**, **e**—$Mg_{64}Zn_{30}Ca_4Er_2$, and **c**, **f**—$Mg_{63}Zn_{30}Ca_4Er_3$. The "corncob" structure is marked with the red rectangle. Trans-crystalline cracks are marked with red arrows, and inter-crystalline cracks are marked with green arrows

Figure 1.3 shows a graph featuring the compression strength of all samples. The highest value of 325 MPa was obtained by the Er_3 sample, 310 MPa for Er_2, and 299 MPa for Er_1. The values clearly indicate an increasing tendency, proportional to the erbium content. Consequently, the hardness measurement performed on the

Table 1.1 EDS results comparison for Mg-Zn-Ca-Er samples, before and after sintering

Element (at.%)	Powder samples			Sintered samples		
	Er_1	Er_2	Er_3	Er_1	Er_2	Er_3
Mg	67.0	65.2	62.1	62.0	61.0	53.4
Zn	28.2	28.5	30.9	32.8	29.7	39.0
Ca	3.8	4.1	3.9	3.9	7.4	4.2
Er	1.0	2.2	3.1	1.3	1.9	3.4

samples features a similar tendency with results averaging from 272 HV, 313 HV, and 330 HV, for Er_1, Er_2, and Er_3 samples, respectively.

The density was measured for all the samples averaging from 50 measurements, with the highest value of 3.4098 g/cm^3 for the Er_3 sample, 3.2617 g/cm^3 for Er_2, and 3.2569 g/cm^3 for Er_1; see Table 1.2. The porosity calculated from the density with the use of Eq. (1.1) was 4% for Er_1, 3% for Er_2, and 0.1% for Er_1. Table 1.2 and Fig. 1.3 feature comparative results of density, porosity, and hardness (alongside compressive strength).

The XRD pattern in Fig. 1.1a features the phases formed at the milling phase of the work. Some degree of amorphousness can be discerned by the wide peak located between 35 and 45°, although microcrystalline phases are clearly visible, and they mainly refer to pure elements such as Zn and Er. Moreover, Mg(x) is a solid solution, where x = Zn, Ca, and Er. However, $MgZn_2$ phase can be discerned as well. Its presence is beneficial to the alloy due to its thermal and mechanical stability. The $MgZn_2$ phase has been described as a good strengthening and stabilizing factor (Andersson et al. 2010; Singh et al. 2010; Xie et al. 2013).
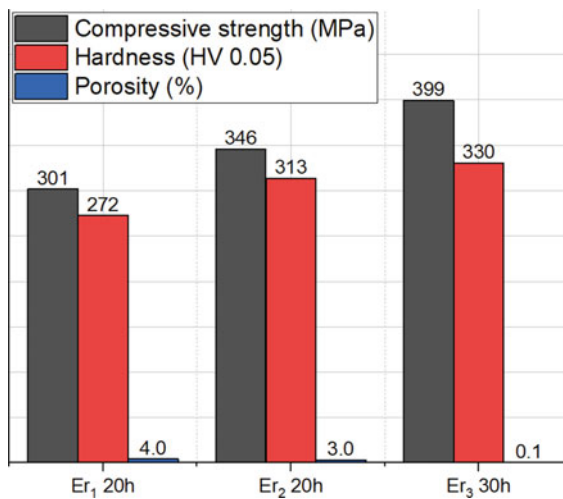
Fig. 1.3 Compressive strength, hardness, and porosity comparison for Mg-Zn-Ca-Er samples

Table 1.2 Comparison of density, porosity, and hardness values for Mg-Zn-Ca-Er samples

Sample	Density (g/cm^3)	Porosity (%)	Hardness (HV 0.05)	Compressive strength (MPa)
Er$_1$ 20h	3.2569	4.0	272	299
Er$_2$ 20h	3.2617	3.0	313	310
Er$_3$ 30h	3.4098	0.1	330	325

Compressive strength added for clarity

Figure 1.1b, on the other hand, presents the phases formed after the sintering. The wide peaks visible in the former graph are much smaller, with much clearer crystalline peaks. During the sintering process, the thermal and mechanical processes caused the $MgZn_2$ phase to disappear into different intermetallic phases: $MgZn$, Mg_7Zn_3, and Mg_2Zn_{11}. The SiO_2 phase has not been formed during the process, and it is a residue from sandblasting the samples after the SPS process. This is to remove the remnant graphite foil.

The micrographs of both powders and sintered specimens are visible in Fig. 1.2. Figure 1.2a–c features the powdered alloys, as the milling time of the alloys was quite similar (20–30 h), there are not any discernible traits between them. All three alloys bear semblance in terms of powder particle size and distribution. Small, equiaxial powder particles can be seen, along bigger agglomerates. This is caused by cyclical fracturing and cold welding of the particles in the mill. The usual, for mechanical synthesis, plate structure is absent, although structures resembling a "corncob" can be seen (Fig. 1.2a–c, marked with red rectangles). Those are characteristics for a brittle material, as strong fragmentation occurring during the process causes a significant rise in hardness, straining the material, hence breaking it apart into smaller particles. The mentioned "corncob" is created when finer, thus harder, particulate embeds itself in softer, bigger agglomerates (Jurczyk 2003; Hrapkowicz et al. 2022).

In Fig. 1.2d–f, the surfaces of the sintered samples are shown. The fractures visible in the micrographs were caused by the compression tests and are brittle for all specimens. No porosity can be seen in the fractures, although slight cracks of both inter- (see the green arrows in Fig. 1.2d–f) and trans-crystalline (see the red arrows in Fig. 1.2a–c) type are present. Alongside SEM, EDS tests were conducted; their results are presented in Table 1.1, for both powders and sintered specimens. The results vary slightly between powder and sintered specimen, and they may be an indicator of phase changes occurring during the sintering process, although the changes are not that considerable as far as the Er is concerned.

Figure 1.3 features the results from performed compression tests, where the compressive strengths obtained were 299, 310, and 325 MPa for Er_1, Er_2, and Er_3 samples, respectively. The increase in compressive strength could be attributed to the decreasing porosities of the samples (Er_1—4%, Er_2—3%, and Er_3—0.1%). Both porosity and the microhardness are related to the resulting strength of the samples. It can be clearly seen that the porosity of the samples decreases, while the compressive strength of the sintered specimens indicates an increasing tendency, the microhardness is proportional, i.e., it has a rising tendency as well.

1.4 Conclusions

Based on the results of the structure analysis, density, and compressive strength of the Mg-Zn-Ca-Er alloys, it can be concluded that:

- The alloys have been successfully synthesized by MA and sintered via SPS method. The powders obtained feature some degree of amorphous structure with microcrystalline phases. The structure changes considerably during the sintering process, transforming into crystalline material and changing its phase composition.
- The density of the sintered samples is comparable (3.25–3.41 g/cm^3) and is like that of a human bone. The same can be said about mechanical properties of the sintered samples, as their compressive strength (299–325 MPa) is comparable to the bone properties. The mechanical properties are strictly related to the microhardness of the samples (272–330 HV).
- After the sintering process, the obtained porosity is very small (0–4%), and along the decreasing porosity hardness, the compression strength rises accordingly.
- The morphologies of the samples are characteristic for brittle and crystalline materials. SEM micrographs feature cracks of inter- and trans-crystalline origin.

References

Andersson M, de Boissieu M, Brühne S et al (2010) Electronic and structural properties of Laves-phase MgZn2 of varying chemical disorder. Phys Rev B—Condens Matter Mater Phys 82. https://doi.org/10.1103/PHYSREVB.82.024202

Ashida T, Tsubakino H, Nozato R (1992) Precipitation in Mg-11 mass% Li-10 mass% Zn alloy. J Jpn Inst Light Met 42:797–803. https://doi.org/10.2464/JILM.42.797

Boehlert CJ, Knittel K (2006) The microstructure, tensile properties, and creep behavior of Mg–Zn alloys containing 0–4.4 wt.% Zn. Mater Sci Eng A 417:315–321. https://doi.org/10.1016/J.MSEA.2005.11.006

Chen Q, Thouas GA (2015) Metallic implant biomaterials. Mater Sci Eng R Rep 87:1–57. https://doi.org/10.1016/J.MSER.2014.10.001

Datta MK, Chou DT, Hong D et al (2011) Structure and thermal stability of biodegradable Mg–Zn–Ca based amorphous alloys synthesized by mechanical alloying. Mater Sci Eng, B 176:1637–1643. https://doi.org/10.1016/J.MSEB.2011.08.008

Drynda A, Hassel T, Hoehn R et al (2010) Development and biocompatibility of a novel corrodible fluoride-coated magnesium-calcium alloy with improved degradation kinetics and adequate mechanical properties for cardiovascular applications. J Biomed Mater Res A 93:763–775. https://doi.org/10.1002/JBM.A.32582

Frost HM (1994) Wolff's Law and bone's structural adaptations to mechanical usage: an overview for clinicians. Angle Orthod 64:175–188. https://doi.org/10.1043/0003-3219

Gu X, Zheng Y, Cheng Y et al (2009) In vitro corrosion and biocompatibility of binary magnesium alloys. Biomaterials 30:484–498. https://doi.org/10.1016/J.BIOMATERIALS.2008.10.021

Gu X, Zheng Y, Zhong S et al (2010) Corrosion of, and cellular responses to Mg–Zn–Ca bulk metallic glasses. Biomaterials 31:1093–1103. https://doi.org/10.1016/J.BIOMATERIALS.2009.11.015

Hampl M, Blawert C, Silva Campos MR et al (2013) Thermodynamic assessment and experimental study of Mg–Gd alloys. J Alloy Compd 581:166–177. https://doi.org/10.1016/J.JALLCOM.2013.07.042

Harandi SE, Mirshahi M, Koleini S et al (2013) Effect of calcium content on the microstructure, hardness and in-vitro corrosion behavior of biodegradable Mg-Ca binary alloy. Mater Res 16:11–18. https://doi.org/10.1590/S1516-14392012005000151

Hermawan H, Dubé D, Mantovani D (2010) Developments in metallic biodegradable stents. Acta Biomater 6:1693–1697. https://doi.org/10.1016/J.ACTBIO.2009.10.006

Hrapkowicz B, Lesz S, Karolus M et al (2022) Microstructure and mechanical properties of spark plasma sintered Mg-Zn-Ca-Pr alloy. Metals 12:375. https://doi.org/10.3390/MET12030375

Hrapkowicz B, Lesz ST (2019) Characterization of Ca 50 Mg 20 Zn 12 Cu 18 Alloy. Arch Foundry Eng 19:75–82. https://doi.org/10.24425/AFE.2018.125195

Jin G, Qin H, Cao H et al (2014) Synergistic effects of dual Zn/Ag ion implantation in osteogenic activity and antibacterial ability of titanium. Biomaterials 35:7699–7713. https://doi.org/10.1016/J.BIOMATERIALS.2014.05.074

Jurczyk M (2003) Mechaniczna synteza. Wydaw. Politechniki Poznańskiej

Kirkland NT, Birbilis N, Walker J et al (2010) In-vitro dissolution of magnesium-calcium binary alloys: clarifying the unique role of calcium additions in bioresorbable magnesium implant alloys. J Biomed Mater Res B Appl Biomater 95:91–100. https://doi.org/10.1002/JBM.B.31687

Lesz S, Hrapkowicz B, Karolus M, Gołombek K (2021) Characteristics of the Mg-Zn-Ca-Gd alloy after mechanical alloying. Materials 14:226. https://doi.org/10.3390/MA14010226

Lesz S, Kraczla J, Nowosielski R (2018) Structure and compression strength characteristics of the sintered Mg–Zn–Ca–Gd alloy for medical applications. Arch Civ Mech Eng 18:1288–1299. https://doi.org/10.1016/J.ACME.2018.04.002

Li J, Tan L, Wan P et al (2015) Study on microstructure and properties of extruded Mg-2Nd-0.2Zn alloy as potential biodegradable implant material. Mater Sci Eng C Mater Biol Appl 49:422–429. https://doi.org/10.1016/J.MSEC.2015.01.029

Liu W, Wang J, Jiang G et al (2017) The improvement of corrosion resistance, biocompatibility and osteogenesis of the novel porous Mg–Nd–Zn alloy. J Mater Chem B 5:7661–7674. https://doi.org/10.1039/C7TB00920H

Mardiha P, Bahrami A, Mohammadnejad A (2019) Towards a high strength ductile Ni/Ni3Al/Ni multilayer composite using spark plasma sintering. Sci Sinter 51:401–408. https://doi.org/10.2298/SOS1904401M

Mardiha P, Bahrami A, Mohammadnejad A (2022) An investigation on the microstructure, interface, and mechanical properties of spark plasma sintered Ni/Ni-Ni3Al/Ni compound. J Mater Eng Perform 31:1163–1169. https://doi.org/10.1007/S11665-021-06227-9/FIGURES/12

Mohammadnejad A, Bahrami A, Tafaghodi Khajavi L (2021) Microstructure and mechanical properties of spark plasma sintered Nanocrystalline TiAl-xB composites (0.0 <x<1.5 at.%) containing carbon nanotubes. J Mater Eng Perform 30:4380–4392. https://doi.org/10.1007/S11665-021-05773-6/FIGURES/13

Murty BS, Datta MK, Pabi SK (2003) Structure and thermal stability of nanocrystalline materials. Sadhana 28(1):23–45. https://doi.org/10.1007/BF02717124

Nagels J, Stokdijk M, Rozing PM (2003) Stress shielding and bone resorption in shoulder arthroplasty. J Shoulder Elbow Surg 12:35–39. https://doi.org/10.1067/MSE.2003.22

Niinomi M (2007) Recent research and development in metallic materials for biomedical, dental and healthcare products applications. Mater Sci Forum 539–543:193–200. https://doi.org/10.4028/0-87849-428-6.193

Orrù R, Licheri R, Locci AM et al (2009) Consolidation/synthesis of materials by electric current activated/assisted sintering. Mater Sci Eng R Rep 63:127–287. https://doi.org/10.1016/J.MSER.2008.09.003

Polmear I, StJohn D, Nie J-F, Qian M (2017) Novel materials and processing methods

Razavi M, Fathi MH, Meratian M (2010) Microstructure, mechanical properties and bio-corrosion evaluation of biodegradable AZ91-FA nanocomposites for biomedical applications. Mater Sci Eng A 527:6938–6944. https://doi.org/10.1016/J.MSEA.2010.07.063

Rude RK (1998) Magnesium deficiency: a cause of heterogenous disease in humans. J Bone Miner Res 13:749–758. https://doi.org/10.1359/JBMR.1998.13.4.749

Schultz L (1988) Formation of amorphous metals by mechanical alloying. Mater Sci Eng 97:15–23. https://doi.org/10.1016/0025-5416(88)90004-3

Singh A, Rosalie JM, Somekawa H, Mukai T (2010) The structure of β1 precipitates in Mg-Zn-Y alloys. Philos Mag Lett 90:641–651. https://doi.org/10.1080/09500839.2010.490049

Straffelini G, Nogueira AP, Muterlle P, Menapace C (2013) Spark plasma sintering and hot compression behaviour of AZ91 Mg alloy. 27:1582–1587. https://doi.org/10.1179/1743284710Y.0000000007

Suryanarayana C (2001) Mechanical alloying and milling. Prog Mater Sci 46:1–184. https://doi.org/10.1016/S0079-6425(99)00010-9

Trapp J, Kieback B (2019) Fundamental principles of spark plasma sintering of metals: part I—Joule heating controlled by the evolution of powder resistivity and local current densities. 62:297–306. https://doi.org/10.1080/00325899.2019.1653532

Witte F (2010) The history of biodegradable magnesium implants: a review. Acta Biomater 6:1680–1692. https://doi.org/10.1016/J.ACTBIO.2010.02.028

Witte F, Kaese V, Haferkamp H et al (2005) In vivo corrosion of four magnesium alloys and the associated bone response. Biomaterials 26:3557–3563. https://doi.org/10.1016/J.BIOMATERIALS.2004.09.049

Xie YP, Wang ZY, Hou ZF (2013) The phase stability and elastic properties of MgZn2 and Mg4Zn7 in Mg–Zn alloys. Scripta Mater 68:495–498. https://doi.org/10.1016/J.SCRIPTAMAT.2012.11.034

Yamaguchi M (2010) Role of nutritional zinc in the prevention of osteoporosis. Mol Cell Biochem 338:241–254. https://doi.org/10.1007/S11010-009-0358-0

Part II
Composites

Chapter 2
Coir and Hop Fibres: Tensile Characterization and Comparison Between Fibres from Distinct Climates

J. Aguirar, J. Rocha ⓘ**, L. Queijo, and J. E. Ribeiro** ⓘ

Abstract The human behaviour has significantly affected the climate. Because of that, the pursue of new alternatives for non-renewable materials has increased. In that scenario, the use of natural fibre to substitute synthetic ones in composite materials has also increased. In this work, two types of natural fibres from different regions and climates were evaluated and compared. The evaluated fibres were Coir from Brazil and Hop from Portugal and also were evaluated two different extraction methods for the hop batches, boiling in NaOH and maceration in water. To evaluate the composite mechanical characteristics, seven tensile tests were performed in each fibre batch, according to ASTM C 1557-14—Standard Test Method for Tensile Strength and Young's Modulus of Fibres, and the average tensile strength for each one was calculated. The highest value of ultimate tensile strength was brought by the hop extracted with the boiling in NaOH method and resulted in an average of 16 MPa.

Keywords Green composite · Natural fibre composites · Tensile strength

2.1 Introduction

The effect of human behaviour on global changes is undeniable. The agenda of sustainable development has been widely in focus trying to find ways to continue with the socio-economic development in a more conscious way.

J. Aguirar · J. Rocha · L. Queijo · J. E. Ribeiro (✉)
Polytechnic Institute of Bragança, C. Sta. Apolónia, 5300-253 Bragança, Portugal
e-mail: jribeiro@ipb.pt

J. Aguirar
e-mail: juliaaguiar@alunos.utfpr.edu.br

J. Rocha
e-mail: jrocha@ipb.pt

L. Queijo
e-mail: lqueijo@ipb.pt

J. E. Ribeiro
CIMO, C. Sta. Apolónia, 5300-253 Bragança, Portugal

At the beginning of the 1990s, the concept of Ecological footprint was developed by Mathis Wackernagel and William Rees, which measured the human demand on the biosphere (Wackernagel and Galli 2007). Since then, the global concern with carbon emissions and greenhouse effects has increased. In 1997, the Kyoto protocol was signed aiming to reduce the emission of greenhouse gases (Protocol 1998). All that leads to sustainable development and intense research targeting the use reduction of non-renewable materials, such as petroleum-based plastics and substituting them for renewable materials.

The challenge of substituting these materials is huge, that is why extensive research of natural sources is necessary. Nowadays, natural fibres are increasingly gaining space as an alternative to synthetic fibres and the technological development involved in the expansion of these materials is directly connected with consumers demands and expectations.

The use of natural plant fibres can be traced back more de 10.000 years. They were used about 8.000 B.C, in the Middle East and China, for textiles. In about 650 B.C., the Babylonians used it for burial purposes (Mwaikambo and Mwaikambo 2006), and over time, the plant fibres were always present.

Faruk et al. (Faruk et al. 2012) called this century the cellulosic century because of the vast number of renewable plant resources for products that are being discovered. The natural fibres are usually residues from primary processing of agricultural materials (Zhao et al. 2022), and all over the world, there is a huge variety of plant residues with potential to be used as natural fibres.

In addition to the growth region, other parameters have influence in the characteristics of the fibres, as the sowing time (Hall et al. 2013) and the sowing density (Bueno 2018), if there is an irrigation system. Many of these parameters are being explored, but the research still is a little restrict to some types of fibres that are more common, as flax (Graupner et al. 2021; Kandemir et al. 2021), hemp (Hall et al. 2013; Colomer-Romero et al. 2020), jute (Arulmurugan and Venkateshwaran 2019), sisal (Ekundayo 2019) and Coir (Tan et al. 2021; Bui et al. 2008; Majid 2011).

In industry, the natural fibres isolated have no huge application, so they are combined with different matrices to create composites. These can be polymeric matrices, cement matrices or other types that are being widely studied for different applications as natural fibre composites (NFC).

The NFCs already have a space in the commercial markets for value-added products, especially in the automotive sector. Although to achieve other markets, NFCs need to ensure high-quality performance, serviceability, durability and reliability standards (Faruk et al. 2012). That is why, the natural fibre research is increasing.

Some types of NFCs have already been widely studied and are already used in the industry, for example, the flax yarns that were accepted and established in the high-price segment and used in a hybrid composite with glass fibres used in prototypes of leaf springs of a narrow-gauge railroad (Graupner et al. 2021).

There are hemp fibres being studied for bio-composites with epoxy matrix, evaluating the difference between different epoxy resins (Colomer-Romero et al. 2020) and comparisons between different fibres and different weight percentages in the composites (Yun et al. 2022).

It is also used as an insulating material for the automobile industry, evaluating noise reduction, sound absorption, thermal resistance, biodegradability, antibacterial and antifungal characteristics. The use of light-weighted, green, environmentally friendly and biodegradable fibres as insulating materials provided comparable acoustic properties and thermal resistance with the commercial insulating materials (Cai et al. 2021). Hop bine fibres have already been used in the paper industry (Haunreiter et al. 2021). The coir fibre has been used for lightweight vehicle applications (Tan et al. 2021).

As seen before, natural fibres have a huge potential for usage, mainly as composite reinforcement. For that reason, this work aims to characterize different types of natural fibres in different regions of the world. The Coir was brought from Brazil and is also widely produced in India, which is the biggest producer in the world. The Hop was produced in Bragança, Portugal, but is also widely produced in many other countries such as the United States and Germany.

This work is proposed to characterize some mechanical properties of coir and hop natural fibres and compare the obtained results.

2.1.1 Natural Fibres

The natural fibres can be classified according to their sources. They can be animal fibres that are generally comprised of proteins. Mineral fibres are mainly occurring fibre or slightly modified fibre processed from minerals, or plant fibres that can be extracted from different parts of the plats, such as bast, leaf, seed, fruit or stalk (Saxena et al. 2011).

Coconut fibre/Coir. The coconut fibre, also called Coir, is extracted from the drupe of the coconut tree, Cocos nucifera, that is from the Palm family, Arecaceae. There are two types of coconut fibres, the brown and the white ones. The brown fibres are extracted from the mature coconut, and they are thick, are strong and have high abrasion resistance. The white fibres are extracted from the immature coconut, and they are smoother and finer than the brown ones but are also weaker (Ekundayo 2019). The coconut fibre is composed of hemicellulose, cellulose and lignin in percentages as shown in Table 2.1.

Hop fibre. The Hop fibre is extracted from the hop plant, Humulus lupulus, a member of the family Cannabaceae, the same as hemp. The Hop plant is mostly grown for its flower and after its harvesting the plant is cut and considered waste.

The Hop fibre is composed of cellulose, lignin and ash as shown in Table 2.2.

Table 2.1 Coir chemical composition (Faruk et al. 2012)

Fibre	Cellulose (wt%)	Hemicellulose (wt%)	Lignin (wt%)
Coir	32–43	0.15–0.25	40–45

Table 2.2 Hop chemical composition (Bredemann 1944)

Fibre	Cellulose (wt%)	Hemicellulose (wt%)	Lignin (wt%)
Hop	84 ± 1.6	6.0 ± 0.2	2.0 ± 0.1

2.2 Experimental Procedure

2.2.1 Hop Fibre Extraction Method

The hop fibres were extracted using two different methods, boiling in NaOH and maceration in water and were named Hop 1 and Hop 2, respectively.

The first method was based on Bredemann (Fiore et al. 2015) procedure. The fibres were extracted from random medium plants, with no distinguishment between what part of the bast was. The samples were boiled in a 0.35% NaOH solution for 1.5 h to separate the bark from the nucleus. Succeeding, the bark was boiled in a 2% NaOH solution, washed with tap water and dried at a temperature of 70 °C without any positioning of the fibre.

In the second method, the fibres were also extracted from random medium plants, with no distinguishment between what part of the bast was. The samples were submerged in water until the bark comes off. The water was renewed three times to reduce de Ph variation.

2.2.2 Specimen Manufacturing

The Coir was bought from a Brazilian industry that sells brown coconut fibres for gardening. The samples were untangled from the fibre tangles, Fig. 2.1. As the objective was to compare the two types of fibres, the coir was chosen to have almost the same thickness, 1 mm. After being chosen, they were cut 9 mm in length.

The samples of hop fibre, extracted as described before, also from tangles, Fig. 2.2, were also chosen to have thickness close to 1 mm and cut with 9 mm in length.

The fibres were weighted in a 4 decimal Laboratory Weighing Balance (ADA model 210/C). The mean masses are presented in Table 2.3.

After the mass evaluation, the samples were prepared for the tensile test. The samples were fixed in paper supports with masking tape, Fig. 2.3, according to ASTM C1557, and identified with LC for the first hop batch, LE for the second hop batch and C for the coir batch and numbers from 1 to 8. Figure 2.2 sample, for example, is the first sample of the second hop batch.

All the samples have the same gauge length, 4 mm.

Fig. 2.1 Coir tangled fibres

(a)   (b)

Fig. 2.2 **a** Hop 1 tangle, **b** Hop 2 tangle

Table 2.3 Mean masses, standard deviation

Sample	Mean mass (g)	σ
Coir	0.0170	0.004454
Hop 1	0.013825	0.003913
Hop 2	0.0048	0.00033

Fig. 2.3 Sample example

2.2.3   Tensile Test

After that, the samples were tested in a universal test machine, Shimadzu Autograph AGS-X 10Kn, with a constant deformation velocity of 5 mm/min.

For each batch were made 7 samples, tested following the ASTM C 1557-14— Standard Test Method for Tensile Strength and Young's Modulus of Fibres.

2.3   Results and Discussion

The test machine returned the dislocation in millimetres, the force in newtons and the time in seconds. With this information and the gauge length, the stress and strain were calculated. The graphs were plotted and are presented in Figs. 2.4, 2.5 and 2.6.

The significant variability of the results between the samples of the same batches is due the difficulty of tensile test on single lignocellulosic fibres. Many factors have influence in the results, as test parameters and conditions, plant characteristics as the source and age of the plant, the processes of fibre extraction and the presence of defects (Fiore et al. 2015; Liu et al. 2009). As some of these parameters could not be controlled, it is not possible to determine what is the source of the variation.

To compare the behaviour between the three batches the average stress–strain curve was determined for each material. In Fig. 2.7 is presented a comparison between the three average stress–strain curves.

Based on the stress–strain curves, Young's modulus was calculated for each sample and its values and standard deviation are presented in Table 2.4.

The values of the Coir Young's modulus are considerably smaller than the values that are seen in the literatures, that are around 4–6 GPa (Majid 2011; Biswas et al. 2013). In these works, the researchers had control in the extraction method, something that was not possible here because the fibres were bought already extracted.
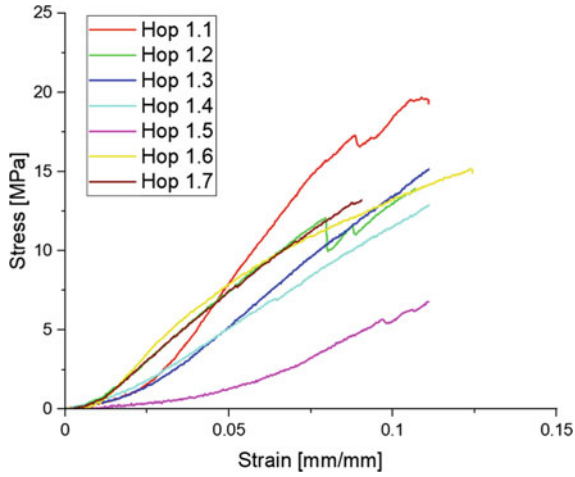
Fig. 2.4 Hop 1: stress versus strain
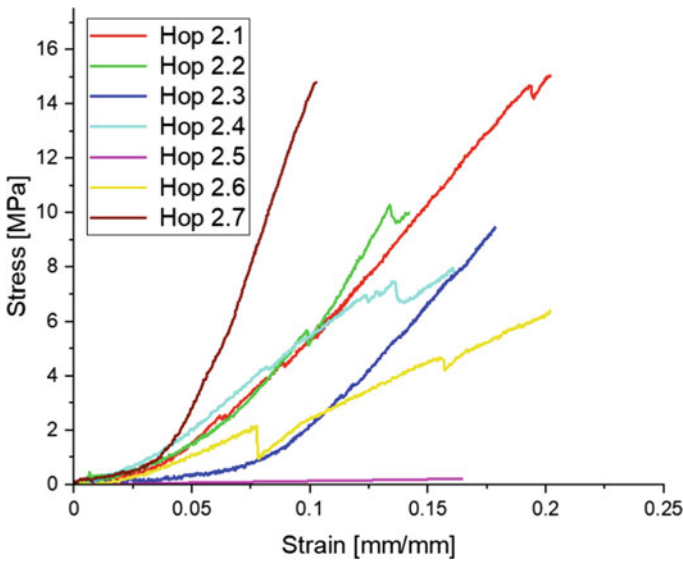
Fig. 2.5 Hop 2: stress versus strain

The exact extraction method that was used to these fibres is not known. These fibres were bought from a gardening supply's company so, probably the integrity of the fibre was not the main concern in the extraction. This is one of the possible explanations for the difference in Young's modulus.

Fig. 2.6 Coir: stress versus strain
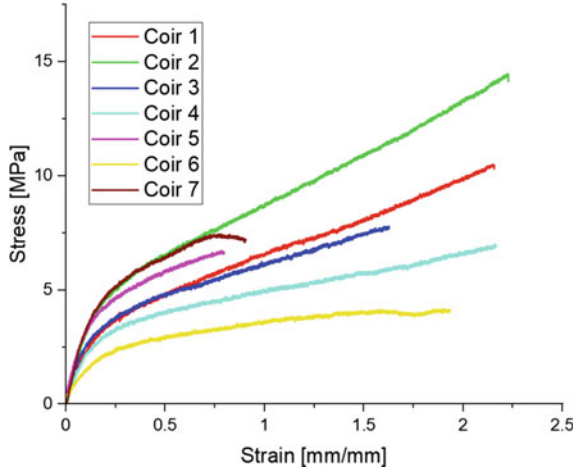
Fig. 2.7 Comparison: stress versus strain (average)
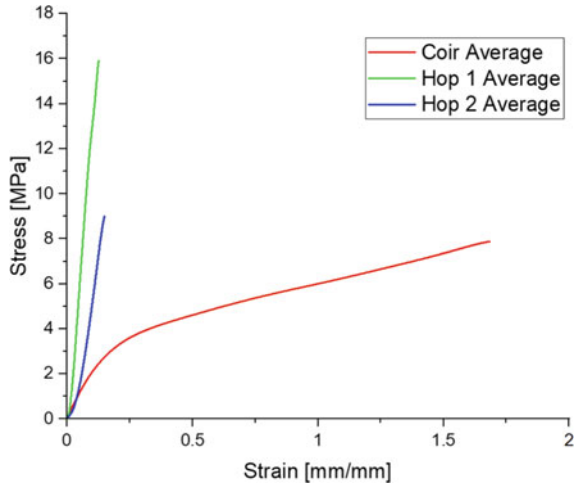
Table 2.4 Young's modulus and standard deviation

Sample	Young's modulus (MPa)	σ
Coir	40.5	8.6
Hop 1	16.1	5.8
Hop 2	30.8	3.9

Also, with the graphs, the force to failure was extracted for each sample and it is presented in Table 2.5 with its standard deviation.

Table 2.5 Ultimate tensile strength and standard deviation

Sample	Ultimate tensile strength (MPa)	σ
Coir	7.90	1.98
Hop 1	16.00	3.23
Hop 2	9.03	4.71

As seen in the results, the standard deviation was very high for the hop fibres batches, and it is due to the difficulty of tensile test on single lignocellulosic fibres, as explained before.

It was expected that the results for the hop fibre batches would be similar to the results for hemp and cotton fibres (Reddy and Yang 2009), but they were considerably different. The difference may possibly be because of the lack of distinguishment between what part of the bast was, causing a considerable variation in the results between samples and the expected results.

Combined with that, both batches of the hop fibres were not positioned in an aligned way for the drying process. They were tangled, as shown in Figs. 2.1 and 2.2, so when the samples were extracted only the strongest fibres were in conditions to be used in the test, the fibres that were thinner or had any type of defect could not even be aligned to be fixed in the test supports.

In the coir fibre samples, these problems were not seen. But many coir samples fractured near or in the gripping area which may be because of the fragilization of the extraction method or because of fragilization generated by the gripping method.

2.4 Conclusions

These are preliminary results for the use and comparison of these two fibre types. There are already many studies with the coir, but the use of the hop fibres has not been profoundly investigated. At the beginning of this research, the results are satisfactory and the major conclusion that can be assumed is that the extraction method must be improved to generate samples more standardized.

To have greater conclusions the tests have to be repeated making improvements in the fibre's extraction methods and controlling the other parameters to understand which parameters interfere the most in the test results.

References

Arulmurugan S, Venkateshwaran N (2019) Effect of nanoclay addition and chemical treatment on static and dynamic mechanical analysis of jute fibre composites. Polimeros 29(4)

Biswas S, Ahsan Q, Cenna A, Hasan M, Hassan A (2013) Physical and mechanical properties of jute, bamboo and coir natural fiber. Fibers Polym 14(10):1762–1767

Bredemann G (1944) Nachtrag Zu Der Arbeit: Nährstoffaufnahme Und Nährstoffbedarf Der Fasernesseln. J Plant Nutr Soil Sci 205–209

Bueno GI (2018) Eduardo Pinto Castro Ribeiro João da Rocha Silva Romeu Rony Cavalcante da Costa J. Efeitos da densidade de plantação, fertilização azotada e método de extração nas propriedades mecânicas de fibras de cânhamo

Bui TT, Boutouil M, Hanh Nguyen DH, Sebaibi N (2008) A simple review of using coconut fiber as reinforcement in composite [Internet]. Available from: https://www.researchgate.net/publication/344883615

Cai Z, Al Faruque MA, Kiziltas A, Mielewski D, Naebe M (2021) Sustainable lightweight insulation materials from textile-based waste for the automobile industry. Materials 14(5):1–21

Colomer-Romero V, Rogiest D, García-Manrique JA, Crespo JE (2020) Comparison of mechanical properties of hemp-fibre biocomposites fabricated with biobased and regular epoxy resins. Materials 13(24):1–8

Ekundayo G (2019) Reviewing the development of natural fiber polymer composite: a case study of sisal and jute. Am J Mech Mater Eng 3(1):1

Faruk O, Bledzki AK, Fink HP, Sain M (2010) Biocomposites reinforced with natural fibers: 2000–2010. Prog Polym Sci 37(2012):1552–96

Fiore V, di Bella G, Valenza A (2015) The effect of alkaline treatment on mechanical properties of kenaf fibers and their epoxy composites. Compos B Eng 68:14–21

Graupner N, Lehmann KH, Weber DE, Hilgers HW, Bell EG, Walenta I et al (2021) Novel low-twist bast fibre yarns from flax tow for high-performance composite applications. Materials 14(1):1–27

Hall J, Bhattarai SP, Midmore DJ (2013) The effects of different sowing times on maturity rates, biomass, and plant growth of industrial fiber hemp. J Nat Fibers 10(1):40–50

Haunreiter KJ, Dichiara A, Gustafson R (2021) Structural and chemical characterization of hop bine fibers and their applications in the paper industry. Ind Crops Prod 15:174

Kandemir A, Longana ML, Panzera TH, del Pino GG, Hamerton I, Eichhorn SJ (2021) Natural fibres as a sustainable reinforcement constituent in aligned discontinuous polymer composites produced by the HiPerDiF method. Materials 14(8)

Liu D, Han G, Huang J, Zhang Y (2009) Composition and structure study of natural Nelumbo nucifera fiber. Carbohyd Polym 75(1):39–43

Majid A (2011) Coconut fibre—a versatile material and its applications in engineering [Internet]. Available from: http://www.claisse.info/Proceedings.htm

Majid A (2011) Coconut fibre—a versatile material and its applications in engineering. In: MATEC Web of conferences, vol 17. Available from: MATEC Web of Conferences (matec-conferences.org)

Mwaikambo LY, Mwaikambo LY (2006) Review of the history, properties and application of plant fibres investigation of the performance of cotton woven fabrics view project review of the history, properties and application of plant fibres. Afr J Sci Technol (AJST) Sci Eng Ser 7 [Internet]. Available from: https://www.researchgate.net/publication/284760719

Protocol K (1998) United Nations framework convention on climate change. In: Kyoto Protoc 19(8):1–21

Reddy N, Yang Y (2009) Properties of natural cellulose fibers from hop stems. Carbohyd Polym 77(4):898–902

Saxena M, Pappu A, Sharma A, Haque R, Wankhede S (2011) Composite materials from natural resources: recent trends and future potentials. In: Advances in composite materials—analysis of natural and man-made materials. InTech

Tan C, Chong K, Thangavelu SK, Charlia Sia C (2021) Development of coir-fiber-reinforced nanocomposite for shell eco marathon vehicle body application. Mater Today Proc 4950–4954

Wackernagel M, Galli A (2007) An overview on ecological footprint and sustainable development: a chat with Mathis Wackernagel. Int J Ecodyn 2:1–9

Yun KK, Hossain MS, Han S, Seunghak C (2022) Rheological, mechanical properties, and statistical significance analysis of shotcrete with various natural fibers and mixing ratios. Case Stud Constr Mater 16:e00833

Zhao X, Copenhaver K, Wang L, Korey M, Gardner DJ, Li K et al (2022) Recycling of natural fiber composites: challenges and opportunities. Resour Conserv Recycl 177

Chapter 3
Simulation Strategies for Dynamic and Static Behaviour of Composite Beams

A. C. Alves, S. Alves, N. Peixinho, V. H. Carneiro, J. P. Mendonça, and O. Rodrigues

Abstract Doors and windows represent a vital role in domestic energy efficiency, and multi-material beams with a thermal break can be fundamental in terms of energetic sustainability. Their static and dynamic structural performance is fundamental to ensure a proper thermal insulation. Two multi-material composite beam topologies were tested in a three-point bending, while one was subjected to an experimental frequency response analysis. FEM models were created for the composite beams, using beam elements (BEAM189) and solid elements (SOLID186) with a shared topology configuration. Their capacity to predict the static and dynamic behaviour of the beams was assessed by comparing the numerical results with the experimental and analytical data. It is shown that the three-point bending behaviour of the physical beam could not be realistically captured by the 1D beam elements model, as their cross section with different components could not be coupled due to the relatively low stiffness of the polymeric components. However, the eigenfrequencies from the beam elements were very close to those measured experimentally, meaning the dynamic modulus at low strain values could keep the beam's cross section in-plane during the experiment. On the other hand, the 3D solid elements had the opposite outcome, agreeing with the experimental three-point bending test but not with the experimental modal analysis.

Keywords Composite beam · Three-point bending · Multi-material beam · Beam elements · Solid elements

A. C. Alves · S. Alves · N. Peixinho (✉) · V. H. Carneiro · J. P. Mendonça
Universidade do Minho DEM/Metrics, Guilhabreu, Portugal
e-mail: peixinho@dem.uminho.pt

O. Rodrigues
JFAN Steel, Guilhabreu, Portugal

3.1 Introduction

The current design trends of doors and windows systems were, and continue to be, heavily influenced by the rising demand in Europe for energy-efficient doors and windows (Architecture & Design 2021). For this reason, it became imperative to develop solutions that cater to sustainable living. To comply with additional consumer demands, such as a sense of space, natural light and better ventilation, glazing has taken over most surface space in door and window structures (Woodland Windows & Doors Blog 2021). In addition, with innovative glass technology and assembly, it is possible to achieve excellent thermal performances while making glazing the primary building material (Thames Valley Window Company Blog 2021). Furthermore, to assure adequate natural light and ventilation, the size of doors and windows can be increased, and their positioning can be altered, sometimes spanning over entire walls. Hence, taller, wider doors and windows, with almost non-visible frames, are a popular option nowadays (Woodland Windows & Doors Blog 2021). In addition, aesthetically, there is a preference for slender door and window frames that showcase the exterior view and allow more surface space for the glass panel (Thames Valley Window Company Blog 2021). Ideally, given the current trends, the beams that make up the frame of these systems should be as thin as possible. However, this constitutes a structural problem since these systems must abide by European standards and manufacturer technical guidelines that often require stiff beams. Therefore, the design of door and window systems, of large dimensions, with very slender frames has to take into account European certification tests that require a minimum level of structural strength and stiffness.

An efficient and practical solution to the mentioned problems would be to increase the width of the beams used in the design of these structures. However, given the aesthetic requirements for slenderness, the said solution is often not feasible. In other words, the increased mechanical properties provided by a stiff beam are forgone. Instead, a slender option is selected, more visually appealing, despite the increasing cost and demand for additional structural reinforcement. In these cases, the door and window systems must be designed outside the manufacturer's specification, and their rigidity and resistance must be increased without hindering their CE certification.

In addition, and despite not directly affecting the certification of doors and windows, dynamic vibration analyses are essential in the interest of escaping the frequencies of the loads caused by natural phenomena such as earthquakes and hurricanes, and consequently, prevent resonant effects in these systems. These loads are random and therefore non-deterministic, meaning that the future of the displacements, velocities and accelerations generated by these loads are hard to predict. These phenomena produce loads distributed in a wide frequency range, without significant peaks occurring in the frequency domain graphs. However, if such type of event has been measured on many occasions for a sufficiently long period, its statistical properties can be deduced. These phenomena are then described as a stationary stochastic process, and it is possible to assume that they follow, e.g. a Gaussian distribution. The frequencies at which the loads are applied can be plotted statistically using

a power spectral density (PSD) (Solari 1989; Dyrbye and Hansen 1997; Brandt 2011). Furthermore, to estimate the performance of the door or window system, its displacements and stresses must be evaluated. Consequently, since these values depend on damping, a correct damping characterization is essential to predict the dynamic behaviour of the structure in analysis.

To guarantee that door or window structures are designed well enough to pass the necessary certification, it is essential to predict their performance. The trial and error method implies unnecessary costs that would otherwise not exist if numerical simulation was used. Hence, numeric methods, such as the finite element method, combined with parameterized analyses, can be a precious help. Some scientific works can be cited regarding the application of FEM in static structural analysis to increase the resistance or rigidity of beams.

In 2016, Wang et al. (2016) used LS-DYNA, a nonlinear explicit finite element code, to simulate the three-point bending test of empty and reinforced multi-cell square tubes, which would then be validated by experimental testing. The goal was to then develop parametric studies that would investigate the influence of geometry configurations and loading conditions on the bending resistance of the tubes. Zhang and Zhang (2018) also analysed the bending behaviour of structures using experimental data and a numerical model to simulate a three-point bending test. The analysed structures were thin-walled square beams under quasi-static and dynamic loading. In terms of composite structures, Jin et al (2021) analysed the static behaviour of sandwich beams subjected to bending by a transverse load. The performed FEM analysis allowed the determination of the displacement response of the beams. Afterwards, the authors used Abaqus software to analyse the static behaviour of the sandwich beams. In 2022, approaches have been conducted for the case of a block matrix formulation of an uncoupled double Timoshenko beam, separated by a Winker elastic interlayer, that allowed the determination of its modal response (Copetti et al. 2022). Additionally, computational methods have been developed, by Eberle and Oberguggenberger et al. (2022), based on experimental results from bending tests and analytical data, for an Euler–Bernoulli beam with a varying cross section along its length. All these developments can be helpful, for instance, to describe the modal response of sandwich composites or laminated beams and in defining the bending stiffness of irregular beams (Copetti et al. 2022; Eberle and Oberguggenberger et al. 2022). Furthermore, it is evident that the study of beams that possess geometrical details that increase the complexity of their behaviour, e.g. variable cross section along their length and/or multiple components, is still evolving.

This study details different approaches simulate the static and dynamic behaviour of multi-material composite beams, using door and window frames as benchmark. Two multi-material composite beams with complex section topologies were subjected to a three-point bending tests. One of the beam topologies was also subjected to vibrations analysis to determine its frequency response. Finally, two FEM models were created to simulate the performance of the composite beams using 1D beam and 3D solid elements. Conclusions were obtained regarding their capability to depict the static and dynamic behaviour of the tested beams once the numerical results were compared with analytical and experimental data.

3.2 Methodology

Multi-material complex beams with complex section topologies were selected from the Secco Sistemi catalogue (2020). Their manufacturing process consists of machine rolling of the brass sheets to from the shells which are combined with polyamide and polyurethane cores (Fig. 3.1). These models are referred by Secco Sistemi as EBE85 P.1102 and P.2992.

While the metal shells define the external geometry of the composite and influence the type of opening system, the final product will have the thermal break contributes mostly towards thermal insulation.

Tensile properties of the beam materials were previously determined as part of an ongoing study. Their elastic, elastoplastic and physical properties are presented in Table 3.1. It may be determined that these are the fundamental properties to perform static elastoplastic structural analysis with a bilinear hardening models and harmonic analysis using FEA. The Poisson's ratio of these materials was assumed as 0.33.
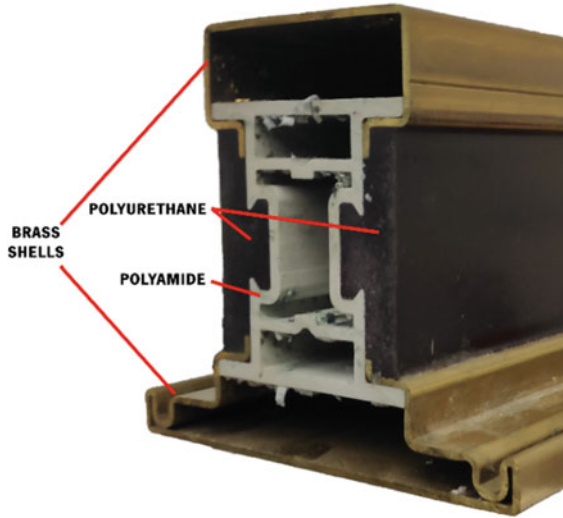
Fig. 3.1 Standard Secco Sistemi material combination exemplified on an EBE85 P.1102 beam

Table 3.1 Experimentally obtained properties of Secco Sistemi brass, polyurethane and polyamide

Material	E (GPa) $\pm$ STD	σ_y (MPa) $\pm$ STD	ρ (kg/m^3) $\pm$ STD	E_t (MPa)
Brass	102.64 $\pm$ 1.48	248.55 $\pm$ 6.36	8491.97 $\pm$ 4.22	926
Polyurethane	0.57 $\pm$ 0.02	31.11 $\pm$ 1.27	1134.00 $\pm$ 0.16	20
Polyamide	0.65 $\pm$ 0.01	46.29 $\pm$ 1.07	1336.03 $\pm$ 1.12	86.91

The values of the tangent moduli were retrieved from Alves (2022)
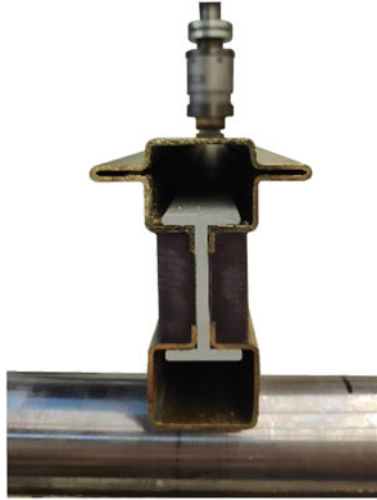
Fig. 3.2 Lateral view of the Secco Sistemi OS275 P.2992 during the three-point bending test

In order to test the static and dynamic performance of the composite beams, these were subjected to a three-point bending test and an FRF modal testing. The Secco Sistemi OS275 P.2992 composite beam will be taken as an example for all other tested beams for the following detailed experimental methods.

An example of the three-point bending testing is depicted in Fig. 3.2 for the symmetric Secco Sistemi composite beam OS275 P.2992 in its brass version with a length of 1600 mm.

This test was performed in an Instron 8874 universal testing machine, with a half cylinder steel mounted at the end of the hydraulic cylinder and a steel base structure with two steel cylindrical supports. The supporting cylinders on the base structure were 1540 mm apart, and the base structure was mounted in a way that put the loading half cylinder, which was attached to the hydraulic ram at the same distance from each supporting pin. Each beam was then placed on the supporting pins so that a transversal plane would pass at the centre of the loading cylinder, which was then lowered to be tangent to the top face of the beam. A digital gauge with a magnetic base was placed on the base structure, measuring the displacement of the beam on the bottom face on its mid-length. The Instron Bluehill data acquisition software was used again for the data collection. This detailed setup is represented in Fig. 3.3.

Two displacement measurements took place on the mid-length of the beam during the test, one on the top face registered by the Instron Bluehill software and another at the bottom face recorded by the digital gauge. Once the displacement registered on the digital gauge reached 10 mm, it was removed since enough data was gathered to calculate the stiffness. During the test, the hydraulic ram imposed a 0.025 mm/s displacement rate until collapse was monitored.
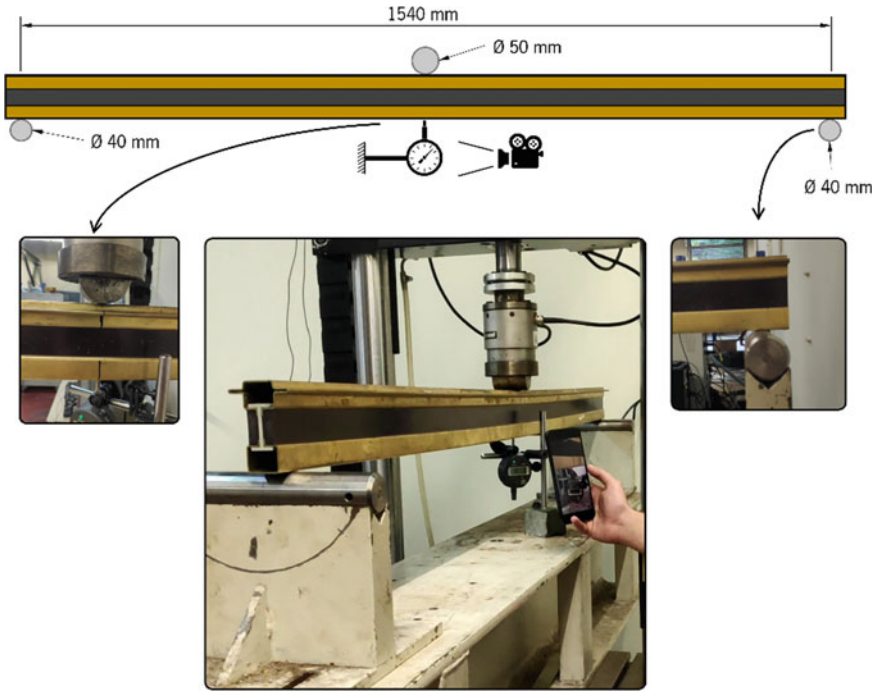
Fig. 3.3 Three-point bending test setup

The experimental vibration analysis (Fig. 3.4) required a PCB piezoelectric model 086c01 impact hammer which was used to impose an impact excitation, while a PCB model 356A1 triaxial piezoelectric accelerometer monitored the dynamic behaviour of the beam. A LMS Scadas mobile spectrum analyser was used to process and analyse the signal and obtain the frequency response function (FRF). After obtaining the general FRF of the system, in the *z*-direction, the damping ratio was determined from the first resonance frequency using the half-power bandwidth method.

The analytical model of the composite beams behaviour was necessary to validate the experimentally obtained results. Therefore, an analytical method was used to transform the studied composite beams into homogenous transformed versions that facilitated calculations and variable manipulation.

The analytical method was based on the Euler–Bernoulli beam theory. The following assumptions were made: the distinct beam elements are bonded together at the various interfaces, and the beam cross section remains unchanged after bending. This allows for the multi-material beam to be defined as a single beam since the centre of curvature of the different elements, when bent, is the same at any point along the length of the beam.

The resulting bending moment of the beam, *M*, from the applied external loads, will match the resistance offered by its distinct elements, as depicted in Fig. 3.5. Therefore, the total moment of resistance of the beam will equal the sum of the
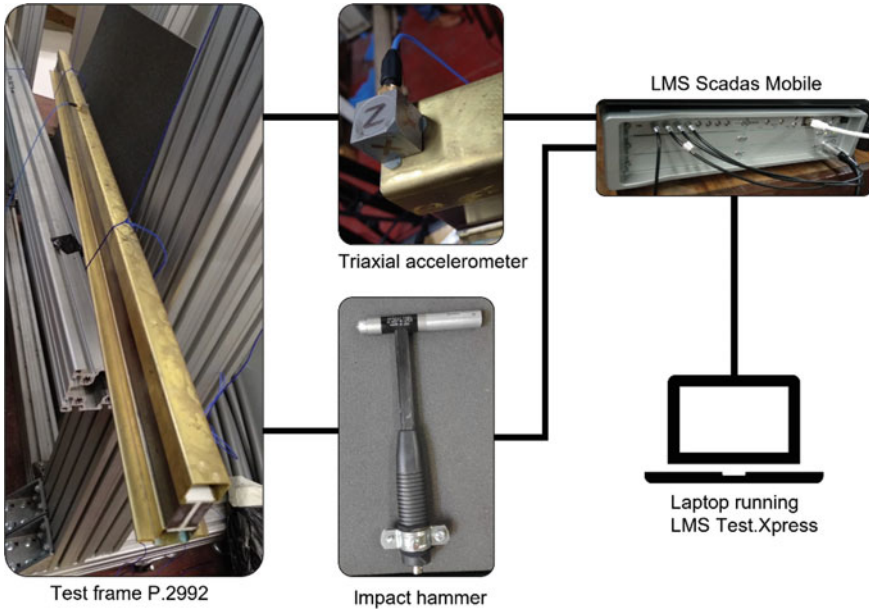
Fig. 3.4 Experimental modal analysis setup

moments supported by each element as stated by Eq. (3.1).

$$M = \sum M_i = \sum -E_i I_i \frac{d^2 y}{dx^2} \tag{3.1}$$
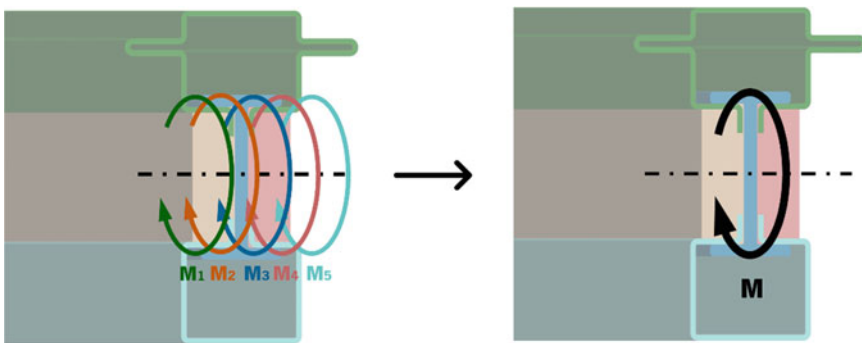
Fig. 3.5 Internal moments from the five components of an MMB compose the internal bending moment that results from applying the external loads

By rearranging Eq. (3.1) into Eq. (3.2), it is possible to obtain an equivalent homogenous beam, made of a single and arbitrarily chosen material, with an equivalent second moment of area I_{eq}, to the original beam determined by Eq. (3.3). Figure 3.6 illustrates the cross section of this transformed homogenous equivalent beam, where the material of the different components influences the weight of its elemental areas in the equivalent beam's cross section. In this case, the equivalent beam is illustrated by expanding each elemental area by the correspondent n_i in a direction parallel to the axis of rotation. The variables d and b represent the distance between the centroid of a component's cross section and the equivalent beam's neutral plane or the CAD software's axis, respectively.

$$M = -E_b I_{eq} \frac{d^2 y}{dx^2} \tag{3.2}$$

$$I_{eq} = \sum \frac{E_i}{E_b} I_i \tag{3.3}$$

Analysing the contribution of element i to the second moment of area, a factor n_i can be singled out, being multiplied by the elemental area, dA, as shown in Eq. (3.4). Consequently, and as represented in Eq. (3.5), the position on the centroid to consider $\overline{Y}$, needs to account for the factors n_i.

$$\frac{E_i}{E_b} I_i = n_i I_i = n_i \int y^2 dA = \int y^2 n_i dA \tag{3.4}$$
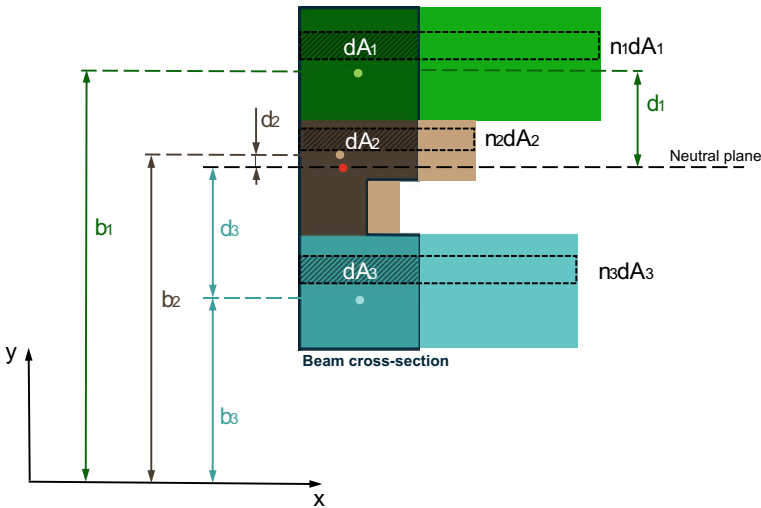
Fig. 3.6 Representation of the cross section of the equivalent beam, from the cross section of a composite beam

$$\overline{Y} = \frac{\sum \int y n_i \, dA}{\sum \int n_i \, dA} = \frac{\sum n_i b_i A_i}{\sum n_i A_i} \qquad (3.5)$$

With this, other equations can be found, for instance, for a composite beam of length L, the three-point bending deflection, represented by Eq. (3.6), and the natural frequencies of the beam in the transverse direction, represented by Eq. (3.7).

$$\delta_{\max} = \frac{P L^3}{48 E_b I_{eq}} \qquad (3.6)$$

$$w_n = \beta_n^2 \sqrt{\frac{E_b I_{eq}}{\sum \rho_i A_i}}; \quad \beta_n = 4.7300L; \ 7.8532L; \ldots \qquad (3.7)$$

The data from the experimental tests was compared to the data from numerical models developed to capture the static and dynamic behaviour of the composite beam. These models were constructed with beam elements (BEAM189, based on Timoshenko's beam theory) and solid elements (SOLID185 and SOLID186). Additionally, the geometry was prepared in Design Modeler, and the numerical simulations were performed on ANSYS Workbench. The three-point bending simulation was performed in the static structural module, and the modal module was used to find the natural frequencies of the composite beam's models.

The first developed numerical model used five 1D beam elements to represent the different components of the composite beams in analysis. This numerical model consisted of five line bodies representing each beam component and the corresponding material data, boundary conditions and applied loads that simulated the physical problem. The static and dynamic simulations considered 1540 mm and 1600 mm lengths, respectively.

The first step in creating the beam elements model was defining a static structural analysis in ANSYS Workbench and adding the materials to the Engineering Data of the project. More specifically, only the elastic modulus, density, Poisson's ratio and tangent modulus were used.

After defining the necessary material properties in the Engineering Data of the project, the geometry of the composite beam was defined in Design Modeler where five separated parallel line bodies, already cut for the boundary conditions to be applied in ANSYS Mechanical (in the static analysis), were given the cross sections relative to each of the composite beam's components. With the "Connect" tool, the line bodies were joined without being merged, each vertex at a time, to the location of one of the line bodies. Then, the correct offsets were given to each line body's cross section, as illustrated in Fig. 3.7, before these line bodies were joined using the "Share Topology" tool. This tool resulted in coincident nodes being created on coincident geometry and the DOF of these nodes being bonded together. This step will guarantee that the separate elements will be treated as a single multi-component beam in the numerical model.

P.2992   P.1102
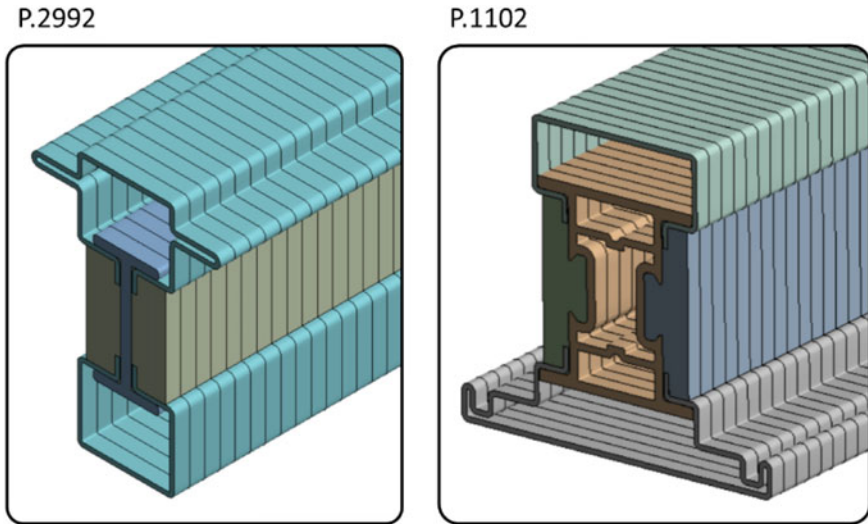
Fig. 3.7 Beam elements models with the different cross sections graphically displayed, taken in ANSYS mechanical

A quadratic element was used in this model, more specifically BEAM189, when defining the mesh. Additionally, for the static analysis, an element size of 5 mm was selected, and for the modal analysis, a division of 100 was employed on the line bodies without the geometry split.

Once the materials, geometry and mesh properties were defined, it was possible to characterize the numerical model's boundary conditions, which represent a simply supported beam in pure bending physical problem, as depicted in Fig. 3.8. Additionally, the large deformation effects were turned on, and several timesteps were defined. Relating the load and displacement in the vertical direction at each timestep, it was possible to build the force–displacement curve.

For the modal analyses, damped and undamped, the goal was to find nine natural/resonant frequencies, which made it possible to achieve all the values for
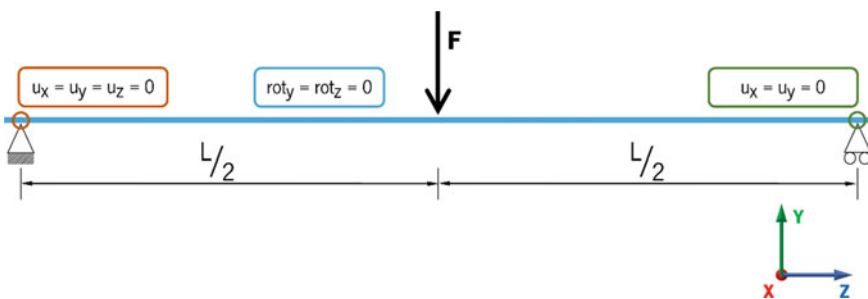
Fig. 3.8 Constraints/boundary conditions applied in the static analysis of the beam elements model

comparison with the analytical model and the experimental data. In the damped modal analysis, damping was turned on, and the first resonance frequency and the correspondent damping ratio from the experimental modal analysis were used for the programme to calculate the Rayleigh damping, considering the mass damping as zero. A range from 5 to 400 Hz was considered for both analyses.

Compared to the beam elements model, there was no simplification of the boundary conditions in the solid elements model, and the maximum deformation could be determined for any point of the composite beam, not exclusively the neutral axis. However, there was a simplification of the beams' cross sections. The simulations with this model were also performed in ANSYS Workbench, in a static structural module, for the static study, and in the modal module, for the dynamic study, and the same materials introduced in the Engineering Data of the simulations with the beam elements model were also considered in these simulations.

For the three-point bending simulations, ¼ of the brass composite beam was modelled, and symmetry conditions were applied in the model. By reducing the geometry to ¼, a significant amount of computational time was saved without affecting the results. For the P.2992 and P.1102 beams, a length of 1600 mm and 1540 mm was considered, respectively. Additionally, for the static analyses, to prepare the mesh, the geometry of the beam was cut into several bodies and strategically split near the ends to further refine the mesh in the zones where contact was expected with the loading and support pins. These pins were modelled as surfaces and had symmetry conditions applied to them. The cut geometry was bonded together using the "Share" tool, which in the case of the P.1102 profile also considered the geometry from the loading and support pins.

For the dynamic analysis, the 1600 mm beam was modelled without cuts, and the different bodies had their topology shared to bond the beam components. In the static simulation, each material was assigned to its corresponding component. The thickness of the surfaces was defined, with an offset to the interior of the loading and support pins, as their radius. Frictionless contacts with penetration of 0.1 mm and a symmetric behaviour were defined between the loading and support pins and the contacting faces of the beam, as well as between the internal beam surfaces that became into contact during the three-point bending experiment.

The static and dynamic simulations both used quadratic elements, SOLID185 (P.1102) and SOLID186 (P.2992) for the beam geometry and SHEL181 (P.1102) and SHELL281 (P.2992) for the pins. Figures 3.9 and 3.10 show the meshed geometry used in the static and dynamic analyses, respectively.

In the post-processing phase, the displacements at the bottom and the top of the composite beam were then probed at the central symmetry plane and plotted against the reaction force ($\times 4$) in the vertical direction at each timestep, allowing for a force–displacement curve to be constructed and compared with the three-point bending experimental data. Since the frequency response analysis considered the composite beam free in space, no boundary conditions were specified.
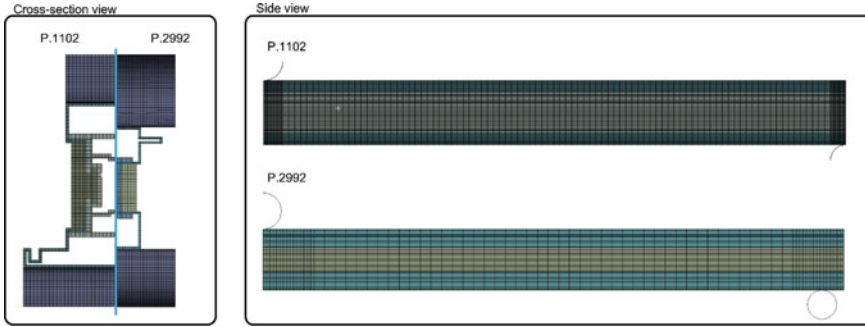
Fig. 3.9 Solid elements model of the three-point bending analysis
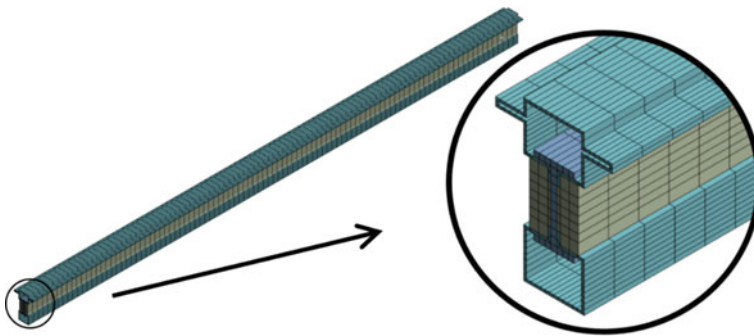
Fig. 3.10 Solid elements model of the frequency response analysis

3.3 Results

In Fig. 3.11, it is possible to observe that the analytical and numerical models have similar results despite overestimating the actual stiffness of the tested composite beams.

When discussing the graph related to the P.1102 beam's top face, it is possible to conclude that the curves for the solid elements model and the experimental data essentially overlap. For the P.2992 beam, this only occurs in the initial section of the graph. In addition, for the same beam, it can be observed that there are small but abrupt drops in force in the experimental data, which are linked to the loss of adhesion between the composite beam components. The final drop is related to the complete loss of adhesion between one of the brass components and the rest of the beam. Since the adhesion of the interface between the different components of the beam was not accounted for in the solid elements model, this model only depicts the experimental data on the initial part of the curve. It could also be observed that indentation caused by the loading pin occurred on the top face of both the solid elements model and the experimental test.
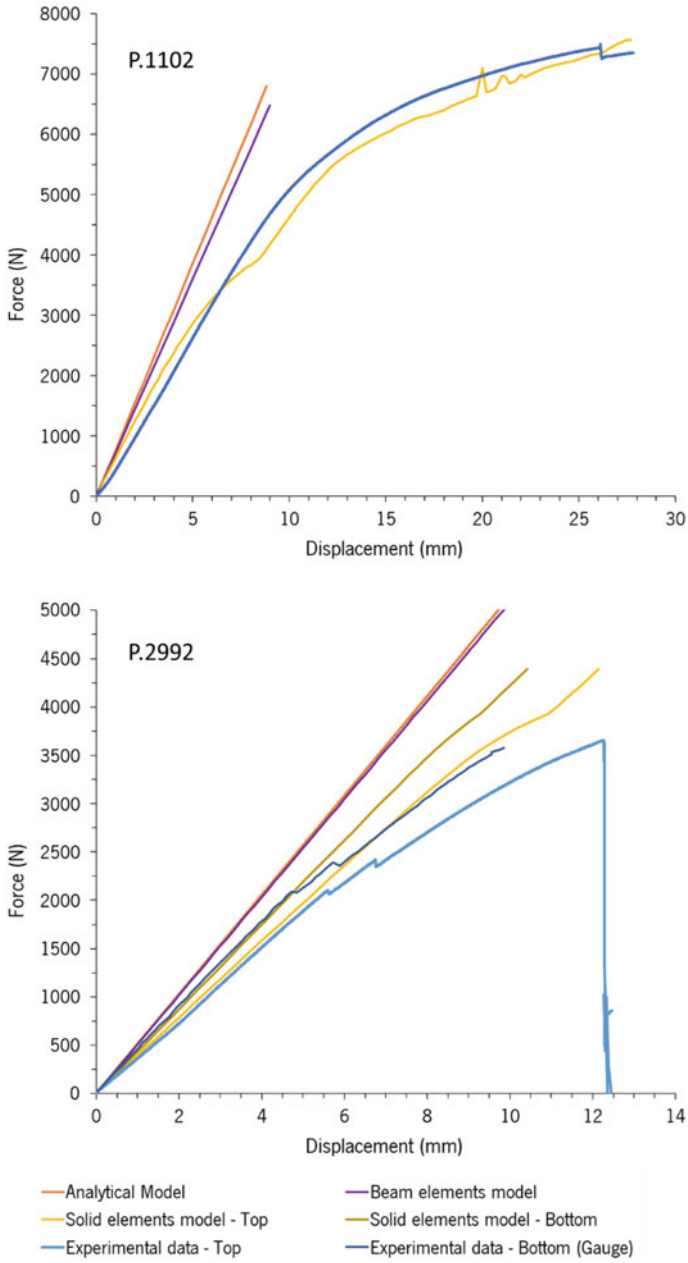
Fig. 3.11 Force–displacement curves for analytical, numerical and experimental results

As shown in the P.2992 graph, the solid elements models can also depict the deformation of the physical beam at the bottom face, where indentation did not occur on the supports or the loading pin, meaning that this curve can be taken as representative of the composite beam's real force–displacement curve.

The analytical and the beam elements models overestimate the stiffness of the physical beam; however, this is not observed in the solid element models. This can be attributed to the formulation and the elastic moduli of polymers. Both the analytical method and the beam elements models assume the beam's cross section remains in-plane, i.e. they follow the Euler–Bernoulli and the Timoshenko beam theories. However, this does not happen, as the elastic moduli of the polymers do not provide these components with enough stiffness to resist the deformation that results from the longitudinal shear stresses that appear when the composite beam is bent. As the solid elements model can capture this drop in stiffness, its results are coherent with the experimental data at the bottom of the beam. Figure 3.12 details the deformed shapes that support this hypothesis.

The results from the experimental modal analysis of the composite beam can be found in the FRF plotted in Fig. 3.13, where three significant eigenfrequency peaks can be identified. Using the half-power bandwidth method applied on the first peak, a damping ratio of 0.0135 was determined.

Table 3.2 compares the eigenfrequency values from the analytical and numerical models to those obtained from the experimental data. With this, it is possible to note that the introduction of damping has little influence on the frequency values but still causes a slight reduction, as expected by for damped eigenfrequencies. The first eigenfrequency (ω_1) is relatively close to the experimental value on all models, with
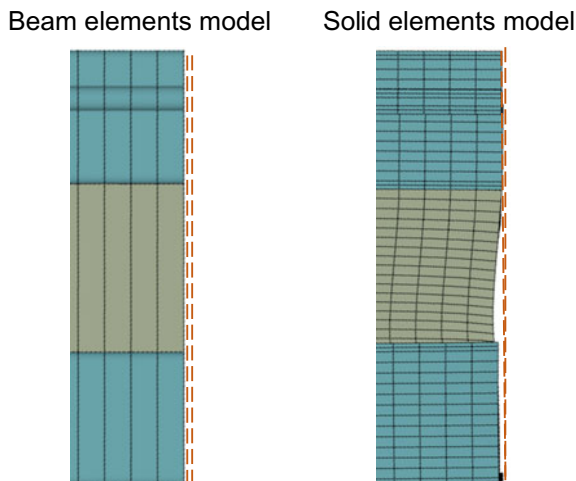
Fig. 3.12 Deformation at the end of the composite beam by a factor of 40 for the numerical models, where the beam elements model is the only one that keeps the cross section of the composite beam in-plane
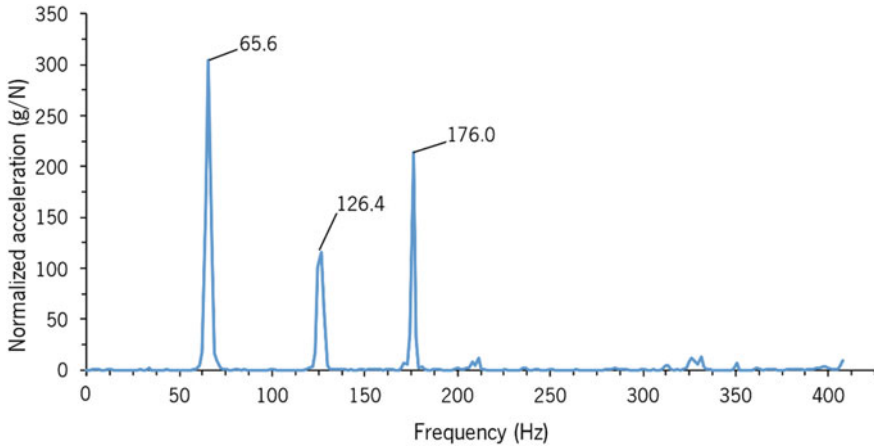
Fig. 3.13 FRF modal analysis of P.2992 beam with peak frequencies

the error being around 3%. For the second eigenfrequency (ω_2), contrary to what had happened in the three-point bending analysis, the analytical and beam elements models had results closer to the experimental data, and the solid elements models presented results with much lower values, reaching a deviation of almost -10% from the experimental value. From the results of the third eigenfrequency (ω_3), similar observations to those from the first resonance frequency results could be made, with the slight difference that the analytical and beam elements model agree even better with the experimental data, and the solid elements model error is slightly higher.

For traditional materials (e.g. steel), the elastic modulus is assumed to be constant. However, for polymers, it has been experimentally proved that the value of this property, when determined by static and by dynamic methods, varies considerably due to the viscoelastic behaviour of these materials, which makes them dependent on the strain rate and temperature, and exhibiting hysteresis under cyclic load, dissipating a good amount of energy (Popov and Sabev 2016; Fan et al. 2017; Massaq et al. 2013).

Table 3.2 Natural and resonant frequencies results, of a P.2992 beam, from numerical models and frequency response analysis

	Eigenfrequencies (bending modes)	Numerical				Analytical	
		Beam (Hz)	Error (%)	Solids (Hz)	Error (%)		Error
Undamped	ω_1	63.50	− 3.20	64.00	− 2.45	63.79	−2.76%
	ω_2	124.66	− 1.38	114.18	− 9.64	126.28	− 0.09%
	ω_3	174.00	− 1.14	171.35	− 2.68	175.84	− 0.09%
Damped	ω_1	63.49	− 3.21	63.99	− 2.46	–	–
	ω_2	124.62	− 1.41	114.18	− 9.67	–	–
	ω_3	173.89	− 1.20	171.19	− 2.73	–	–

The increase of stiffness of the beam in vibration, due to the increase in the elastic modulus, can explain why the second resonant frequency in the physical frame is higher than in the solid elements model while presenting relatively similar results to the analytical and beam elements models. The higher modulus causes the beam's cross section to remain in-plane. Since the analytical and beam elements models' formulation depicts the beam's cross section in-plane throughout its deformation, they can capture the behaviour of the physical beam since once the cross section is in-plane, most of the beam's bending stiffness comes from the metal components, and the elastic modulus of the polymers has less influence. On the other hand, because the polymers cannot maintain the beam's cross section in-plane on the solid elements model, there is a significant loss in stiffness, and the second resonant frequency appears earlier.

This conclusion makes sense with the three-point bending results. The main differentiating factor between the stiffness of the analytical, beam elements and solid elements model was whether the cross section could remain in-plane or not. Hence, there is a clear distinction between the static elastic modulus and the dynamic elastic modulus of the polymeric materials.

3.4 Conclusions

The results for both the analytical data and the beam elements models showed agreement in the static analysis and presented a similar stiffness. However, these models overestimated the stiffness of the real beam since, in the experiment, the cross section of the composite beam did not remain in-plane due to the high difference between the elastic modulus of the brass and polymeric components. Since the formulation of these models assumes the beam keeps its cross section in-plane, throughout its deformation, they are not very realistic. On the other hand, the solid elements model captured the deformation behaviour of the beam's cross section and therefore depicted the real bending behaviour of the tested composite beam. Because the interface between components was not studied and therefore not accounted for in this numerical model, the sliding between components that occurred in the experiment could not be captured. In addition, despite this sliding taking place for the P.2992 beam, it never happened in the experimental test with the P.1102 beam.

In the dynamic analysis, since the dynamic modulus of the polymers was higher than their static elastic modulus and the cross section of the physical beam remained in-plane during the experiment, opposite results from the static analysis were observed. The analytical method and the beam elements models maintained the beam's cross section in-plane as it was deformed and exhibited similar outcomes. In addition, both could depict the resonant frequencies of the physical composite beam. On the other hand, the solid elements model did not account for the change in elastic modulus for a dynamic application, so it still depicted an unrealistic deformation behaviour for the cross section of the beam and underestimated the stiffness of the

beam. This resulted in smaller values for the resonant frequencies with mode shapes that depended on the behaviour of the cross section of the beam.

References

Alves A (2022) Study, modelling, and dynamic analysis of construction solutions for doors and windows of buildings. M.Sc. Dissertation, Department of Mechanical Engineering, University of Minho

Architecture & Design (2021) New study indicates upward trend for global windows and doors market. Architecture news & editorial desk. https://www.architectureanddesign.com.au/news/upward-trend-for-global-windows-and-doorsmarket. Accessed on 12 Dec2021

Brandt A (2011) Noise and vibration analysis: signal analysis and experimental procedures, 1st edn. Wiley

Catalogue (2020) Secco sistemi

Copetti R, Claeyssen J, Tolfo D, Pavlack B (2022) The fundamental modal response of elastically connected parallel Timoshenko beams. J Sound Vib 530:116920

Dyrbye C, Hansen S (1997) Wind loads on structures. Wiley, Chichester, New York

Eberle R, Oberguggenberger M (2022) A new method for estimating the bending stiffness curve of non-uniform Euler-Bernoulli beams using static deflection data. Appl Math Model 105:514–533

Fan J, Fan X, Chen A (2017) Dynamic mechanical behaviour of polymer materials. In: Yilmaz F (ed) Aspects of polyurethanes. InTech

Jin L, Lan Y, Zhang R, Du X (2021) Numerical analysis of the mechanical behavior of the impact-damaged RC beams strengthened with CFRP. Compos Struct 274

Massaq A, Rusinek A, Klosak M (2013) Method for determination of the dynamic elastic modulus for composite materials. Eng Trans 61:301–315

Popov I, Sabev S (2016) Comparative analysis of static and dynamic elastic modulus of polymer concrete polymers. Mach Technol Mater 10(12):38–41

Solari G (1989) Wind response spectrum. J Eng Mech 115(9):2057–2073

Thames Valley Window Company Blog (2021) The 2021 architectural glazing trends you need to know about. https://www.tvwindows.com/blog/the-2021-architectural-glazing-trends-you-need-to-know-about. Accessed on 12 Dec 2021

Wang Z, Li Z, Zhang X (2016) Bending resistance of thin-walled multi-cell square tubes. Thin-Walled Struct 107:287–299

Woodland Windows & Doors Blog (2021) Trends in windows and doors. https://www.woodlandwindows.com/support/blog/2021-trends-in-windowsdoors. Accessed on 12 Dec 2021

Zhang X, Zhang H (2018) Static and dynamic bending collapse of thin-walled square beams with tube filler. Int J Impact Eng 112:165–179

Chapter 4
The Design of a Cementitious Material Modified with the Synergistic Addition of Sodium Silicate and Fine Aggregate Sourced from Granite Waste in Order to Obtain a Mortar with Low Capillary Suction

Natalia Szemiot and Łukasz Sadowski

Abstract The aim of the study was to design a cementitious material that is prepared with the synergistic addition of sodium silicate and granite fine aggregate in order to obtain low capillary suction. For this purpose, three different classes of cement mortar (M15, M10, M5), one type of granite fine aggregate and two different proportions of additive in the form of sodium silicate (0.002 kg, 0.005 kg) were analysed. Firstly, the capillary suction of the granite aggregates was analysed and compared with traditional sand. Afterwards, nine cementitious material bars were made, which were then used to examine the capillary suction. It was proved that the M15 cementitious material with the granite fine aggregate and a higher proportion of the additive had the lowest capillary suction. In turn, the M5 cementitious material without the additive had the highest index of capillary suction, which shows that adding sodium silicate to cement mortar can significantly reduce its capillary suction. Finally, the results of this study were compared with the previous authors' studies concerning basalt and quartz fine aggregates. As a result of the research, it was found that the cementitious material with the fine quartz aggregate had a lower rate of capillary suction index than the cementitious material with the fine basalt aggregate.

Keywords Design · Cementitious materials · Capillary suction · Granite fine aggregate · Mortar

N. Szemiot (✉) · Ł. Sadowski
Department of Materials Engineering and Construction Processes, Wroclaw University of Science and Technology, Wrocław, Poland
e-mail: nataliaszemiot@gmail.com

Ł. Sadowski
e-mail: lukasz.sadowski@pwr.edu.pl

4.1 Introduction

Dampness is one of the main causes of the degradation of civil engineering structures made of brick (e.g. buildings and bridges). In winter, moisture can freeze and lead to the bursting of building materials due to an increase in the volume of water as it becomes solid (Clim et al. 2017; Aval et al. 2022; Yik et al. 2004; Hoła and Czarnecki 2022). The common process of the flow of moisture in the structure of building materials is known as capillary suction (Popek and Wapińska 2009; Pratiwi et al. 2020; Saberian et al. 2017; Karagiannis et al. 2018), which involves the upward transport of water in a porous material by means of capillary forces. These forces depend on the amount of open pores in the material, as well as their diameters (Karoglou et al. 2005; Dondelewski and Januszewski 2008). The smaller the diameter of the capillaries, the higher the level of wall dampness. The height at which capillary suction is noticeable which depends on the structure of the material, primarily its porosity and the system of pores and capillaries (Moropoulou et al. 2001). Figure 4.1 shows the capillary suction of water.

Moisture occurring in building partitions causes the deterioration of their properties, such as e.g. their thermal resistance. In article (Kon and Caner 2022), the authors present the influence of various insulation materials (e.g. hemp wool insulation), and their thicknesses, on the reduction of dampness in walls. They also describe the use of various energy sources for limiting the appearance of dampness in walls. Regardless of the type of used insulation, dampness and mould, to a greater or lesser extent, appeared on the walls.

Cement mortar contains cement, water and aggregate, and therefore when designing cementitious materials, the type of fine aggregate is important (Woźniak
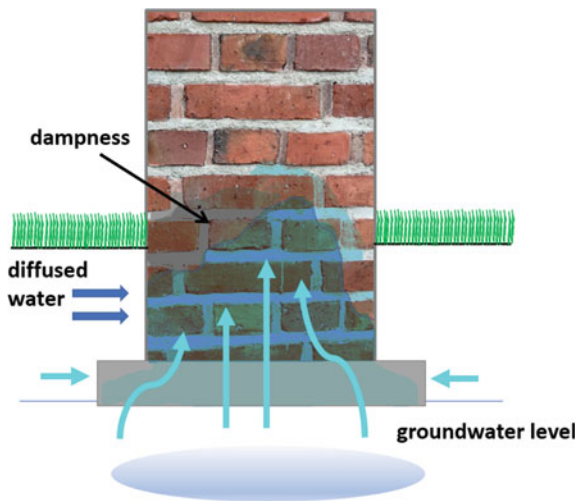
Fig. 4.1 Capillary suction of water as a one of the main reasons of dampness in civil engineering structures made of brick

and Chajec 2022). Approximately 71–78% of the volume of cement mortar is fine aggregates sourced from granite quarry waste. Nowadays, the application of aggregates from industrial wastes is getting more attention (e.g. regarding their use in fine-grained concrete with enhanced durability (Zajceva et al. 2021), or mortars with fine aggregates sourced from crushed glass (Czapik et al. 2020)). In the research presented in this article, granite fine aggregate was used. The results of this study were compared with the authors' previous studies concerning basalt and quartz fine aggregates. Moreover, the used cementitious material was modified with the addition of sodium silicate in various proportions.

The novelty of the article involves the design of a cementitious material that is modified with the addition of sodium silicate and granite fine aggregate in order to obtain a material with low capillary suction. Moreover, the authors conducted research on the reduction of the capillary suction index of cementitious mortars that were prepared with the use of sodium silicate, basalt fine aggregate and quartz fine aggregate.

4.2 Materials and Methods

4.2.1 Granite Fine Aggregate

In the authors' studies, granite fine aggregate with a density of $\rho d = 2.60$ g/cm^3 was used. The grain size of granite fine aggregate ranges from 0.25 to 2.5 mm. It is a natural aggregate that consists of many minerals, such as mica (about 10%), quartz (about 35%) and feldspar (60–65%). Granite is the most common igneous rock and occurs on all the continents in the world (Nedelec and Bouchez 2015). Figure 4.2 represents the particle size distribution of granite fine aggregate.

4.2.2 Cement

Portland cement CEM I 42.5 R was used in the research. Portland cement is a loose and grey material that is made by combining ground cement clinker (95%) with gypsum (max. 5%) (Bogue 1948). The chemical composition of clinker includes: alite; tricalcium silicate (50–65% of the clinker's mass); belite; dicalcium silicate (approx. 20% of the clinker's mass); brownmillerite; a compound of calcium oxide, aluminium oxide and iron (III) oxide (approx. 10% clinker mass); tricalcium aluminate (approx. 10% of the clinker's mass); and other aluminium, calcium and magnesium compounds (Double et al. 1978). CEM I is a Portland cement with no additives and is a pure form of cement. In Portland cement CEM I 42.5 R, there is 0.07% of Cl-, 3.2% of SO_3 and 0.80% of Na_2O. The grain size of Portland cement ranges from 0.02 to 0.14 mm.
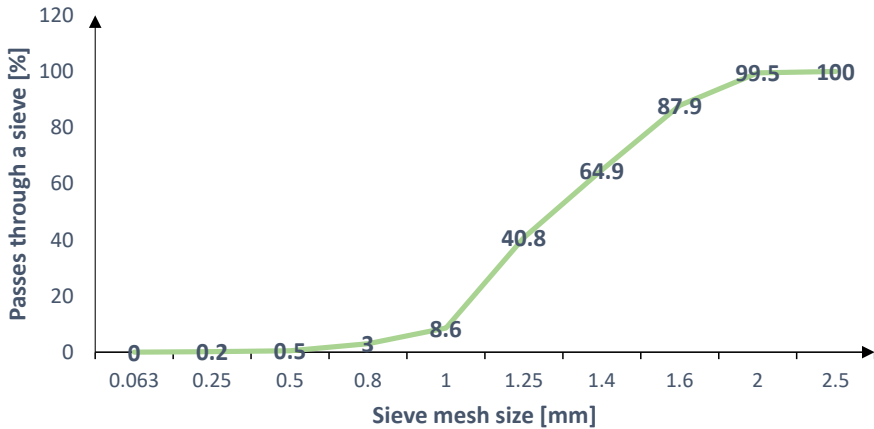
Fig. 4.2 Particle size distribution of granite fine aggregate

4.2.3 Sodium Silicate

Sodium silicate was used in this study as an admixture. The chemical formula of this admixture is $Na_2O\ nSiO_2$. The content of the pure substance ranges from 18 to 40% ($Na_2O + SiO_2$), and the rest is water. Sodium silicate is a semi-translucent, white or colourless, viscous and odourless liquid, which is easily soluble in water. It is inorganic, non-flammable and has a pH of 11–13 in a temp of 20 °C. The pour point of sodium silicate is 730–870 °C, and its softening point is 550–670 °C. The relative density of this substance ranges from 1.26 to 1.71 g/cm^3, and its tenacity ranges from 20 to 800 mPa/20 °C. The substance is mixed with water in different ratios.

4.2.4 Testing the Capillary Suction of the Granite Fine Aggregate

The research consisted of measuring the height of the capillary suction of the granite fine aggregate. For this purpose, three granite fine aggregate samples were prepared, with each being placed in a 1500 mm long pipe of plexiglass. The dimensions of the pipe and the test stand are shown in Fig. 4.3. The pipe was embedded in a glass container filled with liquid up to 10 mm, and then filled with granite fine aggregate. After a specific time, the index of the capillary suction of the fine aggregate was measured. Figure 4.3 shows the scheme of testing the capillary suction of the granite fine aggregate.
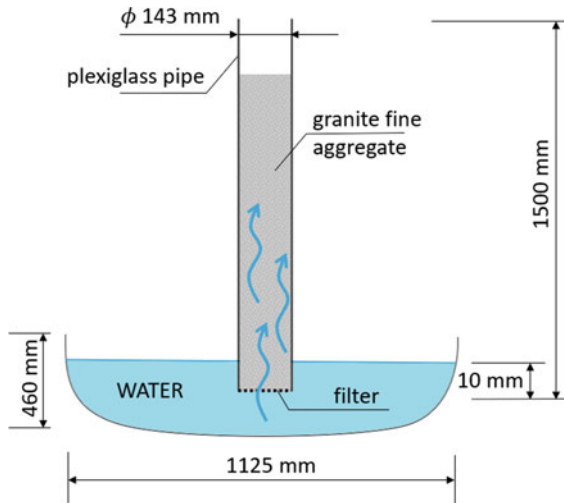
Fig. 4.3 Testing the capillary suction of the fine granite aggregate (own elaboration based on Wysocka et al. 2013)

4.2.5   Testing the Capillary Suction of the Designed Cementitious Material

The research consisted of measuring the height of the capillary suction of the cementitious material. 9 bars of cementitious mortar with dimensions of 40 × 40 × 160 mm were prepared according to standard PN-EN 480-1. Figure 4.4 shows the components of each of the 9 bars of the cementitious mortars. The amounts of the components of the cementitious materials are shown in kilograms. The cementitious material was kept in moulds for 28 days. After this time, the capillary suction tests were performed, with the index of the capillary suction of the cementitious material then being measured.

4.3   Results

4.3.1   The Capillary Suction of the Granite Fine Aggregate

Three samples of granite fine aggregate were used to analyse its capillary suction. Each sample was measured thirteen times. From these 3 samples, the average height of the capillary suction was calculated and is given in the last column of Table 4.1. Table 4.1 presents the results of testing the capillary suction of the granite fine aggregate.
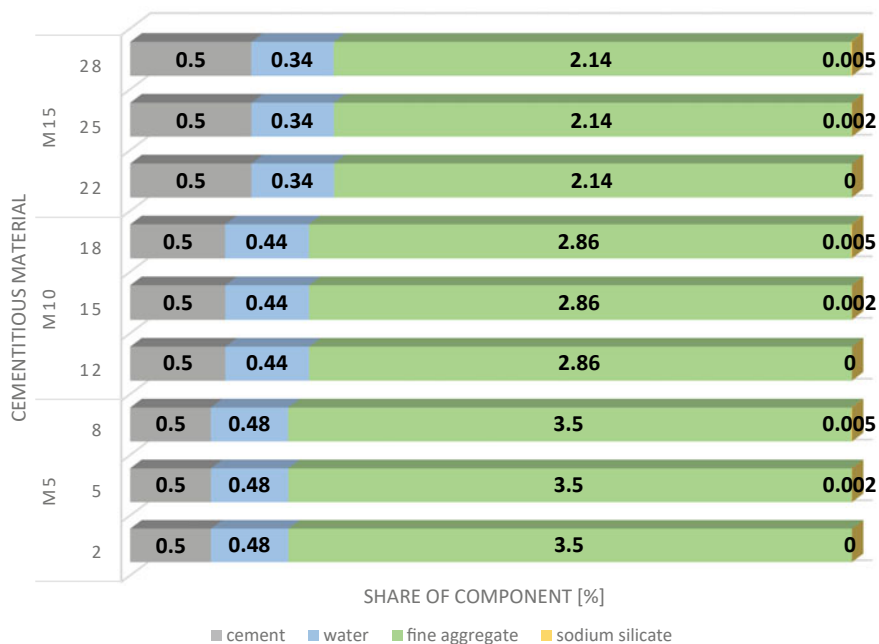
Fig. 4.4 Components of the cementitious mortars

Table 4.1 Tests of the capillary suction of the granite fine aggregate

Granite fine aggregate				
Time (h)	Height (mm)			
	Sample 1	Sample 2	Sample 3	Average
0.12	51	48	50	49.67
0.25	79	76	78	77.67
0.5	101	98	100	99.67
1	136	132	135	134.33
2	178	170	178	175.33
3	195	189	193	192.33
5	220	215	221	218.67
10	235	227	236	232.67
24	249	241	250	246.67
48	261	256	264	260.33
72	275	269	277	273.67
96	280	274	284	279.33
120	291	286	298	291.67
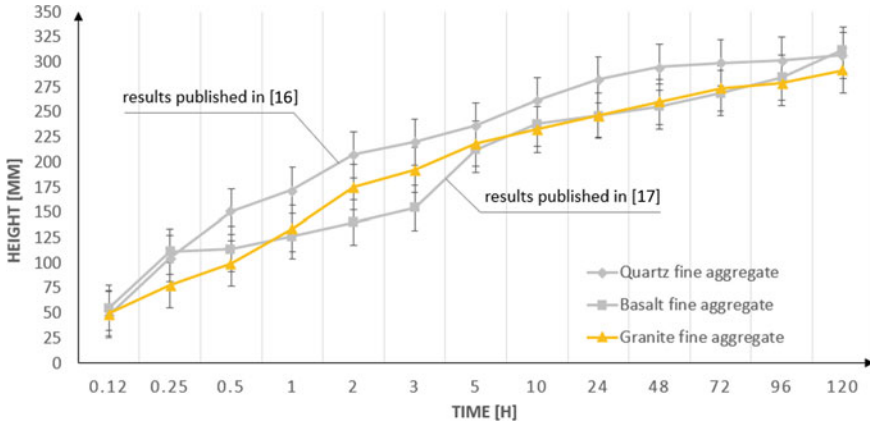
Fig. 4.5 Capillary suction of the granite, quartz and basalt fine aggregates—a comparison

Figure 4.5 presents a comparison of the capillary suction of three different fine aggregates: granite, quartz and basalt. In the first fifteen minutes of the tests, the capillary suction of the basalt and quartz fine aggregate was similar. However, the granite fine aggregate had about a 20% lower capillary suction than the quartz and basalt fine aggregates. From the 15th minute to about the 96th hour of the research, the capillary suction of the granite and quartz fine aggregates was similar, whereas the capillary suction of the basalt fine aggregate was lower when compared to the other fine aggregates. In the last hour of the research, the quartz and basalt fine aggregates had a higher capillary suction than the granite fine aggregate. The granite fine aggregate was about 4.9% more resistant to capillary suction than the quartz fine aggregate, and about 6.6% more resistant to capillary suction than the basalt fine aggregate. The granite fine aggregate had the most favourable result with regards to capillary suction.

4.3.2   The Capillary Suction of the Prepared Cementitious Materials

Figure 4.6 shows a comparison of the capillary suction of the M5 cementitious material that was prepared with the addition of sodium silicate and three different fine aggregates: quartz, basalt and granite. A total of six different cementitious material bars was compared (the composition of the cementitious mortar bars is presented in Fig. 4.4). Each cementitious material bar was measured thirteen times.

Figure 4.6a shows the capillary suction of the three M5 cementitious material bars that had a lower amount of sodium silicate. The first bar also had the quartz fine aggregate, the second bar—the basalt fine aggregate and the third bar—the granite fine aggregate. From the beginning of the research to about the 48th hour, the
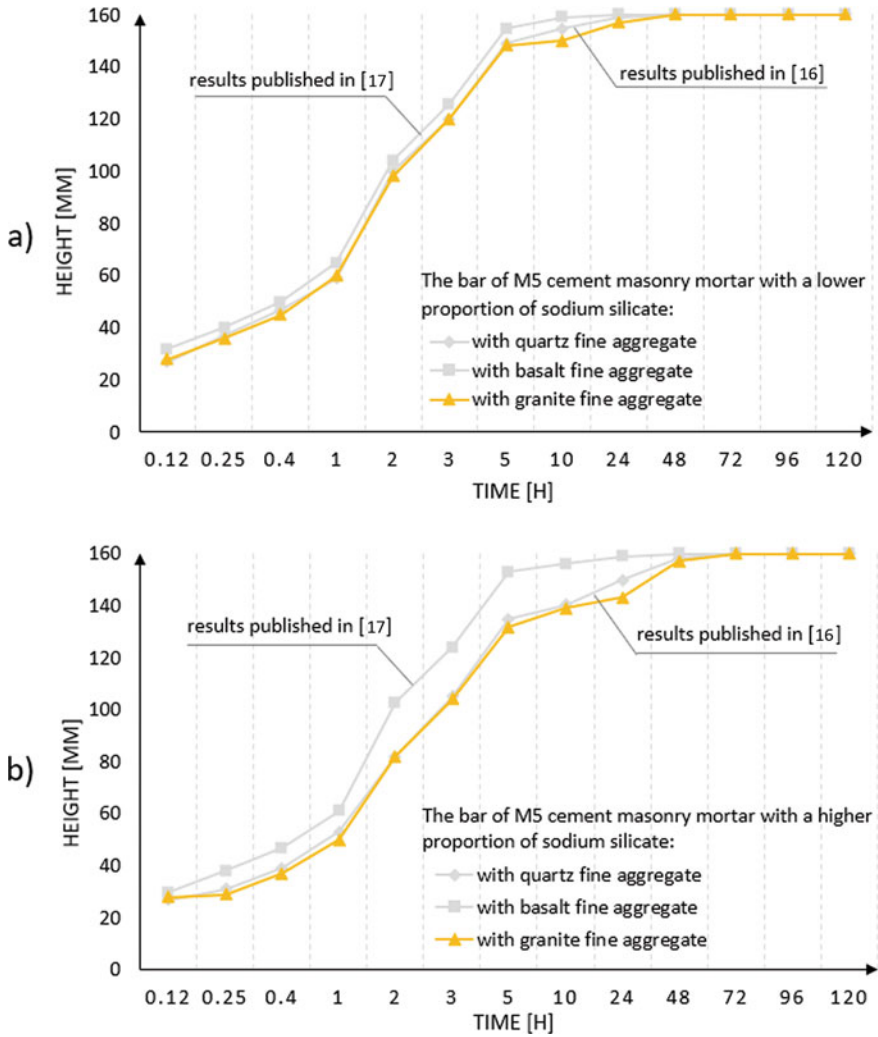
Fig. 4.6 Capillary suction of the M5 cementitious material bars with the granite, quartz and basalt fine aggregates: **a** with a lower proportion of the additive and **b** with a higher proportion of the additive

cementitious material with the granite fine aggregate and the cementitious material with the quartz fine aggregate had similar results. At the same time, the cementitious material with the basalt fine aggregate had about a 6% higher capillary suction than the other bars. After the 48th hour of testing, all the bars achieved the same result.

Figure 4.6b presents the capillary suction of the three M5 cementitious material bars that a higher amount of sodium silicate. The first bar also had the quartz fine aggregate, the second bar—the basalt fine aggregate and the third bar—the granite

fine aggregate. As was the case in Fig. 4.6a, from the beginning of the research to about 48 h, the cementitious material with the granite fine aggregate and the cementitious material with the quartz fine aggregate had similar results. At the same time, the cementitious material with the basalt fine aggregate had about a 12.5% higher capillary suction than the other bars. After the 48th hour of testing, all the bars achieved the same result.

Figure 4.7 shows a comparison of the capillary suction of the M10 cementitious material, which was prepared with the addition of sodium silicate and three different fine aggregates: quartz, basalt and granite. A total of six different cementitious material bars were compared (the composition of the cementitious mortar bars is presented in Fig. 4.4). Each cementitious material bar was measured thirteen times.

The capillary suction of the three M5 cementitious material bars that had a lower amount of sodium silicate is presented in Fig. 4.7a. The first bar also had the quartz fine aggregate, the second bar—the basalt fine aggregate, and the third—the granite fine aggregate. The results obtained for the cementitious material with the quartz fine aggregate and the cementitious material with the granite fine aggregate were similar. In turn, the cementitious material with the basalt fine aggregate had about a 6% higher capillary suction index than the other cementitious materials.

Figure 4.7b shows the capillary suction of the three M5 cementitious material bars that had a higher amount of sodium silicate. The first bar also had the quartz fine aggregate, the second bar—the basalt fine aggregate and the third—the granite fine aggregate. The bar of the M10 cementitious material (with the quartz fine aggregate) and the bar of the M10 cementitious material (with the granite fine aggregate) had a lower index of capillary suction when compared to the cementitious material bar with the basalt fine aggregate. However, the M10 cementitious material with a greater amount of the additive had a more favourable result than the M10 cementitious material with a lower amount of sodium silicate, regardless of the type of used fine aggregate. In turn, the bar of the M5 cementitious material had a higher capillary suction than the M10 cementitious material bars. For the production of the M10 cementitious material, less fine aggregate was used than in the case of the M5 cementitious material. The cementitious material with the basalt fine aggregate and a higher proportion of sodium silicate had the least favourable result. The capillary suction rate of the cementitious material with the basalt fine aggregate was 12% higher than the capillary suction rate of the cementitious material with the quartz fine aggregate, and 10% higher than the capillary suction index of the cementitious material with the granite fine aggregate. However, the capillary suction of the M10 cementitious material with the granite fine aggregate and a higher amount of sodium silicate was about 53% lower than the capillary suction of the M10 cementitious material with the granite fine aggregate and a lower amount of the additive.

Figure 4.8 presents a comparison of the capillary suction of the M15 cementitious material that was prepared with the addition of sodium silicate and the three different fine aggregates: quartz, basalt and granite. A total of six different cementitious material bars were compared (the composition of the cementitious mortar bars is presented in Fig. 4.4). Each cementitious material bar was measured thirteen times.

Fig. 4.7 Capillary suction of the M10 cementitious material bars with the granite, quartz and basalt fine aggregates: **a** with a lower proportion of the additive and **b** with a higher proportion of the additive

Figure 4.8a shows the capillary suction of the three M15 cementitious material bars that had a lower amount of sodium silicate. The first bar also had the quartz fine aggregate, the second bar—the basalt fine aggregate and the third—the granite fine aggregate. The result of the capillary suction of the cementitious material with the basalt fine aggregate and a lower amount of sodium silicate was 8% higher than

Fig. 4.8 Capillary suction of the M15 cementitious material bars with the granite, quartz and basalt fine aggregates: **a** with a lower proportion of the additive and **b** with a higher proportion of the additive

the capillary suction of the cementitious material with the quartz fine aggregate and a lower amount of sodium silicate and 6.5% higher than the result of the capillary suction of the cementitious material with the granite fine aggregate.

Figure 4.8b shows the capillary suction of the three M15 cementitious material bars that had a higher amount of sodium silicate. The first bar also had the quartz fine aggregate, the second bar—the basalt fine aggregate and the third bar—the
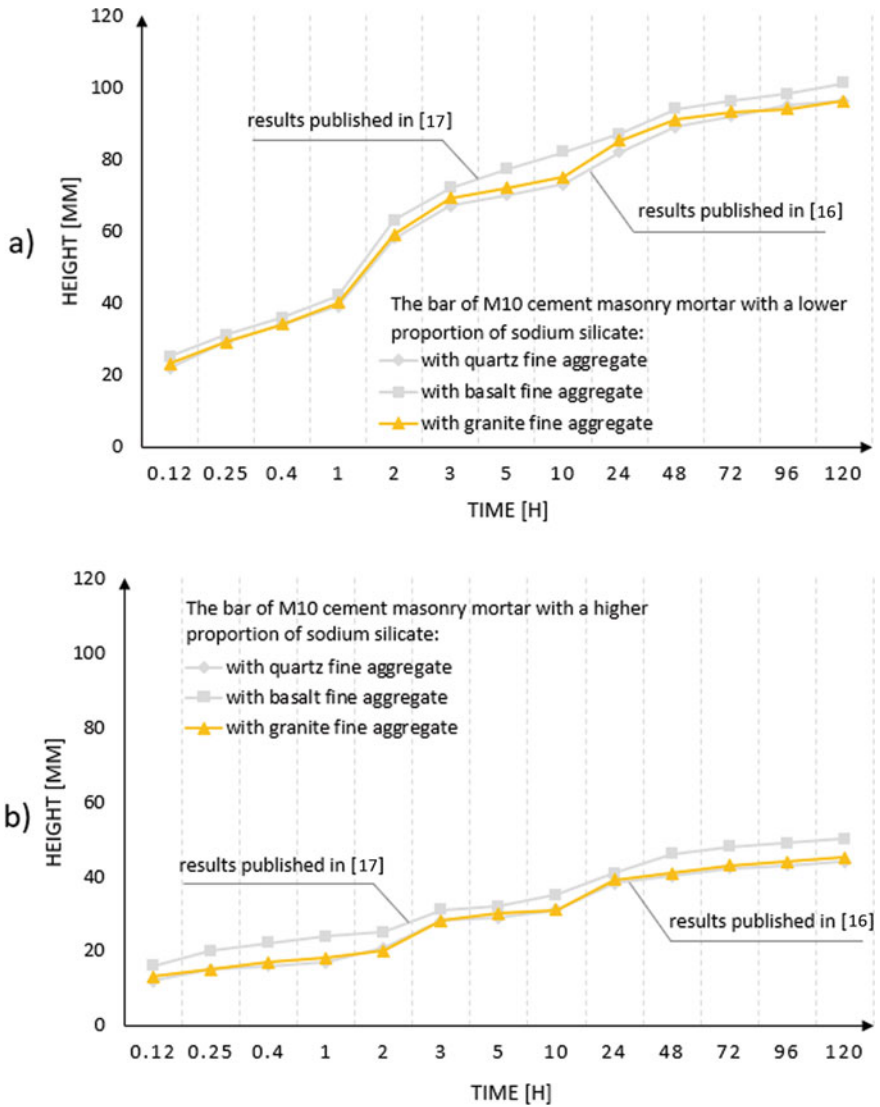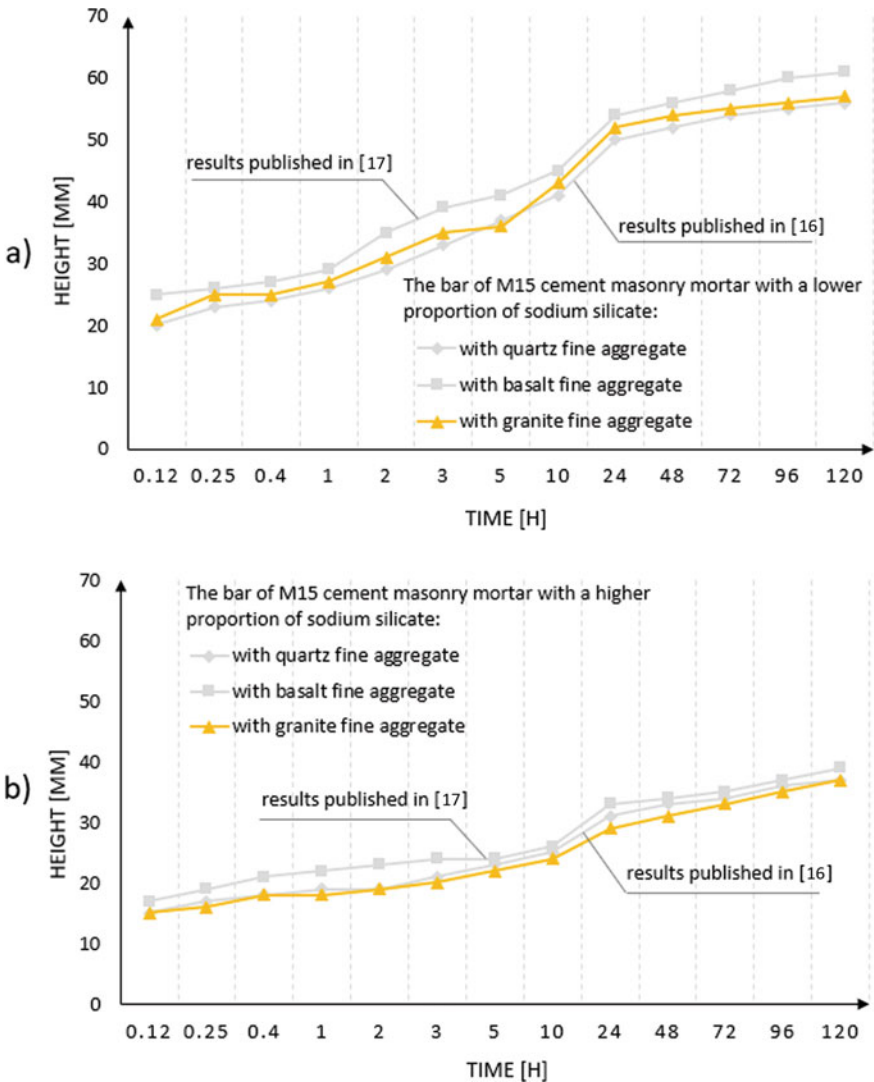
granite fine aggregate. In this study, the bar of the M15 cementitious material with the quartz fine aggregate, and the bar of the M15 cementitious material with the granite fine aggregate had the same results (37 mm). However, the M15 cementitious material bar with the basalt fine aggregate had the least favourable result (39 mm). The capillary suction index of the cementitious material with the basalt fine aggregate was 5% higher than the capillary suction index of the cementitious material with the quartz fine aggregate, and the cementitious material with the granite fine aggregate. However, the capillary suction of the M15 cementitious material with the granite fine aggregate and a higher amount of sodium silicate was about 35% lower than the capillary suction of the M15 cementitious material with the granite fine aggregate and a lower amount of sodium silicate.

Figure 4.9a shows a comparison of the capillary suction of the granite, quartz and basalt fine aggregates, the M5 cementitious material with the granite fine aggregate without the additive, the M5 cementitious material with the quartz fine aggregate without the additive and the M5 cementitious material with the basalt fine aggregate without the additive. Figure 4.9b presents a comparison of the capillary suction of the granite, quartz and basalt fine aggregates, the M10 cementitious material with the granite fine aggregate without the additive, the M10 cementitious material with the quartz fine aggregate without the additive and the M10 cementitious material with the basalt fine aggregate without the additive. Figure 4.9c shows a comparison of the capillary suction of the granite, quartz and basalt fine aggregates, the M15 cementitious material with the granite fine aggregate without the additive, the M15 cementitious material with the quartz fine aggregate without the additive and the M15 cementitious material with the basalt fine aggregate without the additive.

The fine aggregates, when compared to the cementitious materials, had less favourable results in terms of their capillary suction.

4.4 Conclusions

In this research, the capillary suction of cementitious materials with sodium silicate (two different proportions: 0.002 and 0.005 kg) and granite fine aggregate was investigated. The research focused on the design of a cementitious material with a low capillary suction. M5, M10 and M15 cementitious materials were used for testing. The obtained results were compared with previous research concerning quartz and basalt fine aggregates. It was observed that the used additive (sodium silicate) had a positive influence on the capillary suction index of the prepared cementitious materials.

The conducted research also showed that:

- The capillary suction of the M5 cementitious material with the granite fine aggregate and a greater amount of sodium silicate was about 77% higher than the capillary suction of the M15 cementitious material with the granite fine aggregate and a greater amount of sodium silicate.
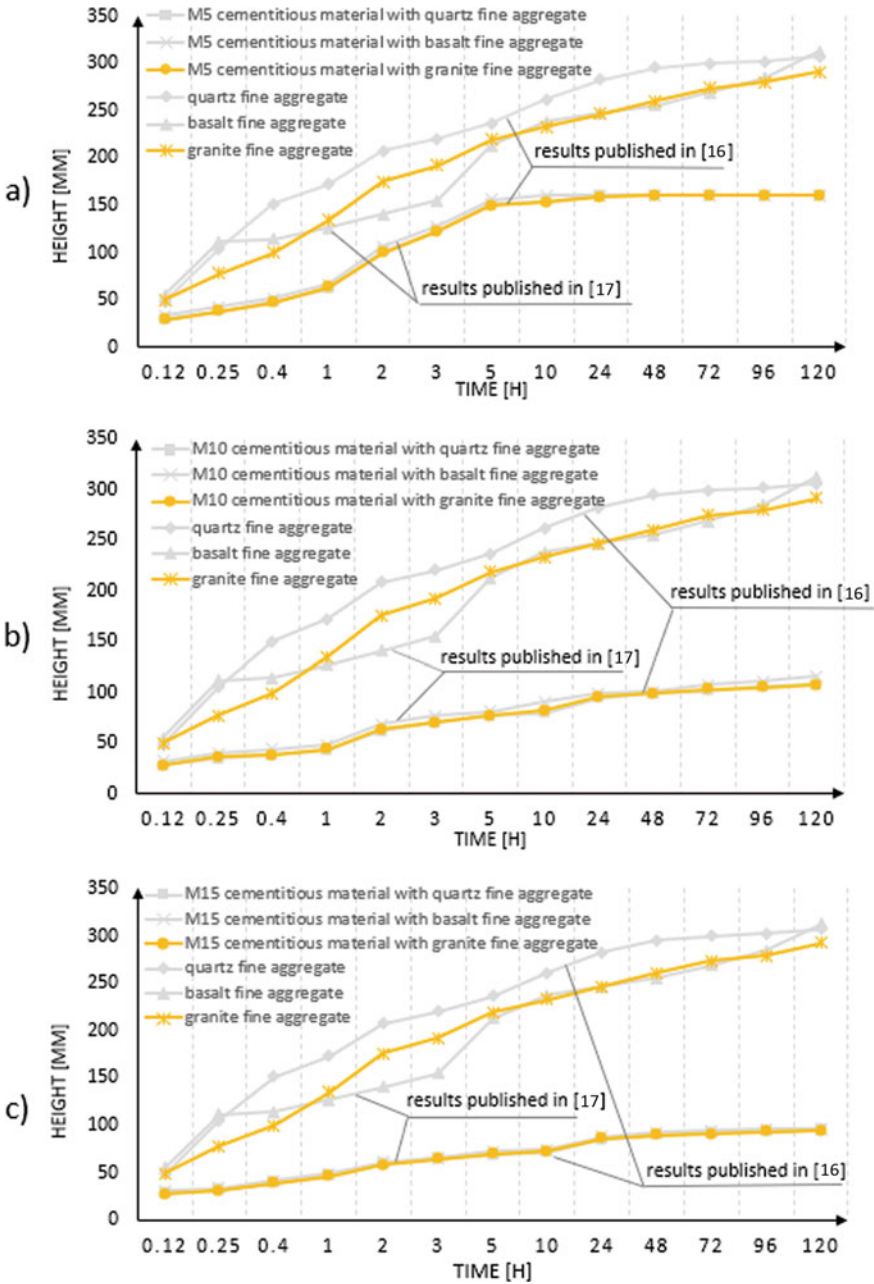
Fig. 4.9 Comparison of the capillary suction of the granite, quartz and basalt fine aggregates with: **a** the M5 cementitious material bar without sodium silicate, **b** the M10 cementitious material bar without sodium silicate and **c** the M 15 cementitious material bar without sodium silicate

- The M15 cementitious material with a greater amount of sodium silicate had the most favourable result. The cementitious material with the quartz fine aggregate and the cementitious material with the granite aggregate obtained the same results with regards to capillary suction. In turn, the M10 cementitious material with the basalt fine aggregate had about a 5% higher capillary suction index when compared to the other two cementitious materials. The least fine aggregate when compared to the M5 and M10 cementitious materials was added to the M15 cementitious material.
- The addition of sodium silicate to the cementitious materials reduced their capillary suction. The M15 cementitious material with the granite fine aggregate had a 60% higher capillary suction index than the M15 cementitious material with the granite fine aggregate and a greater amount of sodium silicate.

To sum up, sodium silicate, the type of fine aggregate and the type of cement mortar had a direct impact on the capillary suction of the cement mortars. Very promising results were obtained for the M15 cementitious materials with a greater amount of sodium silicate. Therefore, this additive, and the type of cement mortar, should be applied in cementitious materials in order to reduce capillary suction. The perspectives for future research include the analysis of the capillary suction of brick walls made using cement mortar with the addition of sodium silicate.

References

Aval SBB, Ghabdian M, Noori M, Altabey W (2022) Simultaneous effect of temperature, shrinkage, and self-weight creep on RC beams: a case study. Proc Inst Mech Eng Part l: J Mater Des Appl 236(5):1020–1036

Bogue R (1948) The chemistry of Portland cement. Am Chem Soc 51–56

Clim D, Groll L, Diaconu L (2017) Moisture—the main cause of the degradation of historic buildings. Buletinul Institutului Politehnic Din Iaşi 63(67):3

Czapik P, Boroń M, Kuza D (2020) O degradacji zapraw cementowych z kruszywem ze szkła odpadowego. Inżynieria i Budownictwo 76

Dondelewski H, Januszewski M (2008) Betony Cementowe. Zagadnienia wybrane, Wydawnictwa Naukowo-Techniczne, pp 46–51

Double DD, Hellawell A, Perry SJ (1978) The hydration of Portland cement. Roy Soc 359(1699)

Hoła A, Czarnecki S (2022) Brick wall moisture evaluation in historic buildings using neural networks. Autom Constr 141:104429

Karagiannis N, Bakolas A, Karoglou M, Krokida M, Moropoulou A (2018) The influence of dynamic environmental conditions on capillary water uptake of building materials. J Building Phys 42(4):506–526

Karoglou M, Moropoulou A, Giakoumaki A, Krokida MK (2005) Capillary rise kinetics of some building materials. J Colloid Interface Sci 284(1):260–264

Kon O, Caner İ (2022) The effect of external wall insulation on mold and moisture on the buildings. Buildings 12(5):521

Moropoulou A, Avdelidis N, Theoulakis P, Koui M (2001) Thermography as an evaluation tool for studying the movement of water through various porous materials: capillary rise and evaporation. In: Proceeding SPIE, vol 4360. Thermosense XXIII, p 4360

Nedelec A, Bouchez J (2015) Granites petrology structure geological setting and metallogeny. Oxford University Press, pp 91–127

Popek M, Wapińska B (2009) Podstawy budownictwa. WSiP 76–77

Pratiwi SM, Wijayanto P, Putri CA (2020) Diagnosis of capillary rise in heritage building. In: IOP conference series: earth and environmental science, vol 780

Saberian M, Jahandari S, Li J, Zivari F (2017) Effect of curing, capillary action, and groundwater level increment on geotechnical properties of lime concrete: experimental and prediction studies. J Rock Mech Geotech Eng 9(4):638–647

Szemiot N, Sadowski Ł, Czarnecki S (2022) Engineering and manufacturing of cementitious mortars with low capillary suction for applications in historical buildings. In: Proceedings in engineering mechanics—research, technology and education

Szemiot N, Sadowski Ł (2022) The design of cement mortar with low capillary suction: understanding the effect of fine aggregate and sodium silicate. Materials 15:1517

Woźniak Z, Chajec A (2022) Wpływ mączki granitowej na wybrane właściwości zapraw cementowych. Materiały Budowlane 4:58–61

Wysocka M, Szypcio Z, Tymosiak D (2013) Prędkość wznoszenia kapilarnego w gruntach niespoistych. Budownictwo i Inżynieria Środowiska 4:167–172

Yik FWH, Sat PSK, Niu JL (2004) Moisture generation through Chinese household activities. Indoor and Built Environ 13(2):115–131

Zajceva L, Lucyk E, Latypova T, Latypov V, Fedorov P, Salamanova M (2021) Influence of the type of aggregate from industrial waste on corrosion resistance of modified fine-grained concrete. Buildings 11(8):352

Chapter 5
The Production Process of Foamed Geopolymers with the Use of Various Foaming Agents

P. Bazan, M. Łach, B. Kozub, B. Figiela, and K. Korniejenko

Abstract The paper presents the possibility of producing foamed geopolymer materials with various foaming agents. Geopolymer is an amorphous aluminosilicate polymer made from the synthesis of silicon (Si) and aluminum (Al), geologically obtained from minerals. Geopolymers contain long chains (copolymers) of aluminum–silicon and aluminum, stabilizing metal cations, most often sodium, potassium, lithium or calcium, and bound water, in addition, there are usually various mixed phases: silicon oxide, unreacted aluminosilicate substrate, and—sometimes—crystallized aluminosilicates of the type zeolite. Most methods of geopolymer synthesis come down to one process: The fine and dried pozzolanic materials are mixed with an aqueous solution of a suitable silicate with the addition of a strong base—usually concentrated sodium or potassium hydroxide. The resulting paste behaves like cement. Fly ash from the Heat and Power Plant in Skawina (Poland) was used as a precursor for the production of geopolymer. The activation process was performed with a 10-molar solution of sodium hydroxide NaOH in combination with a solution of sodium silicate. The foaming agents were perhydrol, aluminum powder, and the Sika® Lightcrete-400 foaming saucer—an organic surfactant for the production of low-emission, lightweight, porous concrete. The produced foamed geopolymer materials were subjected to strength and thermal conductivity tests. The properties of the foams are related to the used foaming agent, but it is not the only factor affecting the quality of the materials. In the production of samples, the crucial factors are mixing the materials, the amount of the added additive, and the temperature of the geopolymerization process.

Keywords Geopolymers · Foaming agents · Thermal conductivity · Compressive strength

P. Bazan (✉) · M. Łach · B. Kozub · B. Figiela · K. Korniejenko
Department of Materials Engineering, Faculty of Materials Engineering and Physics, Tadeusz Kosciuszko Cracow University of Technology, Cracow, Poland
e-mail: patrycja.bazan@pk.edu.pl

5.1 Introduction

Portland cement and concretes based on it are construction materials whose production is quite harmful to the environment. Carbon emissions from Portland cement production in 2020 are estimated to be around 4.8 billion tones (Mehta 2001; Singh and Middendorf 2020). Therefore, the scientific and industrial community has been looking for an alternative to this material for many years. An option to such can be inorganic polymers, formed from polycondensation of aluminosilicate waste (containing silicates with alkali), called geopolymers (Yang et al. 2017; Król and Błaszczyński 2013). Currently, most research is carried out on fly ash-based geopolymers (Sitarz et al. 2020; Assi et al. 2016), metakaolin (Duxon et al. 2007), rice husk ash (Kaur et al. 2018), or slag (Nguyen et al. 2018). Research on this type of materials has shown that these materials are characterized by high strength, corrosion resistance, flame retardance, and durability (Thokchom et al. 2010; Rickard et al. 2013). The construction sector is most often indicated as using geopolymer materials, but also increasingly as a neutralizing material and more environmentally friendly (Duxon et al. 2006; Grant Norton and Provis 2020; Fan et al. 2018; Deb et al. 2014). To date, dozens of works on geopolymers based on various types of waste have been carried out, and the great potential of this type of materials has been indicated. However, most literature focuses on solid materials and their strength properties. Only recently, attention has been focused on the production of porous geopolymeric materials characterized by low thermal conductivity (Feng et al. 2015). Foamed geopolymer is obtained by chemical or mechanical foaming (Zhang et al. 2014). Research on foamed geopolymers has shown a lower thermal conductivity, usually around 10–50% of that of ordinary concrete (Zhang et al. 2015). It also has lower energy consumption and less environmental burden than conventional foam concrete (Yang et al. 2014; Duxson et al. 2007). The most common application is the filling of insulation, partitions, and voids (Ramamurthy et al. 2009) For non-mechanical thermal purposes, the thermal conductivity of the typically foamed geopolymer is generally from 0.072 to 0.48 W/(m K). The thermal properties of geopolymers are influenced by parameters such as size, distribution, pore shape, type and content of the foaming agent, type and content of binder, activator content, temperature, and method of foaming (Jelle et al. 2010; Ducman and Korat 2016; Kamseu et al. 2015; Vucinic et al. 2003; Studart et al. 2006; Kim et al. 2009). Research on geopolymers has identified another critical factor in the production of geopolymers—water. Water is responsible for dissolving the aluminosilicate precursors, transporting ions, and the polycondensation process of Si and Al monomers; in addition, water is responsible for the appropriate lightness of the mixture, which is a key factor in foaming materials; it can affect the foam structure, its regularity, porosity, and the stability of the bubbles formed, therefore, it is necessary to know the effect of water in the production of foamed geopolymers (Lizcano et al. 2012; Perera et al. 2006; Song et al. 2000).

5.2   Materials and Method of Sample Preparation

Fly ash from the Heat and Power Plant in Skawina (Poland) was used as a precursor for the production of geopolymer. The activation process was carried out using a 10-molar sodium hydroxide solution (NaOH) combined with a sodium silicate solution. The foaming agents were hydrogen peroxide (perhydrol 36%, Biomus), aluminum powder (powder, max. particle size 60-μm, purity 99.9%, Sigma-Aldrich), and conventional foam concentrate used in concrete (Sika® Lightcrete-400)—an organic agent surfactant for the production of low-emission, lightweight, porous concrete. Syringaldehyde stabilizer (Sigma-Aldrich) was also used for the geopolymer blend. The process of preparing the foamed geopolymer is shown in Fig. 5.1.

The work was divided into two stages. Part I involved the preparation of foamed geopolymers with three different blowing agents and comparing strength properties and thermal conductivity. Then, based on the first step, two foaming agents were selected and an attempt was made to optimize the foaming process with the addition of H_2O. The type and composition of the manufactured materials are presented in Table 5.1.
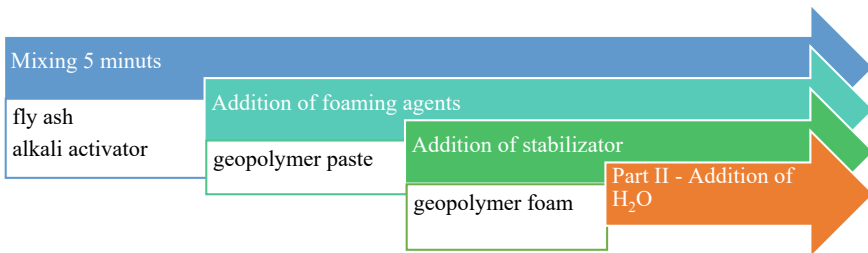
Fig. 5.1 Process of producing geopolymer foams

Table 5.1 List of manufactured materials

Part	Index	Precursor—fly ash (g)	Activator—10 molar (g)	Foaming agent (g)	Stabilizer (g)	Water (g)
I	1	500	460	Sika, 60	5	–
	2	500	460	H_2O_2, 25		–
	3	500	460	Al, 1		–
II	4	500	460	H_2O_2, 25		21
	5	500	460	H_2O_2, 25		43
	6	500	460	Al, 1		21
	7	500	460	Al, 1		43

5.3   Methods of Testing

As part of the research, the produced materials were tested for compressive strength and thermal conductivity. The compressive strength of the composites was carried out according to EN 12,390-3: 2019-07: Concrete tests-part 3: Compressive strength. It was tested on the MATEST 3000 kN (Matest, Treviolo, Italy). Cubic samples of 50 × 50 × 50 mm were prepared for the test and seasoned for 28 days at room temperature. Each geopolymer composite was tested on five samples. The heat conduction coefficient was tested on the HFM 446 plate apparatus (Wittelsbacherstrasse, Germany). In a heat flow meter (HFM), the test specimen is placed between two heated plate-controlled temperatures. For the tests, panels with dimensions of approximately 200 × 200 × 25 mm were made, dried to a constant weight after 28 days of stabilization, and then tested.

5.4   Results and Discussion

5.4.1   Part I—Comparison of Foaming Agents

The first step compared the performance of the three types of tensioning agents, perhydrol, aluminum powder, and the conventional foam concentrate used in concrete. The properties of foams are related to the foaming agent used, but it is not the only factor affecting the quality of the materials. In the production of samples, the process of mixing the materials, the amount of added additive, and the temperature of the geopolymerization process are also important factors. In the production process of geopolymer foam, chemical and mechanical methods are distinguished. Another division is the direct and indirect introduction of gas into the material. Blowing agents such as aluminum oxide or perhydrol, in combination with calcium oxides present in the matrix and binder, emit hydrogen, which gives porosity to the geopolymer structure. During this reaction, hydrated calcium silicate is released, while hydrogen, being lighter than air, escapes from the geopolymeric mass, increasing the mold volume. After some time, the hydrogen completely escapes from the mass and is replaced with air filling the spaces of the foamed geopolymer. Aluminum powder reacts with calcium oxides and calcium hydroxides. In turn, hydrogen peroxide (perhydrol) reacts with calcium chlorides, so it is a chemical foaming. When using a conventional foaming agent, mechanical tamping first made the foam. Then, the foam was mixed with the geopolymer mass, so this method belongs to the direct/mechanical foaming method. Table 5.2 gives the produced foamed geopolymer materials.

The compressive strength and thermal conductivity test results of the manufactured materials are shown in Figs. 5.2 and 5.3. Photographs were also taken on a Keyence VH-7000 digital microscope at 20 × and 30 × magnification to compare the pore size. The microscopic photos are shown in Figs. 5.4, 5.5 and 5.6.

Table 5.2 List of materials manufactured in part I

Part	Index	Precursor—fly ash (g)	Activator—10 molar (g)	Foaming agent (g)	Stabilizer (g)
I	Foam	500	460	Sika, 60	5
	H_2O_2	500	460	H_2O_2, 25	
	Aluminum	500	460	Al, 1	
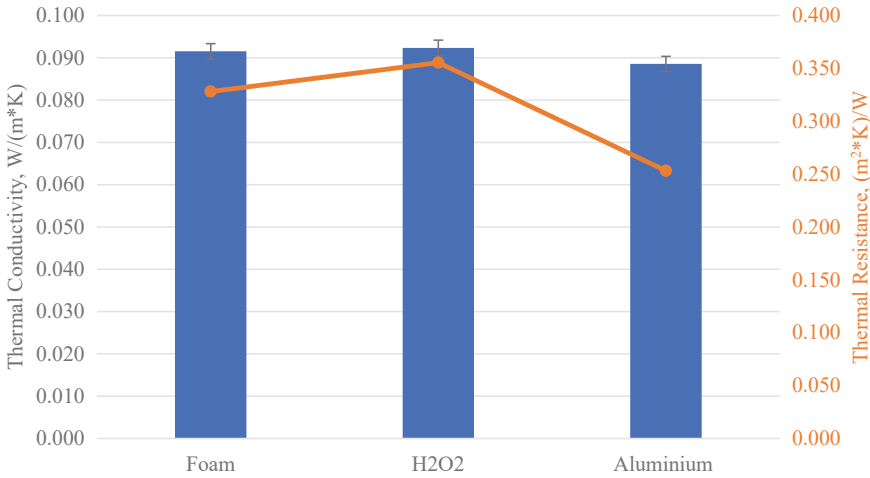
Fig. 5.2 Comparison of the conductivity and thermal resistance of the manufactured materials
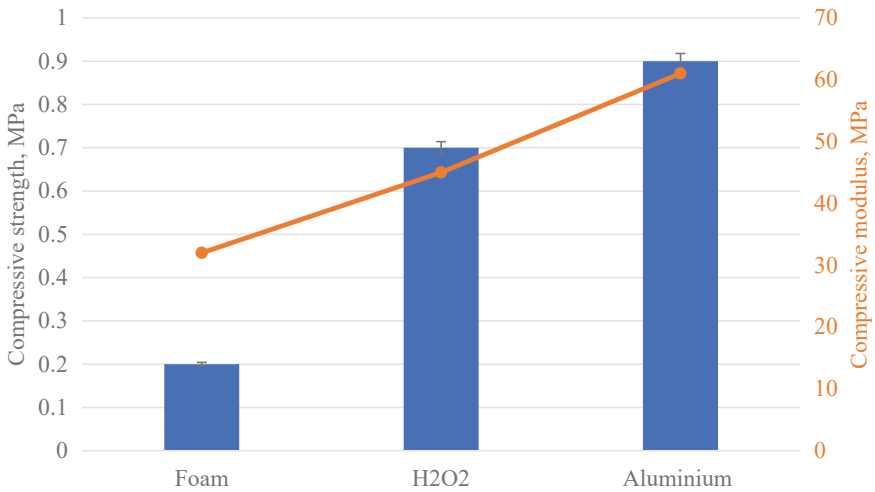
Fig. 5.3 Comparison of the compressive strength and the compressive modulus of the produced materials
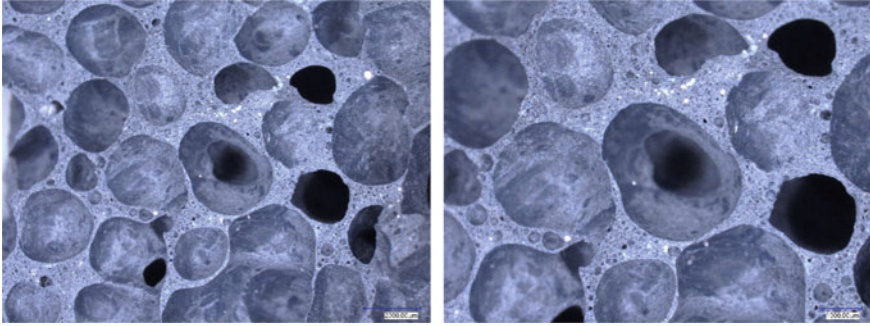
Fig. 5.4 Geopolymer foamed with Silka foaming agent
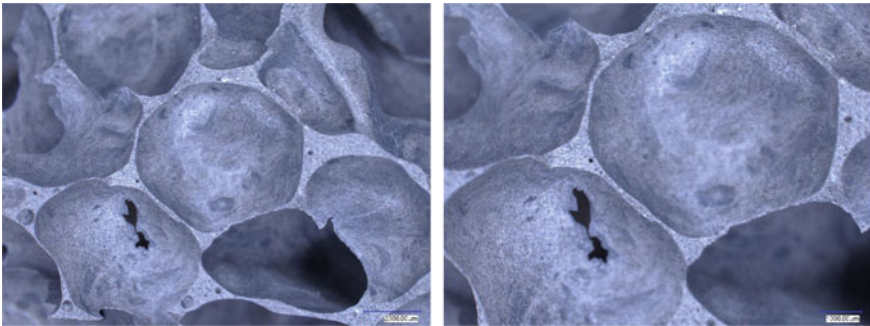
Fig. 5.5 Geopolymer foamed with 36% H_2O_2
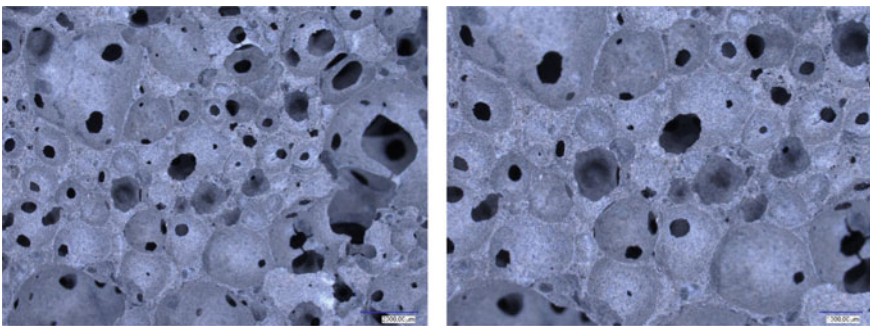
Fig. 5.6 Geopolymer foamed with aluminum powder

The thermal conductivity tests showed little difference between the material foamed with a conventional foaming agent and the use of perhydrol. The lowest thermal conductivity characterized the material foamed with aluminum powder. The thermal conductivity was 0.089 W/(m K) other researchers also investigated foamed

geopolymer materials using H_2O_2 and aluminum powder. The result of thermal conductivity oscillated between 0.07 and 0.22 W/(m K) (Feng et al. 2015; Novais et al. 2016; Łach et al. 2021).

The photos taken on the samples showed that the foamed material with a conventional foaming agent was characterized by an average pore size within 2500 μm and a mixed porosity of both open and closed pores. The highest porosity described the material foamed with H_2O_2. The average pore size was 4000–5000 μm, and closed porosity was observed predominantly. The smallest pore size characterized the material foamed with aluminum powder. The size of the pores ranged from 1000 to 1500 μm, and there were more of them than in the case of the other two materials.

On the other hand, it was observed that the pores cracked during the foaming process. The analysis of the photos and the results of thermal conductivity confirm the conclusions pointed by other researchers that the greater the number of pores containing air, the lower the density of the material, and thus, the decrease in the value of thermal conductivity. However, some sources confirm the opposite relationship (Wongsa et al. 2018; Demirboğa and Gül 2003).

The results of the strength tests showed that also in this case, the material foamed with aluminum powder was characterized by the best properties. On the other hand, the material foamed with a concrete foam concentrate demonstrated the lowest compressive strength. This strength was only 0.2 MPa, which according to the JC/T2200-2013 standard for insulation boards based on ordinary Portland cement (OPC) does not meet the strength conditions (> 0.4 MPa for 0.25 g/cm^3).

5.4.2 Part II—Influence of Water Addition

Based on stage I, materials foamed with perhydrol and aluminum powder were selected for further research. In the second stage, an attempt was made to regulate the pore size of foamed geopolymeric materials with the addition of water. The list of manufactured materials is presented in Table 5.3.

The water addition was selected on the basis of the research presented by Cui and Wang. The study conducted by the authors showed that increasing the water-to-solid (W/S) ratio affects the viscosity, pore characteristics, bulk density, compressive strength, and thermal conductivity. An increase in the water-to-solid ratio causes a

Table 5.3 List and mass composition of the produced materials

Part	Index	Precursor—fly ash (g)	Activator—10 molar (g)	Foaming agent (g)	Stabilizer (g)	Water (g)
II	H_2O_2_21	500	460	H_2O_2, 25	5	21
	H_2O_2_43	500	460	H_2O_2, 25		43
	Al_21	500	460	Al, 1		21
	Al_43	500	460	Al, 1		43
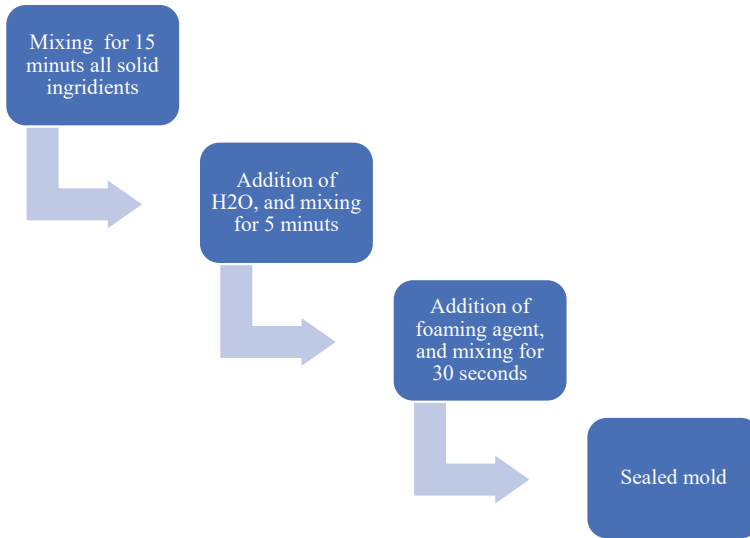
Fig. 5.7 Schematic of the sample manufacturing process

decrease in the viscosity of the geopolymer paste. Additional water also causing an increase in the proportion of micropores and macropores, which resulted in a decrease in thermal conductivity from 0.06 to 0.048 W/(m K) (Cui and Wang 2019).

Foamed geopolymer materials prepared according to the scheme shown in Fig. 5.7.

The results of the compression strength and thermal conductivity tests are shown in Figs. 5.8 and 5.9.

The obtained research results are in line with the conclusions presented by Ciu and Wang. The addition of water affects the viscosity of the geopolymer paste. As a result, H_2O-modified foams had larger pores and a larger pore volume, which resulted in deterioration of strength properties and positively affected thermal conductivity. However, the manufactured materials still meet the requirements of the JC/T2200-2013 standard for insulation boards based on Portland cement (OPC), which is a compressive strength > 0.4 MPa.

5.5 Conclusion

In this work, three types of foaming agents in geopolymer materials were compared. The manufactured materials were tested for compressive strength and thermal conductivity tests. The use of a conventional foaming agent in the production of foam concrete resulted in a geopolymer foam with thermal conductivity of 0.092 W/(m K) and insufficient compressive strength of 0.2 MPa. The best properties were obtained by geopolymer foam foamed with aluminum powder. The thermal conductivity was
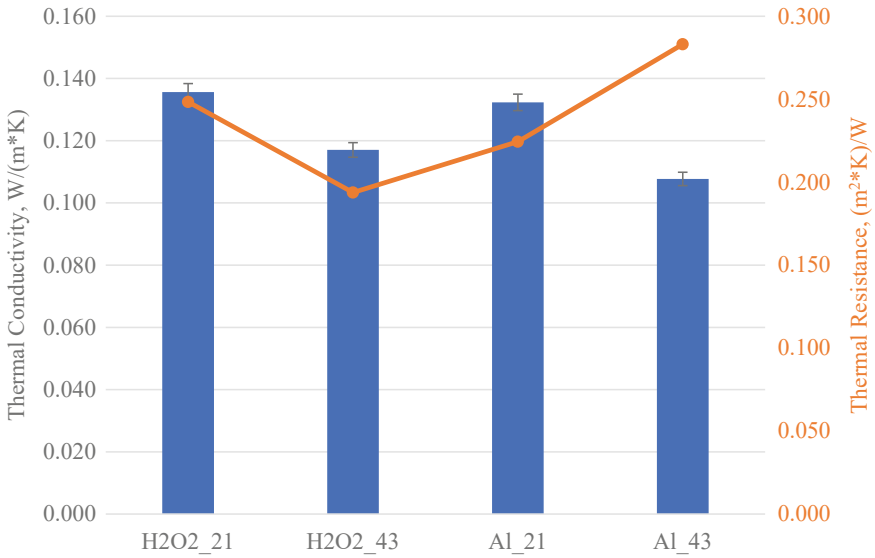
Fig. 5.8 Comparison of the thermal conductivity of materials modified with a variable amount of water
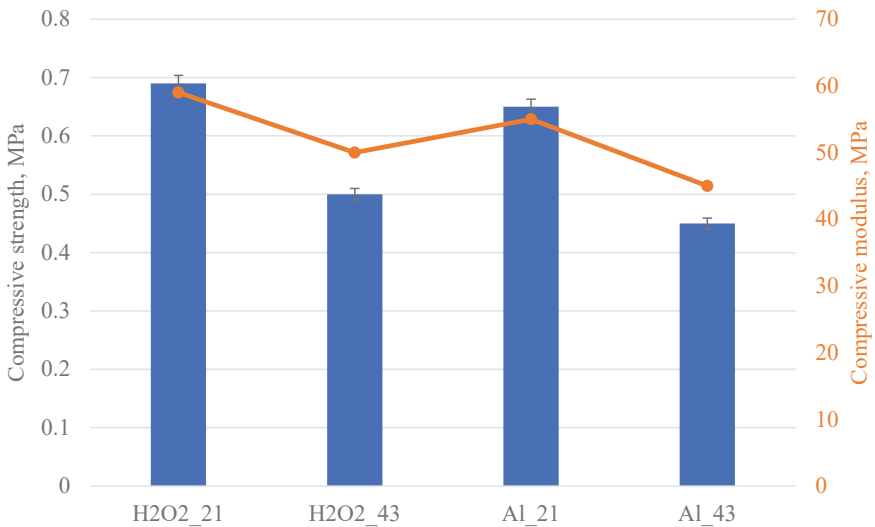
Fig. 5.9 Comparison of the compressive strength and the compressive modulus for materials modified with a variable amount of water

0.089 W/(m K) with a compressive strength of 0.9 MPa. As part of the research, attempts were made to regulate the pore size with the addition of water, influencing the viscosity of the geopolymer paste. The H_2O-modified foams had larger pores and a larger pore volume, which resulted in a deterioration of the strength properties. It was also observed that in the case of H_2O_2 foaming agent, the results were characterized by a greater scatter of the result than in the case of materials foamed with aluminum powder. This is because perhydrol is a foaming agent that is very sensitive to changes in the surface tension of the geopolymeric mass.

The presented research results indicate that geopolymer foams, although they cannot compete with insulating materials such as polystyrene or polyurethane foams, show great potential as building materials. It should be emphasized here that these materials meet the conditions of a closed-loop economy, are non-flammable materials, and are characterized by high mechanical strength.

References

Assi LN, Ghahari SA, Deaver E, Leaphart D, Ziehl P (2016) Improvement of the early and final compressive strength of fly ash-based geopolymer concrete at ambient conditions. Constr Build Mater 123:806–813

Cui Y, Wang D (2019) Effects of water on pore structure and thermal conductivity of fly ash-based foam geopolymers. Adv Mater Sci Eng 2019. https://doi.org/10.1155/2019/3202794

Deb PS, Nath P, Sarker PK (2014) The effects of ground granulated blast-furnace slag blending with fly ash and activator content on the workability and strength properties of geopolymer concrete cured at ambient temperature. Mater Des 62:32–39. https://doi.org/10.1016/j.matdes.2014.05.001

Demirboğa R, Gül R (2003) The effects of expanded perlite aggregate, silica fume and fly ash on the thermal conductivity of lightweight concrete. Cem Concr Res 33:723–727. https://doi.org/10.1016/S0008-8846(02)01032-3

Ducman V, Korat L (2016) Characterization of geopolymer fly-ash based foams obtained with the addition of Al powder or H_2O_2 as foaming agents. Mater Charact 113:207–213. https://doi.org/10.1016/j.matchar.2016.01.019

Duxon P, Fernansez-Jimenez A, Provis JL, Lukey GC, Palomo A, Van Deventer JS (2006) Geopolymer technology: the current state of the art. J Mater Sci 42:2917–2933

Duxon P, Mallicoat SW, Lukey GC, Kriven WM, Van Deventer JS (2007) The effect of alkali and Si/Al ratio on the development of mechanical properties of metakaolin-based geopolymers. Colloids Surf A Physicochemical Eng Asp 292:8–20

Duxon P, Provis JL, Lukey GC, van Deventer JSJ (2007) The role of inorganic polymer technology in the development of "green concrete." Cem Concr Res 37:1590–1597. https://doi.org/10.1016/j.cemconres.2007.08.018

Fan F, Liu Z, Xu G, Peng H, Cai CS (2018) Mechanical and thermal properties of fly ash based geopolymers. Constr Build Mater 160:66–81. https://doi.org/10.1016/j.conbuildmat.2017.11.023

Feng J, Zhang R, Gong L, Li Y, Cao W, Cheng X (2015) Development of porous fly ash-based geopolymer with low thermal conductivity. Mater Des 65:529–533. https://doi.org/10.1016/j.mat des.2014.09.024

Grant Norton M, Provis JL (2020) 1000 at 1000: Geopolymer technology—the current state of the art. J Mater Sci 55:13487–13489. https://doi.org/10.1007/s10853-020-04990-z

Jelle BP, Gustavsen A, Baetens R (2010) The path to the high performance thermal building insulation materials and solutions of tomorrow. J Build Phys 34:99–123. https://doi.org/10.1177/174 4259110372782

Kamseu E, Ngouloure ZNM, Ali BN, Zekeng S, Melo UC, Rossignol S, Leonelli C (2015) Cumulative pore volume, pore size distribution and phases percolation in porous inorganic polymer composites: relation microstructure and effective thermal conductivity. Energy Build. 88:45–56. https://doi.org/10.1016/j.enbuild.2014.11.066

Kaur K, Singh J, Kaur M (2018) Compressive strength of rice husk ash based geopolymer: the effect of alkaline activator. Constr Build Mater 169:188–192

Kim H, Lee S, Han Y, Park JK (2009) Control of pore size in ceramic foams: influence of surfactant concentration. Mater Chem Phys 113:441–444. https://doi.org/10.1016/j.matchemphys.2008.07.099

Król M, Błaszczyński TZ (2013) Geopolimery w Budownictwie. Izolacje 5:38–47

Łach M, Pławecka K, Bąk A, Lichocka K, Korniejenko K, Cheng A, Lin WT (2021) Determination of the influence of hydraulic additives on the foaming process and stability of the produced geopolymer foams. Materials (Basel) 14. https://doi.org/10.3390/ma14175090

Lizcano M, Gonzalez A, Basu S, Lozano K, Radovic M (2012) Effects of water content and chemical composition on structural properties of alkaline activated metakaolin-based geopolymers. J Am Ceram Soc 95:2169–2177. https://doi.org/10.1111/j.1551-2916.2012.05184.x

Mehta P (2001) Reducing the environmental impact of concrete. Concr Int 23:61–66

Nguyen H, Carvelli V, Adesanya E, Kinnunen P, Illikainen M (2018) High performance cementitious composite from alkali-activated ladle slag reinforced with polypropylene fibers. Cem Concr Compos 90:150–160

Novais RM, Ascensão G, Buruberri LH, Senff L, Labrincha JA (2016) Influence of blowing agent on the fresh- and hardened-state properties of lightweight geopolymers. Mater Des 108:551–559. https://doi.org/10.1016/j.matdes.2016.07.039

Perera DS, Vance E, Finnie KS, Blackford MG, Cassidy DJ (2006) Disposition of water in Metakaolinite based geopolymers. Adv Ceram Matrix Compos 75:225–236

Ramamurthy K, Kunhanandan E, Indu Siva Ranjani G (2009) A classification of studies on properties of foam concrete. Cem Concr Compos 31:388–396

Rickard WD, Vickers L, Van Reissen A (2013) Performance of fibre reinforced, low density metakaoline geopolymers under simulated fire conditions. Appl Clay Sci 73:71–77

Singh NB, Middendorf B (2020) Geopolymers as an alternative to Portland cement: an overview. Constr Build Mater 237:117455

Sitarz M, Hager I, Choińska M (2020) Evolution of mechanical properties with time of fly-ash-based geopolymer mortars under the effect of granulated ground blast furnace slag addition. Energies 13:1135

Song Z-L, Ma L-Q, Wu Z-J, He D-P (2000) Effects of viscosity on cellular structure of foamed aluminum in foaming process. J Mater Sci 35:15–20

Studart AR, Gonzenbach UT, Tervoort E, Gauckler LJ (2006) Processing routes to macroporous ceramics: a review. J Am Ceram Soc 89:1771–1789. https://doi.org/10.1111/j.1551-2916.2006.01044.x

Thokchom S, Ghosh P, Ghosh S (2010) Performance of fly ash based geopolymer mortars in sulphate solution. J Eng Sci Technol 3:31–38

Vucinic D, Miljanovic I, Rosic A, Lazic P (2003) Effect of Na_2O/SiO_2 mole ratio on the crystal type of zeolite synthesized from coal fly ash. J Serbian Chem Soc 68:471–478

Wongsa A, Sata V, Nuaklong P, Chindaprasirt P (2018) Use of crushed clay brick and pumice aggregates in lightweight geopolymer concrete. Constr Build Mater 188:1025–1034. https://doi.org/10.1016/j.conbuildmat.2018.08.176

Yang KH, Lee KH, Song JK, Gong MH (2014) Properties and sustainability of alkali-activated slag foamed concrete. J Clean Prod 68:226–233. https://doi.org/10.1016/j.jclepro.2013.12.068

Yang T, Han W, Wang X, Wu D (2017) Surface decoration of polyimide fiber with carbon nanotubes and its application for mechanical enhancement of phosphoric acid-based geopolymers. Appl Surf Sci 416:200–212

Zhang Z, Provis JL, Reid A, Wang H (2014) Geopolymer foam concrete: an emerging material for sustainable construction. Constr Build Mater 56:113–127

Zhang Z, Provis JL, Reid A, Wang H (2015) Mechanical, thermal insulation, thermal resistance and acoustic absorption properties of geopolymer foam concrete. Cem Concr Compos 62:97–105. https://doi.org/10.1016/j.cemconcomp.2015.03.013

Part III
Additive Manufacturing

Chapter 6
Mechanical and Physical Characterization of Parts Manufactured by 3D Printing

C. Oliveira, J. Rocha, and J. E. Ribeiro

Abstract Fused deposition modelling is an additive manufacturing technique, classified as one of the most popular 3D manufacturing processes, because of its low cost and easy usability, resulting in good quality products. However, the mechanical properties of manufactured pieces depend on the base material properties, manufacturing parameters and room conditions (temperature and moisture). For those reasons, to obtain the optimal conditions, three different types of experimental tests were performed: tensile, flexural and water absorption. These tests were carried out to determine ABS and PLA's mechanical and physical properties, which are the main materials used in FDM technique. Results showed that PLA has higher values of tensile and flexural strength comparatively to ABS and, in the other hand, ABS had greater weight of water absorption.

6.1 Introduction

Additive manufacturing (AM), also known as 3D printing, has been attracting interest from industry and the research community (Dizon et al. 2018); nowadays, not cheaper and faster AM techniques have been established, which can manufacture high print qualities. In addition, polymer materials for 3D printing are currently being produced with a wider range of properties (Chapiro 2016). Today, AM is being used to produce

C. Oliveira · J. Rocha · J. E. Ribeiro (✉)
Polytechnic Institute of Bragança, C. Sta. Apolónia, 5300-253 Bragança, Portugal
e-mail: jribeiro@ipb.pt

C. Oliveira
e-mail: a38202@alunos.ipb.pt

J. Rocha
e-mail: jrocha@ipb.pt

J. E. Ribeiro
CIMO, C. Sta. Apolónia, 5300-253 Bragança, Portugal

materials for different applications, namely automotive (Lee et al. 2017), electronics (MacDonald et al. 2014), robots (Lee et al. 2017), construction (Paolini et al. 2019), apparel (Hashemi Sanatgar et al. 2017), medicine (Souza et al. 2020), dentistry (Bhargav et al. 2018) aerospace (Blakey-Milner et al. 2021), military (Bird and Ravindra 2021) and others. However, in these practical applications, the parts manufactured by 3D-printing processes must withstand different quantities of mechanical stress imposed by the environment. Therefore, it is crucial to know the imposed strengths in each application, considering various loading conditions. Furthermore, the mechanical properties of the 3D-printed parts must be equal to those manufactured by traditional methods, such as injection moulding (Goh et al. 2017; Gao et al. 2015).

Additive manufacturing processes are classified in seven categories: powder bed fusion, binder jetting, material jetting, directed energy deposition, vat photo polymerization, sheet lamination and material extrusion (Gao et al. 2015). Among these, one of the most popular is the defused deposition modelling (FDM) technique (Crump 1991) and it is based on extrusion additive manufacturing systems. FDM is a material-melting method which utilizes a coil of thermoplastic filament such as PC, ABS and PLA with different diameters, that are melted and extruded through a heated nozzle (Vaezi et al. 2013). Even though, the referred materials are the most used in recent years, thermoplastic materials, like PEEK, with higher melting points have appeared (Hoskins et al. 2018). Because of this singular mechanism of FDM, the use of thermoplastics and its process of material-melting are its major limitations. So, it is essential to determine the mechanical properties (Algarni and Ghazali 2021) of the materials used in FDM process, mainly the ABS and PLA because they are the most employed. In addition, the resolution and the accuracy of the FDM process are also considered limitations, which must be evaluated and optimized (Charalampous et al. 2021).

The aim of this work is to define reference values for each pair of material printed, to enable the designer to make a pre-selection when starting the production of the parts. To achieve this, tests will be performed to obtain the mechanical and physical properties, such as tensile strength, bending strength and water absorption of specimens manufactured by FDM printers using ABS and PLA. The experimental values obtained will be compared with values from literature.

6.2   Experimental Procedure

The polymeric materials chosen to work on this project were ABS and PLA. Before the tensile test, the specimens were conditioned according to ASTM D618-13, in order to standardize the humidity and temperature conditions in which the models were subjected before the tensile test. Tensile tests were performed in accordance with ASTM D638-14 named "Standard Test Method for Tensile Properties of Plastic". The standard used for Flexion Test met the ASTM D790-17, "Standard Test Methods for Flexural Properties of Unreinforced and Reinforced Plastics and Electrical Insulating

Materials". To determine the water absorption, the procedure described in ASTM D570-98 (2010) was followed.

The printers used were the Big Builder Dual Feed printer, the Cube printer, and the Robox® Dual printer.

From the results of the tensile, bending and water absorption tests, values were obtained for the strength of the materials used. The percentage of water absorbed by them was also obtained. Furthermore, from the results, a brief characterization of these materials was obtained, in which they could be used to assist a designer in the adequate choice of materials for different applications.

Based on the results, it was concluded that the parts made by the FDM process using ABS and PLA are highly anisotropic, a consequence from the variation of the layers' orientation, of the extrusion temperature and the percentage of infilling, which affects mechanical strength, dimensions and geometry.

6.2.1 Tensile Test

Following the recommendations defined by ASTM D883 (ASTM 2020) standard, was chosen to manufacture the V type specimens (ASTM International 2014; American Society for Testing and Materials 2017) making rigid or semi-rigid plastic with thicknesses up to 4 mm. Five models were produced, with geometry dimensions in accordance with the standard for ABS and another five for PLA+.

In order to manufacture ABS models, the stl file was sent to the Robox® Dual printer AutoMaker® software. Parameters used to 3D print ABS (CEL-Robox 2022) and PLA+ (Ultimaker 2022) specimens are shown in Table 6.1.

The Robox® Dual contains heated printing base, which ensures better material adhesion, and has a controlled printing environment. These two features help to avoid printing defects, as they keep the entire object warm until the end of the printing, causing it to cool down. Figure 6.1a, b shows the ABS and PLA+ specimens for the Tensile Test.

Table 6.1 Mean masses, standard deviation and variation coefficient

Parameters	ABS	PLA+
Infill	100%	100%
Colour	Orange	Black
Layer thickness	0.3 mm	0.2 mm
Extruder temperature	235 °C	215 °C
Room temperature	55 °C	~ 20 °C
Build base temperature	115 °C	~ 20 °C
Raster angle	+ 45°/− 45°	+ 45°/− 45°
Number of layers	11	15
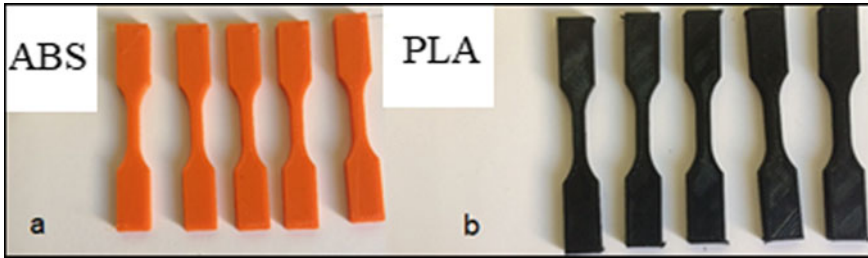
Fig. 6.1 Specimens of ABS **a** and PLA+ **b** for tensile test

The specimens were tested in a universal test machine, Shimadzu Autograph AGS-X 10 kN, with a constant de-formation velocity of 1 mm/min. The tensile test was performed until the specimen rupture.

6.2.2 Flexural Test

The specimens were manufactured with dimensions of 71.2 mm × 12.7 mm × 3.2 mm, taken from ASTM D790-17 standard (American Society for Testing and Materials 2017). Table 6.2 displays the data provided by the printer's software, except for fill percentage and filament colour parameters.

Figure 6.2b shows an ABS specimen in the machine at the beginning of the test, and Fig. 6.2a shows the ABS and PLA+ specimens after the test.

For the flexural tests, the specimens were positioned on the supports of the Shimadzu Universal Testing machine, Autograph AGS—X series (500 N to 10 kN) with its longest axis perpendicular to the load applicator. The test ended when a maximum strain of 0.05 mm/mm was reached, before breaking.

Table 6.2 Manufacturing parameters of ABS and PLA+ models

Parameters	ABS	PLA+
Infill	100%	100%
Colour	Orange	Black
Layer thickness	0.3 mm	0.2 mm
Extruder temperature	235 °C	215 °C
Room temperature	60 °C	~ 20 °C
Build base temperature	125 °C	~ 20 °C
Raster angle	+ 45°/− 45°	+ 45°/− 45°
Number of layers	11	15
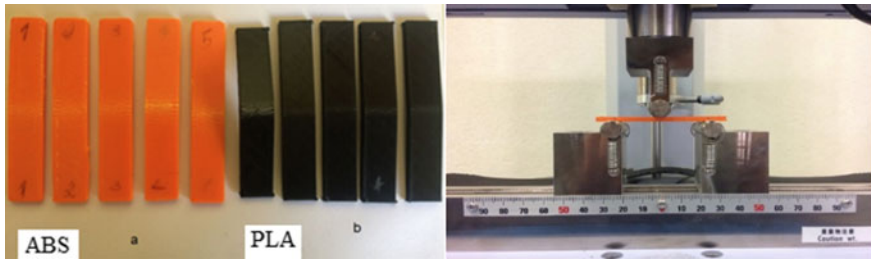
Fig. 6.2 Flexural specimens and three points flexural test

6.2.3 Water Absorption Test

According to D570-98 (ASTM D570-98 2010), the profile of the specimens follows the ISO standard, and their dimensions are 60 × 60 × 1 mm with tolerances of ± 2 and 0.05 mm, respectively.

Table 6.3 shows the printing parameters for PLA and ABS models manufactured by the Robox® Dual printer, together with parameters for PLA+ manufactured by the Big Builder® Dual Feed.

Figure 6.3a, b shows the specimens used in the water absorption test: ABS, PLA+ (black) and PLA, respectively.

Table 6.3 Printing parameters of PLA and PLA+ specimens for Water Absorption test

Parameters	PLA	PLA+	ABS
Infill	100%	100%	100%
Colour	Blue	Black	Orange
Layer thickness	0.3 mm	0.2 mm	0.3 mm
Extruder temperature	195 °C	210 °C	235 °C
Room temperature	70 °C	~ 20 °C	125 °C
Build base temperature	35 °C	~ 20 °C	60 °C
Raster angle	+ 45°/− 45°	+ 45°/− 45°	+ 45°/− 45°
Number of layers	3	5	3
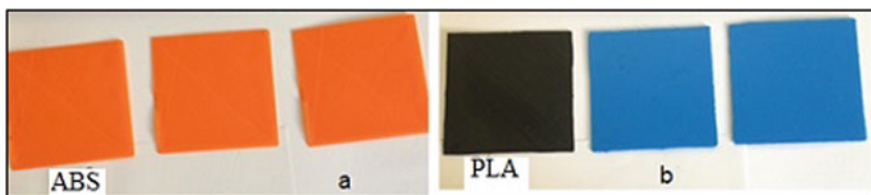
Fig. 6.3 Specimens in ABS (**a**), PLA+ and PLA for water absorption test (**b**)

It was chosen a 24-h immersion, with all specimens fully immersed in a container with distilled water in a vertical position, in order to have the largest possible surface in contact with water. After 24 h, the specimens were removed from water, one at a time, and then, their surface was dried with absorbent paper and immediately measured with a calliper and weighed on a scale.

6.3 Results and Discussion

6.3.1 Tensile Test

The stress–strain curves obtained from the tensile tests for the ABS material and PLA+ are represented in Figs. 6.4 and 6.5, respectively. It is possible to observe that the five specimens of each material present a very similar behaviour until the yield stress. The maximum plastic strain, in the case of ABS samples, varies a lot until failure, with failure observed for a minimum around 4.0% and a maximum of more than 6.6%. In the case of PLA+ samples, there was also a large variation, between 5.7% and 7.6%, although the stress has dropped more progressively than ABS.

Figure 6.6 presents average values of stress obtained from the experimental tests together with values obtained from literature, for comparison. ABS values were taken from (Kanu et al. 2016; Banjanin et al. 2018; Novakova-Marcincinova and Novak-Marcincin 2014; Letcher et al. 2015; Lovo and Fortulan 2016; Tymrak et al. 2014; Wu et al. 2015; Hibbert et al. 2019) and PLA+ from Banjanin et al. 2018; Lovo and Fortulan 2016; Tymrak et al. 2014; Santana et al. 2018).
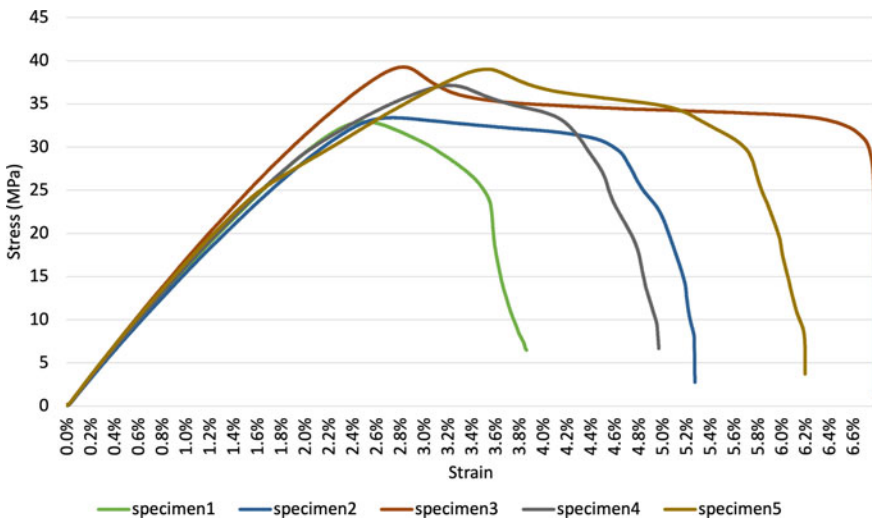
Fig. 6.4 Stress × Strain curves of the tensile test of ABS samples
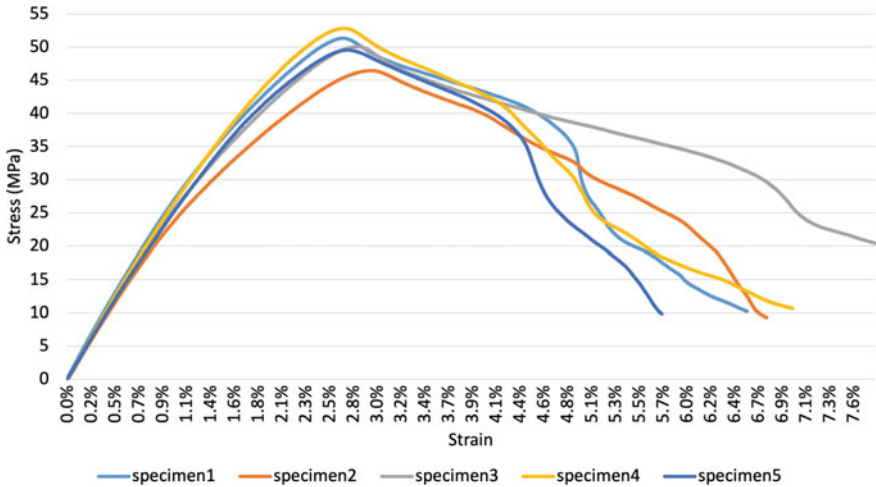
Fig. 6.5 Stress × Strain curves of the tensile test of PLA+ samples
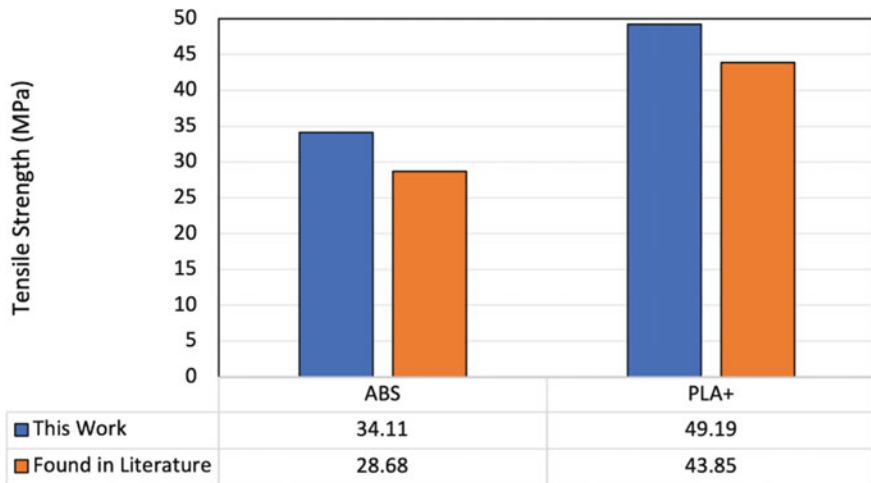
Fig. 6.6 Tensile strength values of samples in ABS and PLA+

The values obtained for ABS and PLA+ were a little higher than averages taken from literature, and this is due to several parameters that influence the results, such as different print settings, controlled environment inside the printer, layer and pigment orientations.

6.3.2 Flexural Test

The tests were carried out and the stress x strain curves of the samples were obtained, shown in Figs. 6.7 and 6.8. These figures present the graph with the stress values of the test specimens. The tests were interrupted until a strain value of, approximately, 5%. It can be observed that the samples had a very similar behaviour. For ABS, a maximum of 55 MPa was observed and for PLA+ a maximum of 85 MPa. Figure 6.8 shows a discontinuity in the graph which can be explained due to existing defects in the plastic filament.

Figure 6.9 shows the mean values of the bending stresses obtained from experimental tests in comparison to the literature, for ABS specimens (Wu et al. 2015;
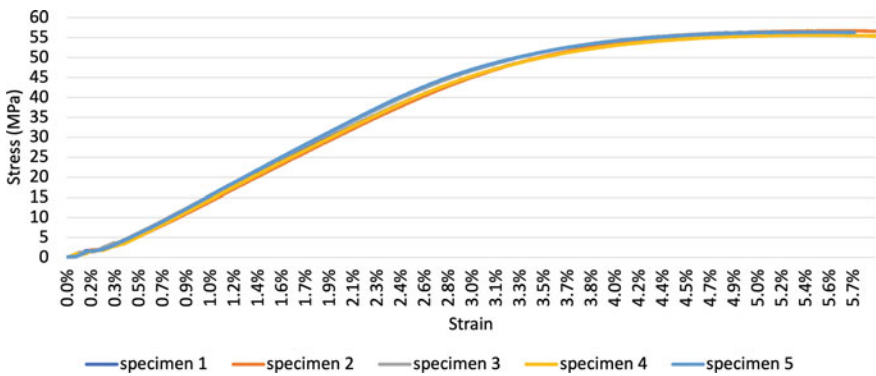
Fig. 6.7 Stress x Strain curves of the bending test of the ABS samples
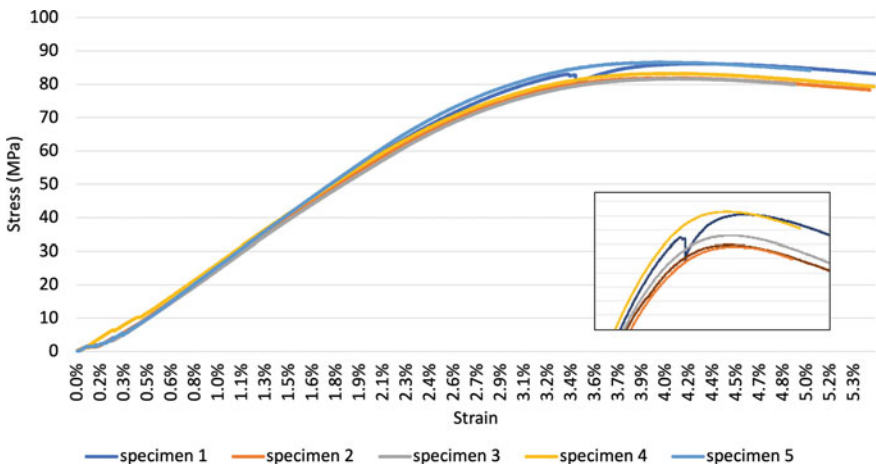
Fig. 6.8 Stress x Strain curves of the bending test of the PLA+ samples
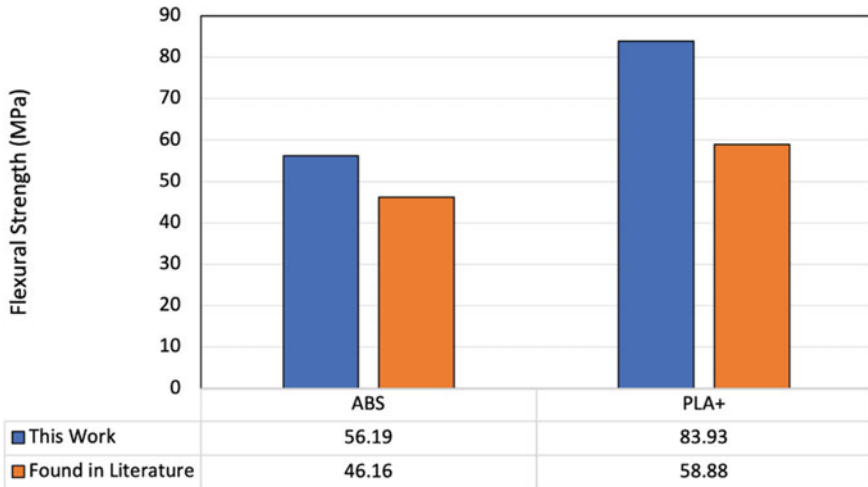
Fig. 6.9 Flexural strength values of samples in ABS and PLA+

Es-Said et al. 2000; Durgun and Ertan 2014; Dawoud et al. 2016) and PLA+ specimens (Rajpurohit and Dave 2018; Jaya Christiyan et al. 2018; Nugroho et al. 2018; Chacón et al. 2017).

The higher values obtained may be caused by the good adhesion between layers. They have small thicknesses (Jaya Christiyan et al. 2018) and raster angles (45°/−45°) (Ultimaker. 2022) that facilitate an increase in strength.

6.3.3 Water Absorption Test

The absorption of water in objects built using FDM printing is essentially due to gaps between layers and printing flaws. In addition, the more porous they are, the more water absorption is expected. ABS was the material with higher amount of water absorbed.

In this work, it was found that the smallest thickness presented the smallest water absorption (PLA+ thickness 0.2 mm), followed by PLA (0.3 mm thickness) and ABS (0.3 mm thickness).

Analysing Fig. 6.10, it can be concluded that ABS has the highest porosity values and was also the material that presented the highest weight percentage increase. A higher number of voids between the layers (porosities) end up influencing the mechanical strength of the material, decreasing it.
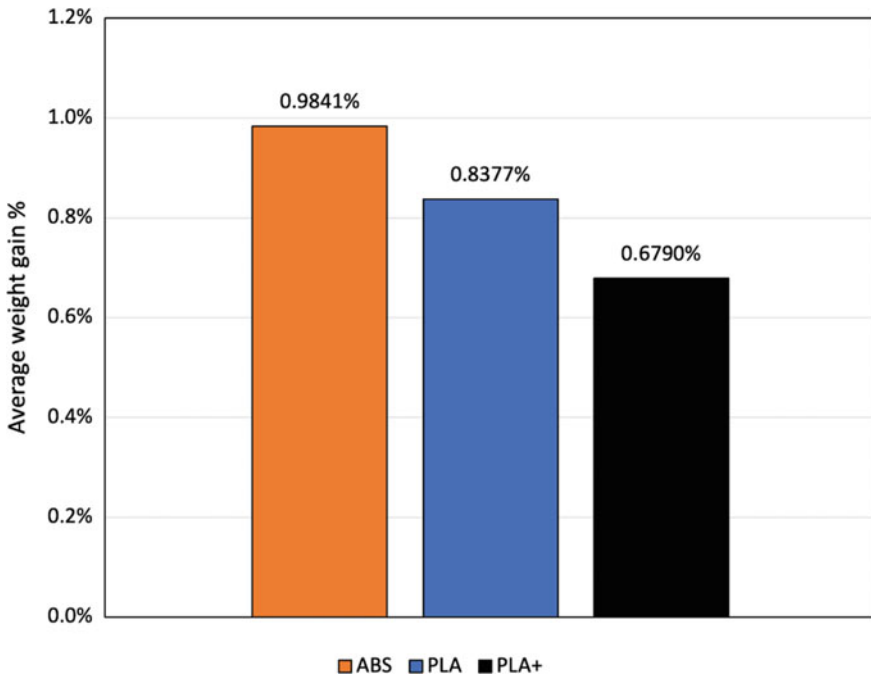
Fig. 6.10 Average percentage increase in sample weight

6.4 Conclusions

In this work, three different types of experimental tests were performed in order to determine the mechanical and physical properties of the most common thermoplastic filament used in FDM, namely ABS and PLA. Furthermore, it was analysed a special kind of PLA designated by PLA+, and the tensile strength of PLA+ (49 MPa) is higher than ABS (39 MPa). The values obtained with experimental tensile tests were higher than the observed from specialized literature. From the flexural tests, it was determined the flexural strength, results showed higher value for PLA+ (85 MPa) and lower for ABS (57 MPa) and these values are higher when compared with the ones showed in literature. In the water absorption test, it was observed that ABS (0.984%) had more water than the PLA (0.838%) and PLA+ (0.679%).

References

Algarni M, Ghazali S (2021) Comparative study of the sensitivity of PLA, ABS, PEEK, and PETG'S mechanical properties to FDM printing process parameters. Crystals (Basel) 11(8)

American Society for Testing and Materials (2017) ASTM D790-17—Standard test methods for flexural proper-ties of unreinforced and reinforced plastics and electrical insulating materials. Annual Book of ASTM Standards

ASTM (2020) ASTM D883: standard terminology relating to plastics. ASTM Standards

ASTM D570-98 (2010) D 570–98 Standard test method for water absorption of plastics ASTM D570-98. ASTM Standards. 98 (Reapproved 2010)

ASTM International (2014) ASTM D638-14. Annual Book of ASTM Standards

Banjanin B, Vladić G, Pál M, Baloš S, Dramićanin M, Rackov M, et al (2018) Consistency analysis of mechanical properties of elements produced by FDM additive manufacturing technology. Revista Materia 23(4)

Bhargav A, Sanjairaj V, Rosa V, Feng LW, Fuh YH J (2018) Applications of additive manufacturing in dentistry: a review. J Biomed Mater Res Part B Appl Biomater 106

Bird DT, Ravindra NM (2021) Additive manufacturing of sensors for military monitoring applications. Polym (Basel) 13(9)

Blakey-Milner B, Gradl P, Snedden G, Brooks M, Pitot J, Lopez E et al (2021) Metal additive manufacturing in aerospace: a review. Mater Des 209:110008 (Internet). Available from: https://www.sciencedirect.com/science/article/pii/S0264127521005633

CEL-Robox (2022) Product datasheet ABS CEL-Robox 1.75 mm Orange ABS 3D Printer Filament, 600g (Internet). RS. 2022 [cited 2022 Jun 22]. Available from: https://export.rsdelivers.com/product/cel/rbx-abs-or023/cel-robox-175mm-orange-abs-3d-printer-filament/9031359

Chacón JM, Caminero MA, García-Plaza E, Núñez PJ (2017) Additive manufacturing of PLA structures using fused deposition modelling: Effect of process parameters on mechanical properties and their optimal selection. Mater Des 124

Chapiro M (2016) Current achievements and future outlook for composites in 3D printing. Reinf Plast 60(6)

Charalampous P, Kostavelis I, Kontodina T, Tzovaras D (2021) Learning-based error modeling in FDM 3D printing process. Rapid Prototyping J 27(3)

Crump SS (1991) Fast, precise, safe prototypes with FDM. In: American society of mechanical engineers, production engineering division (Publication) PED

Dawoud M, Taha I, Ebeid SJ (2016) Mechanical behaviour of ABS: AN experimental study using FDM and injection moulding techniques. J Manuf Process 21

Dizon JRC, Espera AH, Chen Q, Advincula RC (2018) Mechanical characterization of 3D-printed polymers. Add Manuf 20

Durgun I, Ertan R (2014) Experimental investigation of FDM process for improvement of mechanical properties and production cost. Rapid Prototyping J 20(3)

Es-Said OS, Foyos J, Noorani R, Mendelson M, Marloth R, Pregger BA (2000) Effect of layer orientation on mechanical properties of rapid prototyped samples. Mater Manuf Process 15(1)

Gao W, Zhang Y, Ramanujan D, Ramani K, Chen Y, Williams CB et al (2015) The status, challenges, and future of additive manufacturing in engineering. CAD Comput Aided Des 69

Goh GD, Agarwala S, Goh GL, Dikshit V, Sing SL, Yeong WY (2017) Additive manufacturing in unmanned aerial vehicles (UAVs): challenges and potential. Aerosp Sci Technol 63

Hashemi Sanatgar R, Campagne C, Nierstrasz V (2017) Investigation of the adhesion properties of direct 3D printing of polymers and nanocomposites on textiles: effect of FDM printing process parameters. Appl Surf Sci 403:551–563 (Internet). Available from: https://www.sciencedirect.com/science/article/pii/S0169433217301137

Hibbert K, Warner G, Brown C, Ajide O, Owolabi G, Azimi A (2019) The effects of build parameters and strain rate on the mechanical properties of FDM 3D-Printed acrylonitrile butadiene styrene. Open J Org Polym Mater 09(01)

Hoskins TJ, Dearn KD, Kukureka SN (2018) Mechanical performance of PEEK produced by additive manufacturing. Polym Test 70

Jaya Christiyan KG, Chandrasekhar U, Venkateswarlu K (2018) Flexural properties of PLA components under various test condition manufactured by 3D printer. J Inst Eng (India): Ser C 99(3)

Kanu RC, Hale C, Piper PON (2016) The use of 3D printing to introduce students to ASTM standards for testing tensile properties of acrylonitrile-butadiene-styrene (ABS) plastic material. In: ASEE annual conference and exposition, conference proceedings

Lee JY, An J, Chua CK (2017) Fundamentals and applications of 3D printing for novel materials. Appl Mater Today 7

Letcher T, Rankouhi B, Javadpour S (2015) Experimental study of mechanical properties of additively manufactured abs plastic as a function of layer parameters. In: ASME international mechanical engineering congress and exposition, proceedings (IMECE)

Lovo JFP, Fortulan CA (2016) Estudo de propriedades mecânicas e anisotropia em peças fabricadas por manufatura aditiva tipo FDM. I Simpósio do Programa de Pós-Graduação em Engenharia Mecânica da EESC-USP (SiPGEM/EESC-USP) (1)

MacDonald E, Salas R, Espalin D, Perez M, Aguilera E, Muse D et al (2014) 3D printing for the rapid prototyping of structural electronics. IEEE Access 2

Novakova-Marcincinova L, Novak-Marcincin J (2014) Testing of ABS material tensile strength for fused deposition modeling rapid prototyping meth-od. Adv Mater Res

Nugroho A, Ardiansyah R, Rusita L, Larasati IL (2008) Effect of layer thick-ness on flexural properties of PLA (PolyLactid Acid) by 3D printing. J Phys Conf Ser

Paolini A, Kollmannsberger S, Rank E (2019) Additive manufacturing in construction: a review on processes, applications, and digital planning methods. Add Manuf 30:100894 (Internet). Available from: https://www.sciencedirect.com/science/article/pii/S2214860419309029

Rajpurohit SR, Dave HK (2018) Flexural strength of fused filament fabricated (FFF) PLA parts on an open-source 3D printer. Adv Manuf 6(4)

Santana L, Alves J, Netto A, Merlini C (2018) Estudo comparativo entre PETG e PLA para Impressão 3D através de caracterização térmica, química e mecânica. Matéria (rio De Janeiro). 6:23

Souza A, Souza MS, Pinho D, Agujetas R, Ferrera C, Lima R, et al (2020) 3D manufacturing of intracranial aneurysm biomodels for flow visualizations: low cost fabrication processes. Mech Res Commun 107:103535 (Internet). Available from: https://www.sciencedirect.com/science/article/pii/S0093641320300641

Tymrak BM, Kreiger M, Pearce JM (2014) Mechanical properties of components fabricated with open-source 3-D printers under realistic environ-mental conditions. Mater Des 58

Ultimaker (2022) Technical data sheet tough PLA (Internet). 2022 (cited 2022 Jun 22). Available from: https://docs.rs-online.com/d6e4/0900766b81697f3b.pdf

Vaezi M, Seitz H, Yang S (2013) A review on 3D micro-additive manufacturing technologies. Int J Adv Manuf Technol 67(5–8):1721–1754 (Erratum). https://doi.org/10.1007/s00170-012-4605-2

Wu W, Geng P, Li G, Zhao D, Zhang H, Zhao JI (2015) Influence of layer thickness and raster angle on the mechanical properties of 3D-Printed PEEK and a comparative mechanical study between PEEK and ABS. Materials 8:5834–5846

Chapter 7
Potential Use of Sugarcane Bagasse Ash in Cementitious Mortars for 3D Printing

M. Jesus, J. Teixeira, J. L. Alves, S. Pessoa, A. S. Guimarães, and B. Rangel

Abstract Mortars, in particular 3D printing (3DP) ones, rely heavily on Portland cement (PC), a material that entails high carbon emissions and energy consumption related to its manufacture. As its use must become more moderate to comply with the growing environmental regulations and concerns, alternatives to PC or additives to reduce its percentage are being sought. Due to providing adequate pozzolanic activity and filler effect, many supplementary cementitious materials (SCM) have been used, such as agricultural waste. Sugarcane bagasse ash (SCBA) emerges as a strong contender, since sugarcane is available in rich quantities in Brazil and India, with almost no land left to dispose the raw bagasse. The aim of this research is to present a mixture for 3DP with a suitable SCBA content that conforms with the properties in the fresh (flow table and slump) and hardened states (compressive and flexural strength). SCBA with a particle size up to 250 µm was used to replace PC with different dosages (5, 10, 15, 20, 25%), by volume of binder. The fine aggregates used (two types of sand) were kept constant, according to the reference mixture, and no plasticizers or superplasticizers were incorporated. Experimental results showed that an increase in SCBA caused an increase in the water content and the mixture with 5% of SCBA showed similar results of mechanical strength at 28 days when compared to the reference mixture.

Keywords 3D printing mortars · Mix design · Fresh and hardened properties · Sugarcane bagasse ash · Sustainability

M. Jesus (✉) · J. Teixeira · S. Pessoa · A. S. Guimarães · B. Rangel
Faculty of Engineering (FEUP), CONSTRUCT, University of Porto, Rua Dr. Roberto Frias s/n, 4200-465 Porto, Portugal
e-mail: up201505444@edu.fe.up.pt

J. L. Alves
INEGI/Faculty of Engineering (FEUP), University of Porto, Rua Dr. Roberto Frias s/n, 4200-465 Porto, Portugal

7.1 Introduction

The building and construction sector is known for its outdated methods and low productivity, making use of poorly innovative techniques that not only consume large quantities of resources and generate significant amounts of waste, but also bring considerable risks to the manpower. The current implementation of new technologies in this industry (e.g. building information modelling (BIM) and 3DP) proved to bring production and automation benefits while aiming to improve its sustainability, due to: architectural freedom; reduction of material consumption, waste and CO_2 emissions; continuous printing capacity; mitigation of normal constraints during construction (smoke, dust and excessive noise); capacity of constructing in harsh environments, where manpower is unsuitable (Yossef and Chen 2015; Lopes 2016; Wolfs and Salet 2016).

Regarding the materials for 3DP, as the already conceived mixtures contain high amounts of cement (Bos et al. 2016), SCMs are being tested (mainly fly ash (FA) and silica fume (SF)), to reduce high carbon emissions and energy consumption related to the manufacture of cement. Besides contributing to more sustainable mixtures, the integration of these additives is also performed to improve the rheology of mortars and to achieve a proper buildability, for example (Muthukrishnan et al. 2020; Khalil et al. 2020). Muthukrishnan et al. (2020) used rice husk ash as a cement replacement in 3DP mortars, obtaining compressive strength values 180–500% higher than the conventional mortar and reaching the desired workability faster. Khalil et al. (2020) proposed a 3DP mixture of magnesium oxide concrete that showed excellent extrudability, flowability and buildability. The printed specimens also presented a greater compressive strength than cast ones.

This article seeks to study and summarize the different compositions, dosages and materials used in the currently conceived mixtures for 3DP, as well as the inherent requirements for a successful printable material. To contribute to a more sustainable mixture, SCBA, a residue obtained from the incineration of sugarcane bagasse, was added to the composition as a SCM, with substitution rates of 5–25%. Several mortars were then prepared, varying the amount of water according to their percentages of SCBA. It is important to mention that no plasticizer or superplasticizer was used in order to clearly evaluate the influence of the residue.

All mortars were subjected to flow table and slump tests to assess each ones' flowability and buildability/shape retention, respectively. After that, some specimens of the produced mortars were moulded to evaluate their mechanical resistance, namely compressive and flexural strength at 7 and 28 days. It was also possible to print one of the studied compositions.

7.2 Literature Review

One of the most used materials for both in situ structures as well as prefabricated ones (off-site) is concrete. In fact, it provides most of the necessary features for construction purposes: good compressive strength, fire resistance, a good moldability and durability, all under a relatively low production cost (Bos et al. 2016). Thus, 3DP mortar compositions are based on the one of concrete, without the use of coarse aggregates, so as not to affect 3D printer elements, as will be explained.

A primary literature review was essential to record several compositions and respective dosages of different 3D printable cementitious mortars developed worldwide. Once collected, an average was calculated, as shown in Fig. 7.1.

Additions include SF, FA and limestone filler (LF), often used within the study of 3D printable cementitious mortars to reduce the amount of cement. Superplasticizers, retarders and accelerators are also present in some mixtures (Khoshnevis 2005; Nerella et al. 2016; Kruger et al. 2019; Kazemian et al. 2017; Schröfl et al. 2018; Paul et al. 2018) but since they comprise a very small percentage (normally 1–2%), they were not considered in this experimental programme.

In the case of SCBA, many researchers have been studying its potential to replace cement in mortars and concrete. Ganesan et al. (2007) explored the effects of SCBA as a partial replacement of cement, concluding that with an optimum replacement of 20% of cement, there was a development of high early strength, a reduction in
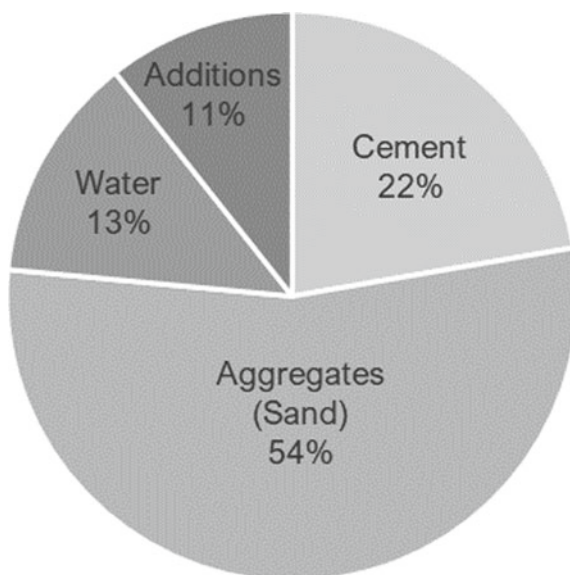
Fig. 7.1 Average dosages of 3D printing cementitious mortars (values from Khoshnevis (2005), Tay et al. (2016), Nerella et al. (2016), Teixeira et al. (2021), Kruger et al. (2019), Kazemian et al. (2017), Schröfl et al. (2018), Lafhaj et al. (2019), Ting et al. (2019) and Paul et al. (2018))

Table 7.1 Influence of the SCBA in the amount of water in cast cementitious mixtures

SCBA (%)	W/C* or W/(C + BA**)				
0	0.53	0.57	0.55	0.60	0.50
5		0.61	–	–	0.52
10		0.62	0.50	0.60	0.54
15		0.64	–	–	0.57
20		0.67	0.44	0.60	0.60
Mixture	Hardened concrete	Sustainable concrete	Mortar	Mortar	Mortar
References	Ganesan et al. (2007)	Quedou et al. (2021)	Chi (2012)	Arenas-Piedrahita et al. (2016)	Arif et al. (2016)

*W/C—Water/cement ratio
**BA—Bagasse ash

water permeability and a significant resistance to chloride permeation and diffusion. Quedou et al. (2021) and Chi (2012) concluded that a 10% replacement of cement with SCBA was the optimal limit, since it had a superior performance on compressive strength, drying shrinkage, water absorption, initial surface absorption and chloride ion penetration (56 days), while contributing to the preservation of the environment.

To understand how the SCBA is used, several cementitious mixtures with SCBA in different ratios were grouped in Table 7.1.

Although Table 7.1 refers to cast/moulded specimens, the respective data allowed to identify important insights for the composition of the first mortars with SCBA:

- The W/C ratio varies between 0.50 and 0.60, being higher as the percentage of ash increases, suggesting that it has a high-water absorption. This may be justified by its lightness (Otoko 2014) or by its hygroscopic properties (Ganesan et al. 2007);
- The percentage of SCBA used is relatively constant between the different mixtures presented (5–20%), assuming that, for these values, the printed material kept or improved most of its relevant properties.

When designing a 3DP mortar, there should be an evolution in workability: at first, a very workable material is required, to be smoothly transported from the mixer to the extrusion nozzle, but after the extrusion process, it should stiff quickly, to guarantee a continuous spread of filaments of material capable of sustaining subsequent layers without deformations, which implies a loss of workability (Teixeira et al. 2021; Ma et al. 2017, 2018). The following properties strongly influence workability (Ma et al. 2017, 2018; Lim et al. 2012):

- Flowability/Pumpability—Capacity of the mortar to be smoothly transported from the mixer to the extrusion nozzle, being affected by temperature and relative humidity. It is directly related to workability;
- Extrudability—Ability of the mixture to continuously pass through the extrusion nozzle, without blocking the system, while producing uniform filaments;
- Buildability—Extrusion of filaments into stacked layers;

- Shape retention—Capacity of the material to retain its extruded shape and resistance at early ages, under self-weight and the pressure of subsequent layers;
- Open time—Time interval where the fresh mortar is capable of being continuously extruded, in stacked layers and without blocking the system. It is related to the change of flowability over time;
- Printability—Ability of the mixture to be printed in the desired geometry, maintaining dimensional stability and good surface finish, being influenced by the above-mentioned properties.

In addition, attention should be paid to other factors related to the compatibility of the mortar and the printing equipment: printing system size, mixing procedure, flow rate, pump pressure, type of extruder and shape and size of the nozzle (Bos et al. 2016; Ma et al. 2018; Malaeb et al. 2019; Rushing et al. 2019).

An optimal mixture for extrusion is hard to reach, as will be understood later, since it requires several steps and always depends on the differences between the type of 3D printers, the nature of the constituents, the surrounding conditions and the research purpose (Ma et al. 2018).

7.3 Laboratory Tests for SCBA Characterization

7.3.1 Bulk Density

The bulk density, ρ, represents the mass of a material divided by its total volume and depends on the percentage of existing voids. Before setting up any mixture, it is necessary to collect the bulk densities of all the components to estimate their quantities. The bulk density of each material had already been calculated for a previous study (Teixeira et al. 2021), except for the SCBA. It was determined through the pycnometer method (Fig. 7.2), as described in NP EN 1097-7:2012 (2012). The results are given in Table 7.2.

As expected, SCBA presents a low bulk density when compared to the other constituents.

7.3.2 Particle Size Distribution

Since the activity of SCBA highly depends on its particle size and fineness, the particle size distribution of the material was determined through the sieving method, as suggested by NP EN 933-1:2014 (2014). This test enables a significant understanding of the effectiveness of a certain material, since some of its properties (bulk density, permeability, etc.) are controlled by the size of the material's particles. With the results obtained, it was possible to plot the granulometric curve shown in Fig. 7.3.

Fig. 7.2 Determination of SCBA's bulk density with pycnometers

Table 7.2 Bulk density of each constituent

Constituent	PC	SCBA	LF	Sand 0–4 mm	Sand 0–2 mm
Bulk density (kg/m^3)	3100	2330	2700	2637	2636
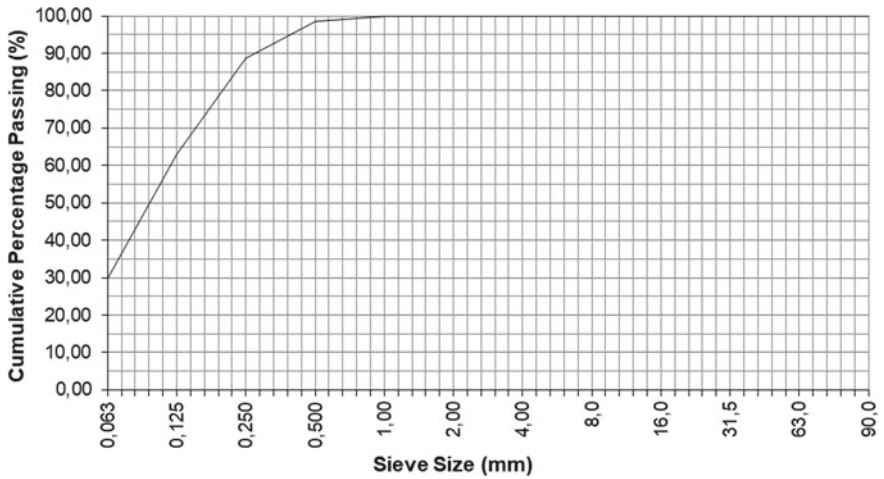
Fig. 7.3 Granulometric curve of SCBA

After analysing the curve presented above, it is possible to conclude that almost all the material passed the 0.500 mm sieve. However, only 30% of the sample passed in the 0.063 mm sieve, which means that a very small percentage of it has a cement-like fineness (the size of cement's particles is usually < 0.1 mm). In order to avoid great losses of material (in the order of 70%), the material that was used was the one that passed in the 0.250 mm sieve, allowing the removal of coarse material.

7.4 Cementitious Mortar Design

7.4.1 Materials Used

SCBA was collected from different waste disposals in Brazil. It results from the incineration of sugarcane bagasse, a fibrous matter obtained from the extraction of sugarcane juice. It is composed by fine burnt and coarse unburnt particles, being deposited in the cogeneration plant (Bahurudeen et al. 2015) and then it can be used as a soil fertilizer or filling material, but most of the times, it is dumped in ash ponds or landfills (Quedou et al. 2021; Jagadesh et al. 2019). Since it is a waste material with unknown properties, it was crucial to conduct the tests described in Sect. 7.3.

PC (CEM I 42.5 R) was used for the trials, according to EN 197-1:2011 (2011).

As natural fine aggregates, two sands with different granulometries were used: 0–2 mm and 0–4 mm. According to Teixeira et al. (2021), the nozzle diameter may be up to five times larger than the maximum aggregate size. Since the circular nozzle used has a diameter close to 20 mm, it was possible to use sand with a particle size up to 4 mm.

Since LF enables a better particle size distribution, by filling the voids in the mixture, and improves its mechanical strength, a small portion was also considered in the composition of the mortars.

Also, tap water was used.

7.4.2 Dosage Calculation

Since the purpose of this work is to study the effect of SCBA on the composition of 3D printable mortars, small increments of this residue were tested (5, 10, 15, 20 and 25%), allowing a reduction in the amount of cement used.

The mixture proportions followed, in part, the experimental work proposed by Teixeira et al. (2021), calculated for an approximate volume of 1 L, and they are given in Table 7.3.

The percentage of replacement of cement per SCBA is related to its volume, not to its mass. For instance, if the volume of cement is 9% for 0% of SCBA, the used

Table 7.3 Mixture proportions of cementitious and SCBA mortars, per mass

Mixture reference	% of substitution (volume)	PC (%)	LF (%)	SCBA (%)	Water (%)	Sand 0–2 mm (%)	Sand 0–4 mm (%)	W/C	W/P*
SCBA-0	0	13.50	11.80	0.00	10.70	6.40	57.60	0.79	0.42
SCBA-5	5	12.90	11.80	0.50	10.70	6.40	57.70	0.83	0.42
SCBA-10	10	12.20	11.80	1.00	11.10	6.40	57.60	0.91	0.44
SCBA-15	15	11.50	11.80	1.50	11.40	6.40	57.40	1.00	0.46
SCBA-20	20	10.80	11.70	2.00	11.80	6.40	57.30	1.10	0.48
SCBA-25	25	10.10	11.70	2.50	12.10	6.40	57.20	1.20	0.50

*W/P—Water/powders ratio (powders include PC, LF and SCBA)

Table 7.4 Comparison between the average values of the mixtures from literature and experimental work

Source	Cement (%)	Additions (%)	Water (%)	Sand (%)
Average values from literature (Fig. 7.1)	22	11	13	54
Average values from experimental work (Table 7.3)	13	13	11	64

*Additions include SF and FA (literature dosages), SCBA and LF (Table 7.3)

volume of SCBA for a 10% replacement will be 0.9%, so the correspondent volume of cement for this new mixture will be 8.1%.

The mixture dosages were controlled by W/P, since it has significant influence on the fresh properties of the mortars (Teixeira et al. 2022), while W/C affects their mechanical resistance (Panda et al. 2020). The proportions of the other constituents were not modified throughout the mixtures, apart from water, which was adjusted upwards whenever the percentage of SCBA increased.

The average values of the designed mixtures were compared with the average literature values presented in Fig. 7.1. The results can be seen in Table 7.4.

The mixtures prepared during the experimental work slightly differ from the ones proposed by the other authors. The greatest variation found in the dosages was related to the percentage of cement used. Its reduction is mainly linked to the high quantity of aggregate (sand) applied, which leads to a lower need to fill the voids between the particles with paste (composed by water and powders) (Teixeira et al. 2021), despite reducing the mechanical resistance.

7.5 Laboratory Tests for Mortar Characterization

7.5.1 Consistency of Fresh Mortar

After estimating the dosages, the mixtures were then prepared, being possible to observe if it was necessary to add more water or other materials to the mixture, through its viscosity (Fig. 7.4b) and according to the intended purpose of the mortars (in this case, for 3DP).

The determination of the mortars' consistency in fresh state, by the flow table method, was based on EN 1015-3:1999 (1999). Firstly, a mould is filled with two layers of mortar, that are compacted through ten short strokes with a tamper. After that, the mould is removed and the slump, defined as the displacement suffered by the mortar when the mould is removed, is measured, in mm (Fig. 7.5a). Then, the material is jolted 15 times on the flow table and the spread mortar diameter is measured in perpendicular directions (Fig. 7.5b). The average diameter (of those 2 values) represents the flow value, in mm. The flow values obtained for each mixture are displayed in Table 7.5.
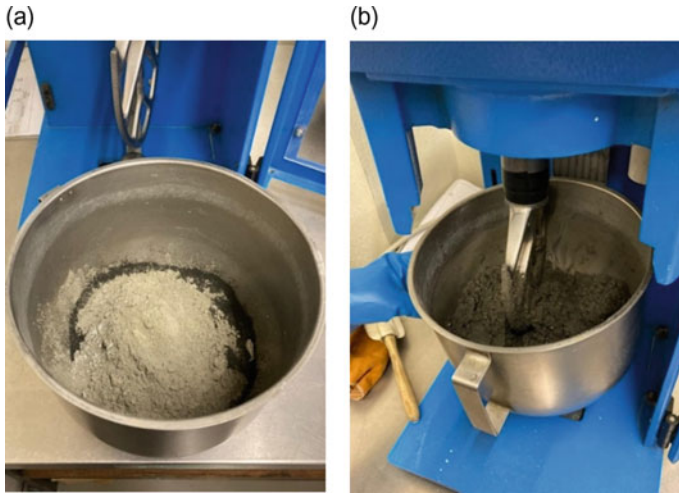
Fig. 7.4 **a** Placement of the constituents in the container and **b** constituent mixture
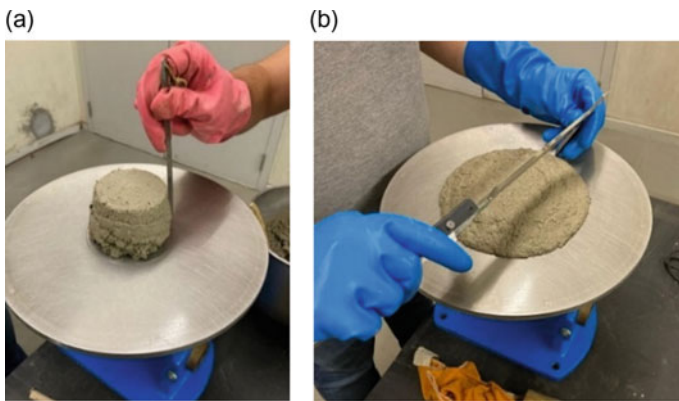
Fig. 7.5 **a** Evaluation of mortar's slump and **b** mortar's flow

Table 7.5 Flow table test results

Mixture reference	SCBA-0	SCBA-5	SCBA-10	SCBA-15	SCBA-20	SCBA-25
W/P	0.42	0.42	0.44	0.46	0.48	0.50
Flow (mm)	168.50	174.00	170.00	172.50	176.00	181.50

To obtain proper flow values (between 175 and 210 mm, to reach a suitable flowability of the mixture for 3DP (Ma et al. 2018)), W/P ratio should be close to 0.40, when no plasticizers/superplasticizers are added (Teixeira et al. 2022). However,

since the flow value of the reference mixture (0% SCBA) was 168.5 mm, the subsequent values of the other compositions should range between ± 10 mm from that reference value, according to NP EN 450-1:2012 (2012). As seen in Table 7.5, to obtain values within that interval, W/P was increased (more water added) whenever the percentage of SCBA was increased.

Regarding the slump test, all mixtures showed displacements close to zero, as intended, since after the extrusion, the material must guarantee good shape stability due to the lack of support formwork to sustain the weight of the upper layers (Long et al. 2019).

7.5.2 Mechanical Resistance

The mechanical resistance of cast specimens was assessed through compressive and flexural strength tests, performed in accordance with EN 196-1:2016 (2016). After the determination of the consistency, the fresh mortar was poured into a specific mould with 3 slots, so that 3 test specimens can be tested per mixture. The specimens were stored in the mould in a moist atmosphere for 24 h, then demoulded and stored under water until mechanical strength tests took place. At the required ages (normally 7 and 28 days), the specimens were subjected to flexure (Fig. 7.6a) and then each half was submitted to the compressive test (Fig. 7.6b). The results can be observed in Table 7.6.

A decrease in the mechanical resistance of mortars was expected, since SCBA does not provide a similar strength to cement. When analysing mechanical strength values, from mixture SCBA-0 to SCBA-25, an accentuated decrease is observed, due
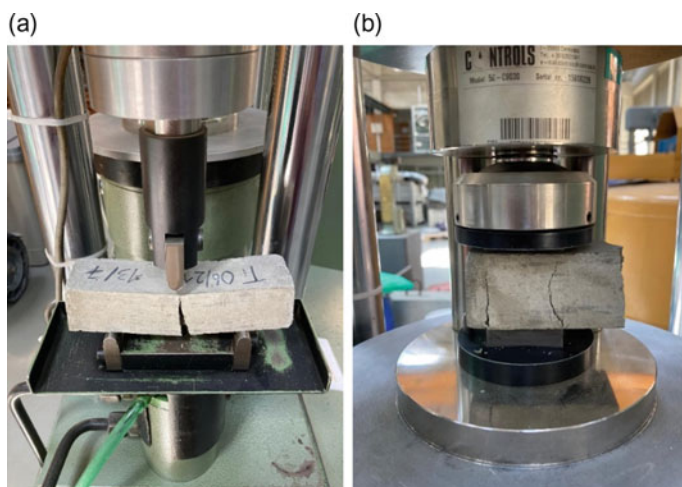
Fig. 7.6 a Flexural and **b** compressive strength tests

Table 7.6 Mechanical resistance of cast specimens

Mixture reference	Average flexural strength (MPa)		Average compressive strength (MPa)	
	7 days	28 days	7 days	28 days
SCBA-0	5.30	5.90	30.40	35.00
SCBA-5	4.60	5.80	27.50	33.20
SCBA-10	4.50	5.20	24.10	28.60
SCBA-15	3.90	4.80	18.90	23.70
SCBA-20	3.70	–	16.60	–
SCBA-25	3.00	–	14.20	–

to the combined action of cement reduction in favour of SCBA and the increase of water content (as reported in Table 7.3). It is also important to mention that when the specimens were being cast, mixtures SCBA-20 and SCBA-25 presented exudation, which can cause segregation when hardened.

7.6 Printing Trial

A first trial was carried out with mixture SCBA-15, in order to assess its printability. The printed specimen presents an average layer width of 35 mm and a layer thickness of approximately 15 mm.

As seen in Fig. 7.7, the prototype shows an adequate buildability and shape retention. The extrusion process occurred continuously, without any sort of clogging in the printing system, which means that the mixture had enough flowability to be extruded.

Fig. 7.7 Printing trial of the composition with 15% of SCBA

However, it is visible that the material is too dry, resulting in some voids and roughness in the sample surface. This problem may be related to the significant reduction in the amount of cement at the expense of SCBA, which can result in segregation. Thus, it can be concluded that the following mixtures to be tested will be those of 5 and 10% of SCBA.

7.7 Conclusions

As previously mentioned, the study of SCM is not new within the design of new 3DP cementitious mortars, mainly with SF and FA. However, despite using those constituents to improve important properties of the mixtures, the compositions found in the literature maintain their rations of PC. Instead, this study sought to evaluate the effects of a further reduction in the amount of cement employed in new 3DP cementitious mixtures, which is already low due to the significant quantity of sand and LF used.

Regarding the experimental tests, an increase in the amount of SCBA led to a higher W/P ratio, since it requires a greater amount of water to maintain the desired levels of fluidity and slump, decreasing the mortars' mechanical resistance. This fact is probably related to the fine structure and lightness of the residue employed. According to the literature, to reverse this pattern, chemical admixtures (such as superplasticizers) should be used to lower the W/P ratio. The slump test showed that values near to zero were ideal to produce a 3DP mortar with acceptable build-ability and shape retention. Furthermore, the mechanical resistance of the specimens decreased with higher amounts of SCBA and water (a lower W/C ratio).

The printing trial demonstrated that a 15% substitution of cement by SCBA is not advisable, since the printed specimen entailed a considerable number of voids and roughness on the external surfaces. This problem can result later in segregation, affecting the material durability. Also, flow values close to 170 mm were ideal to achieve an adequate flowability.

Further work should contemplate the printing of mixtures SCBA-5 and SCBA-10, accounting the results from the printed specimen with 15% of SCBA. Also, the fresh and hardened state properties of the mortars would benefit from a combination of other SCM with SCBA, such as SF or FA, capable of improving its mechanical properties and reducing the absorption of large quantities of water associated with SCBA (the latter could be also fixed with a plasticizer/superplasticizer). In the end, it might be interesting to determine the mechanical resistance of the printed samples and compare it with the values obtained for the moulded ones (Table 7.6).

References

Arenas-Piedrahita JC, Montes-García P, Mendoza-Rangel JM, López Calvo HZ, Valdez-Tamez PL, Martínez-Reyes J (2016) Mechanical and durability properties of mortars prepared with untreated sugarcane bagasse ash and untreated fly ash. Constr Build Mater 105:69–81

Arif E, Clark MW, Lake N (2016) Sugarcane bagasse ash from a high efficiency co-generation boiler: applications in cement and mortar production. Constr Build Mater 128:287–297

Bahurudeen A, Kanraj D, Gokul Dev V, Santhanam M (2015) Performance evaluation of sugarcane bagasse ash blended cement in concrete. Cem Concr Compos 59:77–88

Bos F, Wolfs R, Ahmed Z, Salet T (2016) Additive manufacturing of concrete in construction: potentials and challenges of 3D concrete printing. Virtual Phys Prototyping 11(3):209–225

Cement—part 1: composition, specifications and conformity criteria for common cements (2011)

Chi M-C (2012) Effects of sugarcane bagasse ash as a cement replacement on properties of mortars. Sci Eng Compos Mater 19(3):279–285

Cinzas volantes para betão—Parte 1: Definição, espeficicações e critérios de conformidade (2012)

Ensaios das propriedades mecânicas e físicas dos agregados—Parte 7: Determinação da massa volúmica do fíler—Método do picnómetro (2012)

Ensaios das propriedades geométricas dos agregados—Parte 1: Análise granulométrica—Método da peneiração (2014)

Ganesan K, Rajagopal K, Thangavel K (2007) Evaluation of bagasse ash as supplementary cementitious material. Cement Concr Compos 29(6):515–524

Jagadesh P, Ramachandramurthy A, Murugesan R, Karthik Prabhu T (2019) Adaptability of sugar cane bagasse ash in mortar. J Inst Eng (India) Ser A 100(2):225–240

Kazemian A, Yuan X, Cochran E, Khoshnevis B (2017) Cementitious materials for construction-scale 3D printing: Laboratory testing of fresh printing mixture. Constr Build Mater 145:639–647

Khalil A, Wang X, Celik K (2020) 3D Printable magnesium oxide concrete: towards sustainable modern architecture. Addit Manuf 33:101145

Khoshnevis B (2005) An innovative construction process-contour crafting (CC). In: Presented at the proceedings of the 22nd international symposium on automation and robotics in construction, 11th–14th September 2005

Kruger J, Zeranka S, van Zijl G (2019) 3D concrete printing: a lower bound analytical model for buildability performance quantification. Autom Constr 106:102904

Lafhaj Z, Rabenantoandro AZ, el Moussaoui S, Dakhli Z, Youssef N (2019) Experimental approach for printability assessment: toward a practical decision-making framework of printability for cementitious materials. Buildings 9(12)

Lim S, Buswell RA, Le TT, Austin SA, Gibb AGF, Thorpe T (2012) Developments in construction-scale additive manufacturing processes. Autom Constr 21:262–268

Long W-J et al (2019) Rheology and buildability of sustainable cement-based composites containing micro-crystalline cellulose for 3D-printing. J Clean Prod 239:118054

Lopes GTF (2016) Exploração das Possibilidades da Impressão 3D na Construção, Master thesis, FEUP, Porto, Portugal

Ma G, Wang L, Ju Y (2017) State-of-the-art of 3D printing technology of cementitious material—an emerging technique for construction. Sci China Technol Sci 61(4):475–495

Ma G, Li Z, Wang L (2018) Printable properties of cementitious material containing copper tailings for extrusion based 3D printing. Constr Build Mater 162:613–627

Malaeb Z, AlSakka F, Hamzeh F (2019) Chapter 6—3D concrete printing: machine design, mix proportioning, and mix comparison between different machine setups. In: Sanjayan JG, Nazari A, Nematollahi B (eds) 3D concrete printing technology. Butterworth-Heinemann, pp 115–136

Methods of test for mortar for masonry—part 3: determination of consistence of fresh mortar (by flow table) (1999)

Methods of testing cement—part 1: determination of strength (2016)

Muthukrishnan S, Kua Harn W, Yu Ling N, Chung Jacky KH (2020) Fresh properties of cementitious materials containing rice husk ash for construction 3D printing. J Mater Civ Eng 32(8):04020195

Nerella VN, Krause M, Näther M, Mechtcherine V (2016) Studying printability of fresh concrete for formwork free concrete on-site 3D printing technology (CONPrint3D)

Otoko DG (2014) Use of bagasse ash as partial replacement of cement in concrete. Int J Innovative Res Dev 3:1–5

Panda S, Sarkar P, Davis R (2020) Effect of water-cement ratio on mix design and mechanical strength of copper slag aggregate concrete. IOP Conf Ser Mater Sci Eng 936(1):012019

Paul SC, Tay YWD, Panda B, Tan MJ (2018) Fresh and hardened properties of 3D printable cementitious materials for building and construction. Arch Civ Mech Eng 18(1):311–319

Quedou PG, Wirquin E, Bokhoree C (2021) Sustainable concrete: potency of sugarcane bagasse ash as a cementitious material in the construction industry. Case Stud Constr Mater 14:e00545

Rushing TS et al (2019) Chapter 7—Investigation of concrete mixtures for additive construction. In: Sanjayan JG, Nazari A, Nematollahi B (eds) 3D concrete printing technology. Butterworth-Heinemann, Victoria, Australia, pp 137–160

Schröfl C, Nerella VN, Mechtcherine V (2019) Capillary water intake by 3D-printed concrete visualised and quantified by neutron radiography. In: First RILEM international conference on concrete and digital fabrication—digital concrete 2018. Springer International Publishing, Cham, pp 217–224

Tay YWD et al (2016) Processing and properties of construction materials for 3D printing. Mater Sci Forum 861:177–181

Teixeira J et al (2021) Development of 3D printing sustainable mortars based on a bibliometric analysis. Proc Inst Mech Eng Part L J Mater Des Appl. https://doi.org/10.1177/1464420721995210

Teixeira J, Schaefer CO, Maia L, Rangel B, Neto R, Alves JL (2022) Influence of supplementary cementitious materials on fresh properties of 3D printable materials. Sustainability 14(7)

Ting GH, Tay YWD, Qian Y, Tan MJ (2019) Utilization of recycled glass for 3D concrete printing: rheological and mechanical properties. J Mater Cycles Waste Manage 21(4):994–1003

Wolfs RJM, Salet TAM (2016) Potentials and challenges in 3D concrete printing. In: 2nd International conference on progress in additive manufacturing Singapore, pp 8–13

Yossef M, Chen A (2015) Applicability and limitations of 3D printing for civil structures. In: Conference on autonomous and robotic construction of infrastructure. Ames, Iowa, United States of America, pp 237–246

Part IV
Design

Chapter 8
Experimental Bench for the Analysis of Belt Deformation in Belt–Pulley Systems by Digital Image Correlation

Francesco Bucchi, Francesco Frendo, and Paolo Neri

Abstract Belt–pulley transmissions are a classical topic in mechanical engineering, usually studied following two approaches: the *creep* theory (Euler or Grashof model) and the *shear* theory. Recently, the authors introduced a new theory to study the belt–pulley contact mechanics, which is inspired to the *brush* model used for pneumatic tires. Basing on this theory, the belt is considered as an almost axially rigid tension member connected to a series of bristles, which are, at the other end, in contact with the pulley. In this paper, a test bench is presented and designed to experimentally validate the brush model. The bench is made up of two pulleys connected to two shafts driven by independently controlled motors; a belt is installed between the pulleys, and the shafts are equipped with sensors measuring the angular velocity and the transmitted torque. The belt preload, which is measured by a load cell, can be varied by changing the distance between the two shafts. The belt was painted creating a suitable texture (random speckle pattern) to be interpreted using the Digital Image Correlation (DIC) technique. The first results obtained by carrying out tests at low speed with different transmitted torque values are discussed, appreciating the variation in the tension of the belt along the winding arc and the dependence of the radial compression of the belt from the transmitted torque. The tangential deformation of the belt under the action of different torque values and direction of rotation of the pulleys is also presented, which is consistent with that foreseen by the brush model.

Keywords Belt · Power transmissions · Brush model · Experimental bench · Digital image correlation · Creep model

F. Bucchi (✉) · F. Frendo · P. Neri
Department of Civil and Industrial Engineering, University of Pisa, Largo L. Lazzarino, 56122 Pisa, Italy
e-mail: francesco.bucchi@unipi.it

107

8.1   Introduction

Pulley–belt is a transmission system used in many industrial applications, due to its low cost, ease of implementation and maintenance requirements. Several models have been proposed to study the contact mechanics, transmission capability and the overall transmission efficiency. Euler proposed the first analyses on this topic in the XVIII century, with reference to the friction of a rope wound along a pulley. In the XIX century, Reynolds and Grashof added to the Euler analyzes the effect of speed losses due to belt deformation and the centrifugal effect. More recently, the Grashof model, mentioned in the literature as creep model, was extended. According to the creep model, the winding arc is subdivided into an adhesion arc, located at the beginning of the contact arc, and a sliding arc, located nearby the exit from the pulley. Basing on this model, along the former arc, no tangential stress occurs between the belt and the pulley and, consequently, the belt tension does not vary. Along the sliding arc, the model assumes that micro-slip (creep) occurs which originates tangential friction between the belt and the pulley and, in turn, the tension variation in the belt.

In 1970, Firbank proposed an alternative model, called shear model, which assumes that friction occurs along the whole winding arc, which is divided into a region where static friction occurs, and the belt is subject to angular deformation (shear), followed by a creep region where sliding occurs. The tangential friction along both regions contributes to the torque transmission and the belt tension varies along the whole winding arc. The Firbank model has also been extended to include extensible belts (Kong and Parker 2005).

Recently, the authors proposed an innovative model (Frendo and Bucchi 2020a), which is inspired to the brush model which is usually employed for pneumatic tires of vehicles (Bernard et al. 1977; Pacejka and Sharp 1991). This model can describe the tangential stress distribution between the pulley and the belt in steady-state conditions and to predict the angular velocity of the driven pulley when a known torque value is applied to it. This allows also to estimate the power losses of the transmission system and the elastic deformation of the belt (Bertini et al. 2014; Frendo and Bucchi 2020b). Even in this model, the winding arc is divided into different regions, depending on the friction condition, and several studies have been proposed varying the transmission parameters (Bucchi and Frendo 1038). The model was also validated by finite element analyses (Bucchi and Frendo 2022) which demonstrated the capability of this approach to reproduce, through analytical expressions, the pressure and tangential force along the winding arc, except for the pulley entrance and exit zone, were kinematic issues arise (Wasfy et al. 2016); the FE analyses also showed that the hypothesis of no tension variation along the adhesion zone, postulated by Grashof, is not strictly correct.

To the best of the authors knowledge, few studies (Della and Timpone 2013) have been devoted to the experimental study of the contact mechanics between the pulley and the belt and none of them used full-field measurements.

To fill this gap, in this paper, a test bench is presented, designed to experimentally validate the brush model developed by the authors. The bench is made up of two

pulleys connected to two shafts driven by independently controlled motors; a flat belt is installed between the pulleys, and the shafts are equipped with sensors. The belt was painted creating a suitable texture (random speckle pattern) to be interpreted using the Digital Image Correlation (DIC) technique (Barone et al. 2017; Neri et al. 2022) to measure the belt deformation and, consequently, assess the pressure and tangential actions between the belt and the pulley.

Section 8.2 recaps the key features of the brush model applied to pulley–belt transmissions. Section 8.3 details the test bench layout, describing its functioning principle and its measure capabilities. Section 8.4 recaps the DIC technique fundamentals and describes the analyses performed on the acquired images. Section 8.5 shows and discusses the results in terms of belt–pulley pressure, tangential actions, belt tension and their affinity with literature models. Conclusions are drawn in Sect. 8.6.

8.2 Brush Model Outline

The first basic hypothesis of the "brush model" is considering the belt as made of two parts: the rubber matrix being in contact with the pulley along the winding arc, and the reinforcement fibers, having the stiffness several orders of magnitude greater than the rubber matrix stiffness. The belt is assumed as a planar component, and no stress component arise along the belt width (transverse direction). In the first version of the brush model (Frendo and Bucchi 2020a), which is used in this work, the reinforcement fibers are inextensible. The same model can also be applied to belts having elastic reinforcement fibers.

The model assumes that a bed of elastically deformable bristles composes the rubber matrix. Such bristles are connected to the tension member on one end and are in contact with the pulley on the other end.

The bristles height is negligible with respect to the pulley radius, and they are ideally elastic, deformable along the tangential direction due to the speed difference between the belt inextensible tension member, which has constant speed V_b in steady-state condition, and the pulley.

If the bristle tangential deformation s is known, the contact tangential stress τ given by Eq. 8.1:

$$\tau = k_s s \tag{8.1}$$

where the parameter k_s is the bristle tangential stiffness. In order to determine the bristle tangential deformation s, two different cases are discussed, depending on the fact that the analyzed pulley is driving or driven.

Considering the belt entering in the driving the pulley, having radius R_{dg} and angular speed ω_{dg}, the bristle deformation along the driving pulley s_{dg} is expressed as a function of the angular coordinate α as follows

$$s_{\text{dg}}(\alpha) = \int_0^\alpha \frac{V_{\text{s, dg}}}{\omega_{\text{dg}}} d\tilde{\alpha} = \frac{V_{\text{s, dg}}}{\omega_{\text{dg}}} \alpha \tag{8.2}$$

where $V_{\text{s, dg}} = \omega_{\text{dg}} R_{\text{dg}} - V_{\text{b}}$ is the relative slip velocity of the belt. Equation 8.2 is valid if the static friction between the belt and the pulley is enough to bear the tangential stress, that is

$$\tau_{\text{dg}}(\alpha) = k_{\text{s}} \frac{V_{\text{s, dg}}}{\omega_{\text{dg}}} \alpha \leq f_{\text{s}} p_{\text{dg}} \tag{8.3}$$

where f_{s} is the static friction coefficient and p_{dg} is the normal pressure between the belt and the pulley. The normal pressure is computed considering the radial equilibrium of the belt and is expressed by

$$p_{\text{dg}}(\alpha) = \frac{T_{\text{dg}}(\alpha) - q V_{\text{b}}^2}{R_{\text{dg}}} \tag{8.4}$$

being $T_{\text{dg}}(\alpha)$ the belt tension along the driving pulley and q the lineic mass. The belt tension is obtainable integrating the tangential stress along the winding arc of the driving pulley. The static friction limit is then reached for a precise value of α (Frendo and Bucchi 2020a). Then, the friction regime moves from static to kinematic, usually reducing the friction coefficient. This effect produces stick-slip phenomenon along the slip zone, described in detail in Frendo and Bucchi 2020a. The tangential stress along the winding arc reduces along the sliding arc, as well as the normal pressure and the belt tension. Figure 8.1a shows an exemplificative trend of the tangential stress along the winding arc. The friction static [kinematic] limit is also shown, which is computed multiplying the normal pressure and the static [kinematic] friction coefficient. Hence, Fig. 8.1a provides also information related to the normal pressure trend. Figure 8.1b shows the belt tension along the winding arc of the driving pulley.
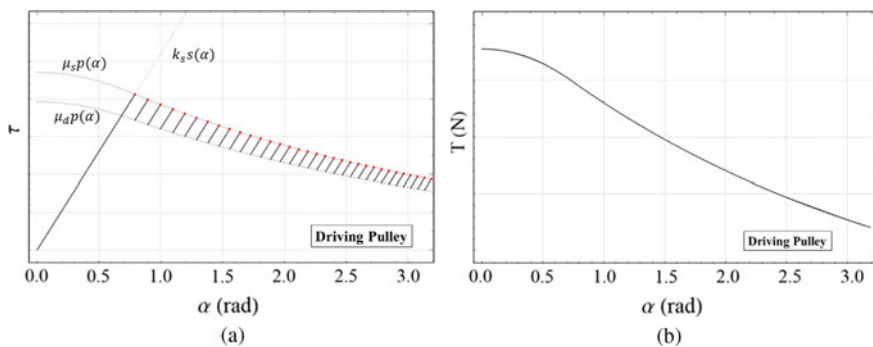
Fig. 8.1 Tangential stress (**a**) and belt tension (**b**) along the winding arc of the driving pulley (Frendo and Bucchi 2020a)

It is worth noting that the tangential stress linearly rises with α up to its maximum value, which occurs where the static friction limit is reached and then decreases. The normal pressure and the belt tension, which are directly proportional if the centrifugal effect is neglected (e.g. at low speed, see Eq. 8.4), decreases along the whole winding arc.

Concerning the driven pulley, a similar approach can be used, precisely described in Frendo and Bucchi 2020a. In such a case, the tangential stress, as well as the pressure and the belt tension, increases (if the local stick-slip phenomenon is neglected) along the winding arc.

8.3 Test Bench Description

In order to experimentally validate the brush model, a dedicated test bench was conceived. The aim of the bench was to control the angular velocity of the driving pulley and the resistant moment at the driven pulley of a dummy transmission system composed of a flat belt and two pulleys. A belt with reinforcement fibers was chosen to be used as flat belt. Due to difficulties in finding commercial flat reinforced belts, a commercial trapezoidal belt was selected, but it was used as flat belt, using the internal surface of the belt in contact with the external cylindrical surface of the pulley.

Figure 8.2 shows a picture of the test bench installed in the University of Pisa laboratory, and Fig. 8.3 shows a schematic of the data acquisition system and control logic of the test bench.

A brushless motor (BM), driven by the brushless driver (BD, not represented in Fig. 8.2), controllable either through an integrated speed control (SC) or torque control (TC), is connected to the left shaft, which is supported by two bearings. The shaft is equipped with a torque (torsiometer) and angular position/velocity (encoder) sensor, measuring the left shaft torque T_L and angular velocity ω_L, respectively. At the end of the shaft, the pulley is fixed. The whole left shaft system (motor, shaft, pulley and sensor) is installed on a sleeve whose position can be regulated by a screw. This allows to set the desired belt pre-tension.

On the other side, an asynchronous motor (AM), driven by the asynchronous drive (AD, not represented in Fig. 8.2), is connected to the right shaft, which is also equipped with a torque and angular position/speed sensor, measuring the left shaft torque T_R and angular velocity ω_R, respectively. The bearings which support the right shaft are installed on two tri-axial load cells which allow to measure the bearing forces (F_1 and F_2) and considering the shaft equilibrium, which allow to compute the belt total tension (sum of tight and loose sides of the belt, neglecting the centrifugal effect). The asynchronous motor has no integrated speed or torque control, but its speed or torque can be controlled by a PID which uses the signals measured by torque and speed sensor (Fig. 8.3 shows only the speed control case). All the measurement signals are acquired by a USB-6351 National Instrument board (DAQ), which also controls the input signal of the controllers of the motors. A
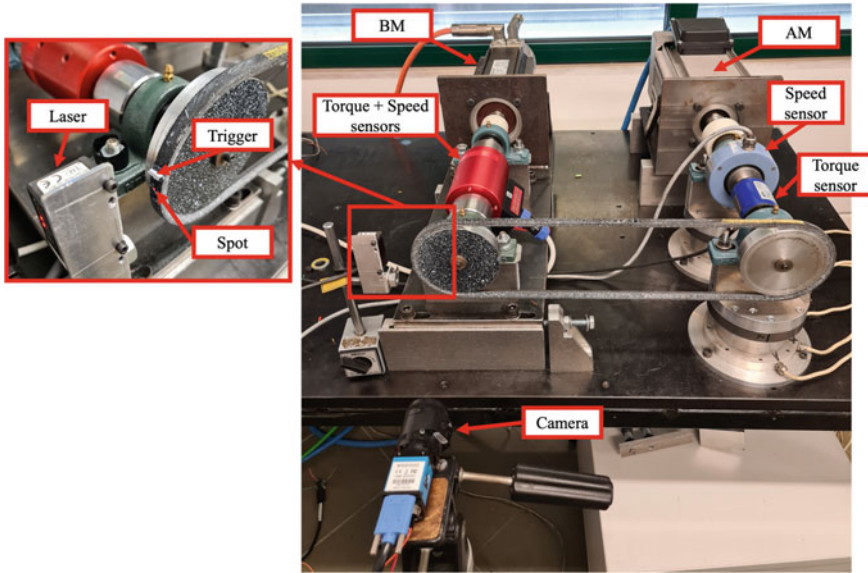
Fig. 8.2 Belt–pulley contact mechanics test bench
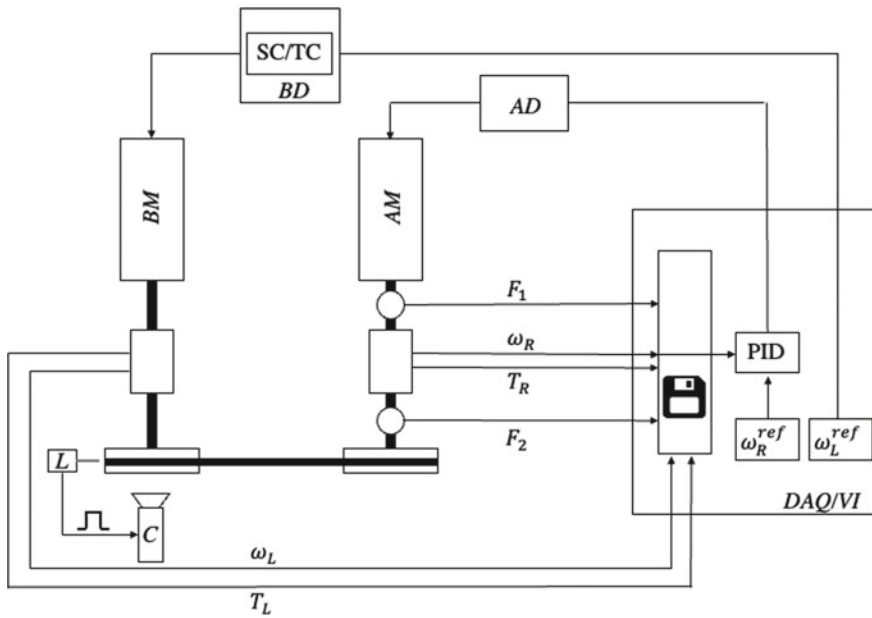
Fig. 8.3 Schematic of the logic and control of the test bench

LabVIEW virtual instrument (VI) was developed to record the data and control the motor speed.

The belt tension and pressure cannot be directly measured and, to assess them, an indirect measurement system was conceived. The image acquisition system, shown in the zoomed detail in Fig. 8.2, is made up of a camera (C) (Image sourcing DMK 23UP031), a trigger element fixed on the belt and a laser sensor (L) which detects the passage of the trigger element. Indeed, since slip occurs between the pulley and the belt, it is not possible to use the encoder installed on the pulley shaft to assess the belt position. Nevertheless, the belt has to be shot in the same position in order to correctly elaborate images using the DIC technique. For this reason, a laser sensor and a camera, which allows the trigger input, were directly connected to acquire a picture every time the trigger sensor is detected by the laser. Both the lateral surface of the belt and the frontal surface of the left pulley were painted creating a suitable texture (random speckle pattern, see Fig. 8.5), which is processed through DIC technique.

The measurement system allows to compute the belt deformation by a Digital Image Correlation (DIC) system, whose working principle is described in Sect. 8.4.

8.4 DIC Analyses Implementation

Digital Image Correlation is a well-established technique which allows for the measurement of displacements through image processing. Provided that a random pattern is available on the target object, it is possible to track the surface displacement in each frame. This can be achieved by exploiting the natural texture of the surface or, more frequently, by spraying or gluing a black and white speckle pattern on the object. Once the grid of measurement points is defined on the images, a pixel subset is associated with each point and tracked along the frame set to estimate horizontal (Δx) and vertical (Δy) displacements. This procedure is illustrated in Fig. 8.4, for two consecutive frames.
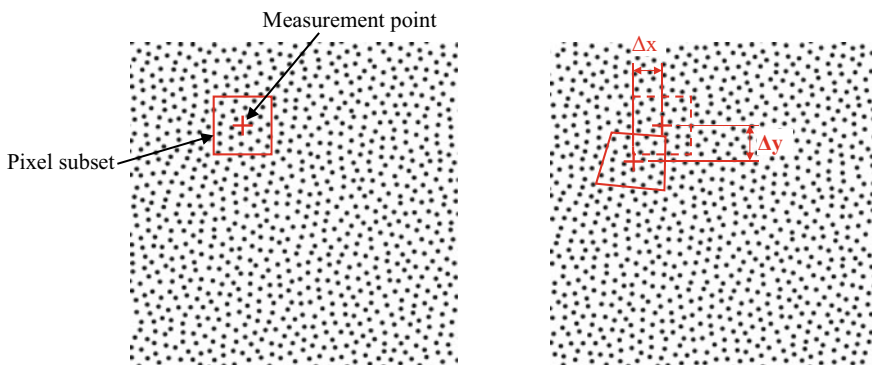
Fig. 8.4 Working principle for DIC analysis
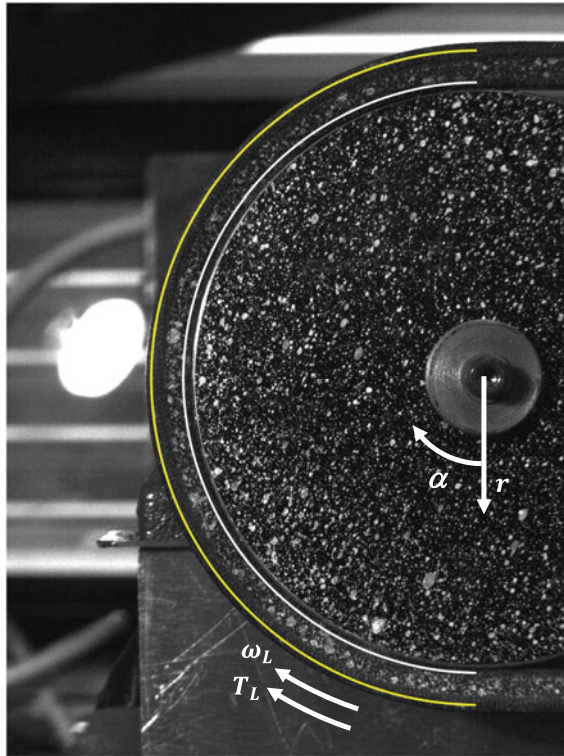
Fig. 8.5 Speckle pattern, reference system and measuring arcs on the driving pulley

In this paper, an open source 2D DIC algorithm was used to perform the task (Eberl 2010). Since the belt shows a black surface, white spray paint was used to obtain the speckle pattern, as shown in Fig. 8.5. The aforementioned algorithm provides the raw data calculation, i.e. extracting the full-field displacement information from the image set. It is worth noting that due to slip, the belt revolution period is not an integer multiple of the pulley rotation period. For this reason, the region of interest in this research is limited to the belt surface, thus, even if the speckle pattern was painted on both the pulley and the belt, only the belt measure is worth of interest. For this reason, the measurement grid was defined only on the belt area, where correlation is expected to be successful. The DIC measurement requires the definition of a reference image, which set the zero for the displacement. In this paper, the zero was set by taking a frame of the rotating belt with no torque applied to the pulley. Then, the frames were shot by subsequently increasing the torque value, thus imposing higher load to the belt, always waiting for steady-state condition. Thanks to the trigger implementation, described in Sect. 8.3, it was possible to shoot the belt at the same position, allowing to compare the images acquired for different torque values.

Three frames were taken at each torque value, to assess the measurement repeatability. The raw displacement maps are defined in the camera reference frame along the vertical and horizontal directions. Due to the typical belt deformed shape, a cylindrical reference frame centered on the pulley (Fig. 8.5) is more convenient for result interpretation. Thus, the center of the pulley was detected in the first image, by manually selecting ten points on the pulley circumference and then computing the best fitting ellipse (to account for any small misalignment between the camera and the pulley). The Cartesian raw displacement could then be converted into radial and tangential displacements. The tangential displacements were additionally normalized with respect to the distance between each measurement point and the pulley center (i.e. radius), to obtain angular displacement in radians and to allow to compare the results with the brush model, which assumes negligible belt thickness. Even if the full-field maps provide a clear and complete overview of the displacement distribution all over the belt, additional processing was performed to obtain an in-depth analysis of the results. In particular, the results corresponding to the maximum and minimum radius of the belt were selected (i.e. yellow and white line in Fig. 8.5, respectively), and the difference between radial and tangential displacements at the two radii were plotted. These results are directly related, by the knowledge of the belt radial and tangential stiffness, to the radial (pressure) and tangential stress acting between the pulley and the belt.

8.5 Test Results and Discussion

Preliminary tests were performed to assess the test bench equipment functionality. A very low speed (about 10 rpm) was imposed at the brushless motor and different constant values of resistant torque were applied using the PID implemented to control the asynchronous motor. In particular, three torque levels were imposed: (i) no resistant torque, (ii) 1.5 Nm resistant torque and (iii) 3.5 Nm resistant torque. In all the tests, in addition to the resistant torque applied by the asynchronous motor, a bias torque of 0.5 Nm had to be overcome due to bench losses (bearings).

The displacement of each point of the belt wound on the driven (brushless motor side) pulley was analyzed using DIC technique. In particular, the displacement d_r and d_t of each point of the grid were measured along the radial and tangential direction, respectively. Zero displacement refers to the torque level (i) (no resistant torque applied by the motor, only friction torque has to be overcome). Concerning the tangential displacement, to compare the displacement of different grid points having different radial coordinate, the tangential angular displacement was measured as follows:

$$d_\alpha(\alpha,\, r) = \frac{d_t(\alpha,\, r)}{r} \tag{8.5}$$

In addition, in order to analyze the tangential deformation of the belt, which is related to the tangential stress between the belt and the pulley, two arcs shown in Fig. 8.5 were selected on the grid, with the white arc corresponding to the minimum measurable radius (R_i) and the yellow arc corresponding to the maximum measurable radius (R_e) along the belt. Hence, the belt tangential deformation was defined as

$$\Delta_\alpha(\alpha) = d_\alpha(\alpha, \ R_i) - d_\alpha(\alpha, \ R_e) \tag{8.6}$$

Figure 8.6 shows the radial displacement of the belt wound on the driven pulley obtained when the resistant torque is 3.5 Nm. Since the torque applied by the brushless motor is clockwise, the tight side of the belt is on the lower part and the slack side on the upper part of the figure.

This is also confirmed analyzing the radial displacement which is negative on the bottom part of the figure and gradually changes to positive clockwise moving. The radial displacement of the belt is related to the pressure acting between the belt and the pulley and consequently, as stated in Eq. 8.4, to the belt tension (in this case, the centrifugal effect is negligible due to the very low velocity). Hence, the DIC
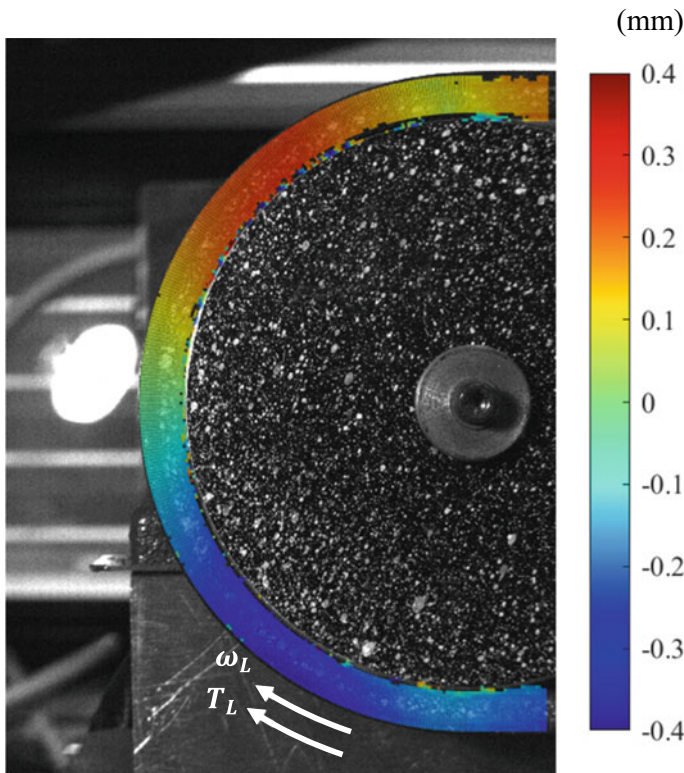
Fig. 8.6 Radial displacement of the grid elements belonging to the belt

analysis allows to measure how the belt is compressed in the lower part (entrance) and is enlarged in the lower part (exit) of Fig. 8.6, proving that the pressure and consequently the tension of the belt is higher at the pulley entrance (tight side of the belt) and lower at the pulley exit (loose side of the belt). The trend is not monotonic due to local effects at the entrance and the exit of the pulley, which will be considered in the future analysis.

Figure 8.7 shows the tangential displacement d_α for each point of the grid, for the same load condition. Neglecting the local effects nearby the entrance and exit from the pulley, all the points are subject to tangential displacement with reference to the zero-torque reference configuration; this can be attributed to small errors in the trigger setup and to the belt reinforcement fibers elasticity. It can be observed that in the central part of the winding arc, a gradient is appreciable between the angular tangential displacement at the inner and the outer radius, proving how the belt is subject to tangential stress.

To highlight the tangential deformation of the belt $\Delta_\alpha(\alpha)$ is plot in Fig. 8.8 along the whole winding arc for two different values of transmitted torque. As anticipated, $\Delta_\alpha(\alpha)$ is related (almost proportionally) to the tangential stress $\tau(\alpha)$ between the pulley and the belt. It is worth noting that the belt tangential deformation is higher as
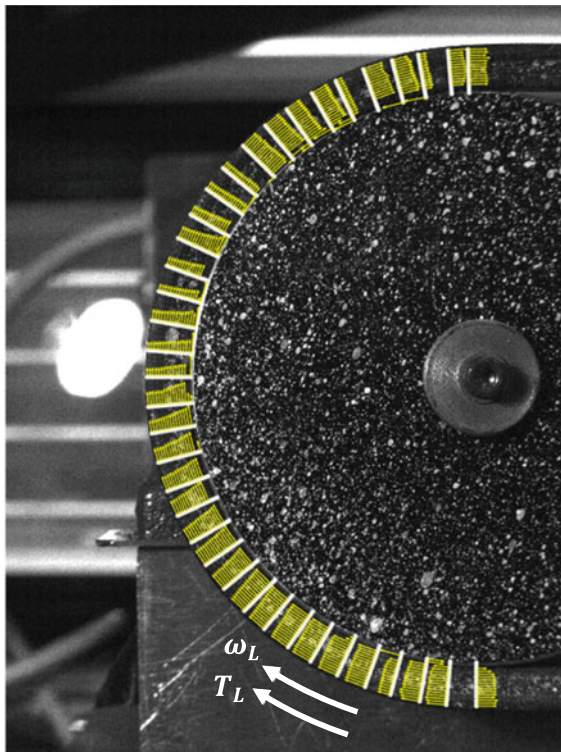
Fig. 8.7 Tangential displacement of the grid elements belonging to the belt
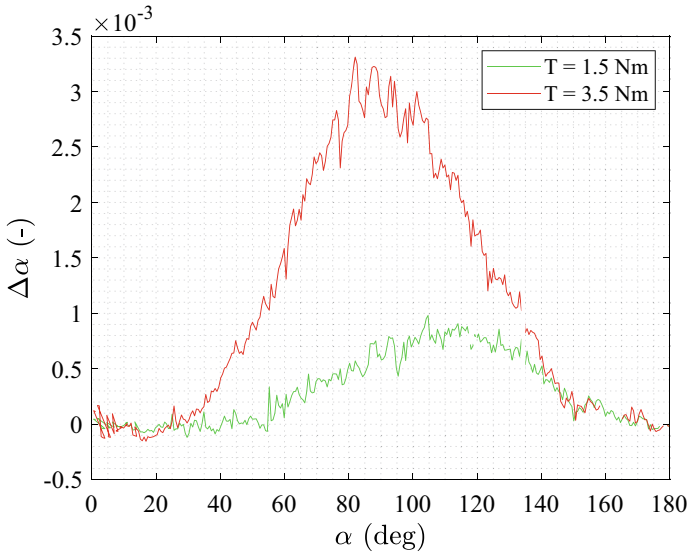
Fig. 8.8 Belt tangential deformation along the driving pulley obtained for two torque values

the transmitted torque rises, since also that the tangential stress between the pulley and the belt rises.

More worth of interest is the trend of the tangential deformation along the winding arc: neglecting the local effects at the entrance and the exit from the pulley, for both torque values $\Delta_\alpha(\alpha)$, rises almost linearly up to a maximum value. The rising slope is higher as the transmitted torque rises. Then, once the maximum value is reached, the tangential deformation decreases. This behavior is qualitatively compatible with the tangential stress plot obtained using the brush model and shown in Fig. 8.1a. Indeed, basing on the brush model, (i) $\tau(\alpha)$ linearly rises along the adhesion arc; (ii) the slope of $\tau(\alpha)$ is larger as the transmitted torque increases; (iii) $\tau(\alpha)$ reaches its maximum value when the static friction limit is reached and then decreases; (iv) the maximum value of $\tau(\alpha)$ is reached for lower values of α as the transmitted torque increases. On the contrary, if the Grashof model is considered, no tangential stress should appear along the adhesion zone and a sudden increase in the stress should verify once the slip zone is reached. This assumption seems to conflict with preliminary experimental evidence, thus confirming that the brush model is more reliable than the Grashof model.

8.6 Conclusions

In the present work, a test bench was developed to measure the contact actions between the belt and the pulley in flat belt transmissions. Two motors were used

to control the pulleys torque and speed, and a belt was painted creating a suitable texture (random speckle pattern) to be analyzed by DIC technique. Several sensors were installed on the bench, to measure the torque and angular velocity of the shaft, and a triggered camera was used to acquire belt pictures for different transmitted torque values.

A grid was created, corresponding to the belt, and the radial and tangential displacement of each point of the grid were measured for three different values of transmitted torque. The results seem promising, being the radial displacement of the belt related to the pulley–belt contact pressure and to the belt tension, and the tangential deformation related to the tangential stress between the pulley and the belt.

The preliminary results were compared with the tangential stress results obtained by the brush model, showing a fair good qualitative agreement.

In the future research, the test bench, which to the best of the authors' knowledge is novel and unique for performing such measures, will be used to collect data of a wide test campaign to characterize the belt deformation for different working conditions and compare it to theoretical and FE models results.

References

Barone S, Neri P, Paoli A, Razionale AV (2017) Digital image correlation based on projected pattern for high frequency vibration measurements. Procedia Manuf 11:1592–1599

Bernard JE, Segel L, Wild RE (1977) Tire shear force generation during combined steering and braking maneuvers. SAE technical paper, p 770852

Bertini L, Carmignani L, Frendo F (2014) Analytical model for the power losses in rubber v-belt continuously variable transmission (CVT). Mech Mach Theory 78:289–306

Bucchi F, Frendo F (2021) Analysis of belt transmissions capabilities using the brush model. IOP Conf Ser Mater Sci Eng 1038(1). IOP Publishing

Bucchi F, Frendo F (2022) Validation of the brush model for the analysis of flat belt transmissions in steady-state conditions by finite element simulation. Mech Mach Theory 167:104556

Della Pietra L, Timpone F (2013) Tension in a flat belt transmission: experimental investigation. Mech Mach Theory (70):129–156

Eberl C (2010) Digital image correlation and tracking. Mathworks, Matlab Central

Frendo F, Bucchi F (2020a) "Brush model" for the analysis of flat belt transmissions in steady-state conditions. Mech Mach Theory 143:103653

Frendo F, Bucchi F (2020b) Enhanced brush model for the mechanics of power transmission in flat belt drives under steady-state conditions: effect of belt elasticity. Mech Mach Theory 153:103998

Kong L, Parker RG (2005) Microslip friction in flat belt drives. Proc Inst Mech Eng C J Mech Eng Sci 10(219):1097–1106

Neri P, Paoli A, Santus C (2022) Stereo-DIC measurements of a vibrating bladed disk: in-depth analysis of full-field deformed shapes. Appl Sci 11

Pacejka HB, Sharp RS (1991) Shear force development by pneumatic tyres in steady state conditions: a review of modelling aspects. Veh Syst Dyn 3–4(20):121–175

Wasfy TM et al (2016) Effect of flat belt thickness on steady-state belt stresses and slip. J Comput Nonlinear Dyn 11(5)

Part V
Forming

Chapter 9
The Effect of Rubber Hardness on the Channel Depth of the Metallic Bipolar Plates Fabricated by Rubber Pad Forming

Hossein Talebi-Ghadikolaee, Majid Elyasi, Samaneh Shahgaldi, Shahaboddin Seddighi, Mohammad Mehdi Kasaei, and Lucas F. M. da Silva

Abstract   In this study, rubber pad forming is employed for the cost-effective production of metallic bipolar plates. To this end, a punch with parallel serpentine flow field patterns and a rubber layer is used to form SS316 bipolar plates with a thickness of 0.1 mm. The influence of forming force and rubber hardness on the channel depth of the bipolar plates is investigated. Results show a direct relationship between the channel depth and the applied force. The maximum channel depth is decreased by increasing the hardness of the rubber. However, a remarkable reduction in the rubber hardness reduces the system's performance in supplying the pressure required for forming microchannels and results in an unformed bipolar plate. Thus, to achieve a greater channel depth, the applied force and the rubber hardness should be increased accordingly.

Keywords PEMFC · Metallic bipolar plates · Metal forming · Rubber pad forming · Rubber hardness

H. Talebi-Ghadikolaee (✉)
Faculty of Mechanical Engineering, University of Kashan, Kashan, Iran
e-mail: h.talebi.q@kashanu.ac.ir

M. Elyasi
Mechanical Engineering Department, Babol Noshirvani University of Technology, Babol, Iran

S. Shahgaldi
Hydrogen Energy Institute, Université du Québec À Trois-Rivières (UQTR), Trois-Rivières, QC, Canada

S. Seddighi
Faculty of Mechanical Engineering, Tarbiat Modares University, Tehran, Iran

M. M. Kasaei
Institute of Science and Innovation in Mechanical and Industrial Engineering (INEGI), Porto, Portugal

Department of Mechanical Engineering, Qazvin Branch, Islamic Azad University, Qazvin, Iran

L. F. M. da Silva
Department of Mechanical Engineering, Faculty of Engineering, University of Porto, Porto, Portugal

9.1 Introduction

Due to the non-renewability of fossil fuels and the rate of pollutants from burning fossil fuels, the use of clean and renewable energy sources has grown in recent years. This way, Proton-exchange membrane fuel cells (PEMFCs) have attracted a lot of attention due to their efficiency, high current density, and low operating temperature. PEMFCs are made of various parts. Bipolar plates are one of the main components in PEMFCs. These plates are typically made of graphite, composite, and metallic materials (Blunk et al. 2003; Müller et al. 2006; Talebi-Ghadikolaee et al. 2022; Modanloo et al. 2021). Graphite plates have enhanced corrosion resistance and improved conductivity. However, they have poor mechanical strength and impose high manufacturing costs due to the need for machining operations. The drawbacks of graphite plates have led researchers to explore other alternatives to these plates. In the literature, sheet metals have been studied as an alternative to graphite plates due to their superior mechanical, thermal, and electrical properties (Bar-On et al. 2002). In addition to the advantages mentioned for metallic bipolar plates, and since bipolar plates build a significant part of the weight and manufacturing cost of PEMFCs, bipolar plates fabricated with sheet metal can noticeably reduce the fuel cell weight (Sopian and Daud 2006).

The flow field pattern is another variable in metallic and non-metallic bipolar plates that plays a critical role in fuel cell performance. Hence, various patterns are used as flow fields in bipolar plates. According to the study by Li and Sabir (2005), the flow field designs are categorized into four groups including pin-type, series-parallel, interdigitated, and serpentine.

Bipolar plates are made through three main methods, including molding, machining, and forming. The molding method is used to manufacture composite plates while forming and machining methods are used to build metallic bipolar plates. In addition, hydroforming (Piccininni et al. 2022), stamping (Zhang et al. 2022), roll forming (Zeinali et al. 2022), and rubber pad forming (Teng et al. 2022) are an example of forming techniques that could be used for manufacturing metallic bipolar plates. Among all the above methods, the rubber pad forming process is of great importance due to its simpler process, lower die cost, high manufacturing speed, and appropriate surface quality. These advantages have enabled the widespread use of this technique for forming metallic bipolar plates. During the forming process, the rubber layer is used to provide the pressure required for the deformation of the sheet metal. Therefore, the rubber layer characteristics can substantially influence the process.

Concerning the process variables and to enhance the quality of the manufactured products, numerous studies have investigated the feasibility of forming metallic bipolar plates by the rubber pad forming process.

Liu and Hua (2010) studied the forming of bipolar plates by rubber pad forming using the 2D simulation method. They evaluated the influence of die radius, draft angle, and rubber layer hardness. The results showed that an increase in the die radius leads to the better filling of channels and reduces the risk of rapture. Additionally,

the rubber layer hardness had no noticeable effect on stress distribution in the manufactured plates, and an increase in the draft angle mitigated the force required for forming.

Lim et al. (2013) studied a titanium plate with a thickness of 0.1 mm through the rubber layer forming process. For this purpose, a 200-ton press was used to shape the plates. In this study, the effects of punch speed, pressure applied to the assembly, rubber pad thickness, rubber pad hardness, and draft angle on the depth of the channel have been investigated. According to the results, the channel depth in the manufactured products was improved by increasing the rubber pad thickness and reducing the hardness of the rubber layer. They eventually obtained optimal values of the forming variables by considering the effect of the variables on the channel depth in the bipolar plates.

Jeong et al. (2014) investigated the effect of punch speed, the pressure applied on the assembly, rubber thickness, and rubber hardness on forming SS304 bipolar plates. The results showed that the depth of the channels is directly related to the punch speed, pressure, and rubber thickness. In addition, a reduction in the rubber hardness improved the process of forming plates. Furthermore, increasing the draft angle, especially from 10 to 20°, improved the forming condition. The depth of the channels was not significantly altered from 20 to 30°. Hence, the angle of 20° was more desirable.

Kolahdooz et al. (2017) investigate the effect of various factors in rubber pad forming of metallic bipolar plates using the integration of finite element method and design of experiment. They showed that outer corner radius, draft angle, and the friction coefficient are the most critical parameters in the forming process.

Talebi-Ghadikolaee et al. (2020) studied the rubber pad forming of metallic bipolar plater, and they proposed a reliable method for predicting the fracture onset during the plastic deformation of the sheet metal. According to their results, the finite element model together with the normalized Cockroft–Latham criterion presented the most accurate prediction of the process (plastic and fracture behavior). Rubber pad forming of Cu/Ni clad foil microchannel was investigated by Wang et al. (2022). They used a rigid convex die (RVD) and a rigid concave die (RCD) to fabricate the bipolar plates. According to their results, higher forming loads were needed in the RCD method and the stress–strain increased when the microchannel was created using the RCD method.

As mentioned above, previous studies have investigated the effect of the rubber layer on the channel depth of bipolar plates. However, given that a greater channel depth can noticeably enhance the performance and efficiency of the fuel cell assembly, it is crucial to conduct other studies to achieve greater channel depths, which is of great importance due to the low thickness (0.1 mm) of the desired plate.

Furthermore, research has reported the advantage of reducing the rubber layer hardness in increasing the depth of the channel. However, a reduction in the rubber layer's hardness will behave contrarily and reduces the channel's depth when greater channel depths are required. This problem has not been investigated in the literature.

Additionally, since the rubber layer is a process component and remarkably affects the processing costs, it is crucial to evaluate its behavior under various conditions to determine the best item for the forming process. Accordingly, this study investigates the parameters mentioned above quantitatively.

9.2 Methods and Procedures

9.2.1 Material Characterization

In this study, SS316 stainless steel sheets with a thickness of 0.1 mm were used to manufacture bipolar plates with a serpentine flow field pattern and an approximate width and length of 55 mm. In order to determine the mechanical properties of the sheet, samples have been prepared by a wire cut machine according to ASTM E8M-04. Then, the samples were tested until fracture using the SANTAM Universal Tensile Test Machine (model: STM 250) with a loading capacity of up to 25 tons. The samples and the tensile test results including the engineering and true strain–stress curves are shown in Fig. 9.1. The plastic behavior was modeled using the Swift hardening law as follows:

$$\sigma = 1215(\varepsilon + 0.04)^{0.53} \tag{9.1}$$

where σ is the true flow stress and ε is the true strain.
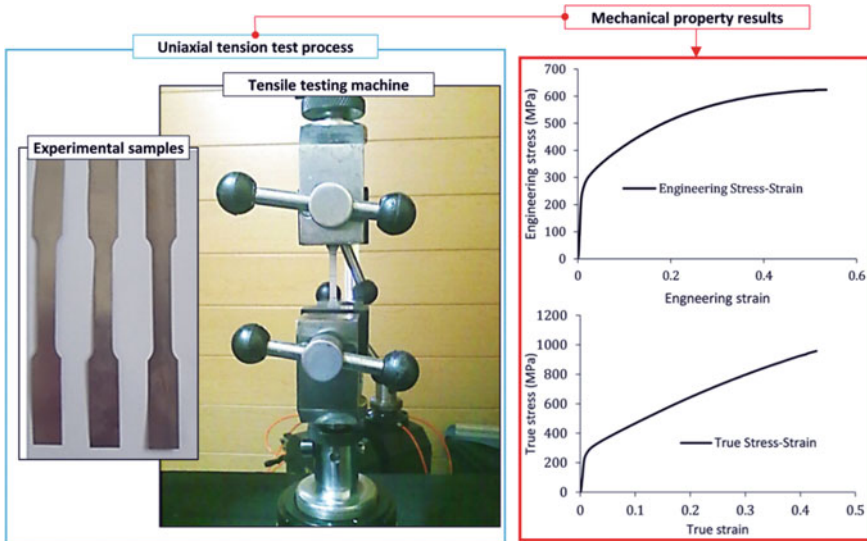
Fig. 9.1 Uniaxial tension test procedure together with the mechanical properties results

9.2.2   Rubber Pad Forming Experiments

First, the required tools were fabricated to perform the rubber pad forming experiments (refer to Fig. 9.2). The punch consists of the main body and a rectangular insert made of SPK steel with a length of 100 mm and a width of 140 mm. In order to form bipolar plates, both convex and concave patterns can be utilized. In this work, the channels of the desired bipolar plate were machined in the form of convex patterns on the insert by a CNC milling machine. As shown in Fig. 9.2, the patterns created on the die have a channel width of 1.1 mm and a draft width of 1.2 mm. Furthermore, to avoid any potential rapture in the plate, the draft angle was set at 10°, and the radius of the upper and lower corners was considered to be 0.2 mm. Figure 9.2 shows the press system, the punch, and the machined patterns on the punch.

In the experiments, the rubber layer was employed as the matrix and placed in a chamber with a cavity proportional to its dimensions. The rubber layer was made from polyurethane with 60, 85, and 90 Shore A hardness while the layer thickness was constant and equal to 20 mm. A distance of 2 mm was considered between the
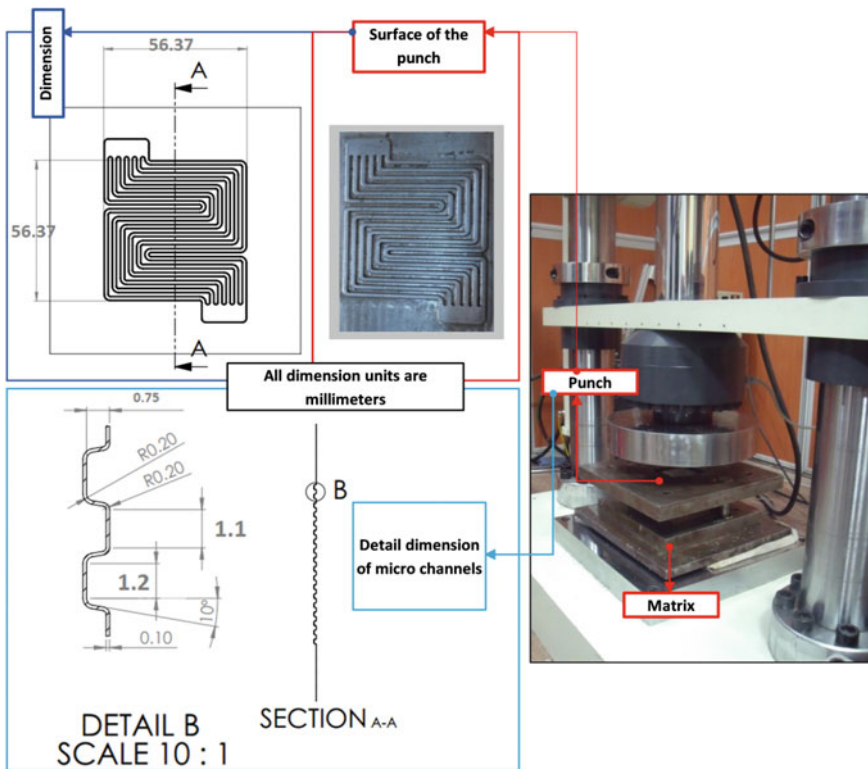

Fig. 9.2 Experimental equipment and the microchannels dimension

lateral sides of the punch and the rubber chamber (clearance) to avoid wearing the punch edge and the rubber holding chamber.

The rubber pad forming process was started by placing the sheet on the matrix. Then, the upper press jaw was driven after adjusting the desired force on the press. As a result, the rubber underwent elastic deformation and exerted pressure on the sheet to plastically deform and fill the patterns of the punch. Due to the importance of forming force and its possible relationship with the hardness of the rubber layer, specimens were formed by applying 400, 500, 800, 1000, and 1200 kN forces.

9.2.3 Measurement of the Channel Depth

In order to evaluate and analyze the specimens and obtain data about the channel depth of the bipolar plates fabricated under various conditions, the specimens were cut in longitudinal, transverse, and diagonal directions, as shown in Fig. 9.3. The specimens then underwent further operations to prepare the cut cross-section and enhance measurement accuracy. In addition, due to the poor quality of the specimens' cross-section after cutting by wire cut machine, the cut surfaces were molded with epoxy resin to enhance the measurement accuracy. Then, specimens were sanded and polished to enhance the quality of the cross-sections.

Afterward, an optical microscope (4 × and 10 × magnification) equipped with surface measurement, and analysis software was used to measure the intended parameters. Firstly, to measure the depth of the channels, microscope images of their cross-section were taken. Then, the depth of the channels was measured by analyzing
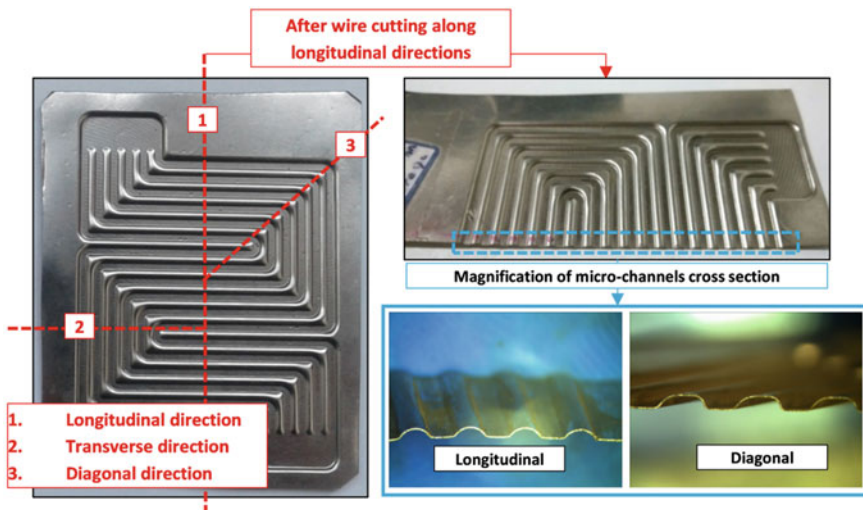

Fig. 9.3 Fabricated specimens, cutting directions together with a magnified cross-section view

images and data obtained from measuring tools embedded in the relevant software. The channel depth of the formed plates was considered as the distance between the flat zone of the specimen and the end of the dome shape area.

9.3   Results and Discussion

9.3.1   The Effect of Applied Force on the Channel Depth

The effect of applying 400–1200 kN forces on the channel depth located in different directions of 316 stainless steel bipolar plates was investigated. For this purpose, a 20 mm-thick rubber layer with 90 Shore A was used. According to Fig. 9.4, the channel depth increases by raising the applied force. The highest channel depth in the transverse, longitudinal, and diagonal directions were 0.592, 0.568, and 0.61 mm, respectively. This occurs due to the increased deformation of the rubber layer upon increasing the force and, consequently, applying more force to the metallic plate and its higher deformation. This increase continues until the rubber layer can supply the pressure required in the chamber. The channel depth under various forces in the diagonal direction was higher than that in other directions. This is due to the larger space of the channels in this direction, which results in the easier flow of the rubber layer and thereby applying more force on the sheet. Ultimately, this leads to more deformation of the sheet and increases the channel depth. However, with the increase of the applied force, the difference between the channel depths in three directions decreases.
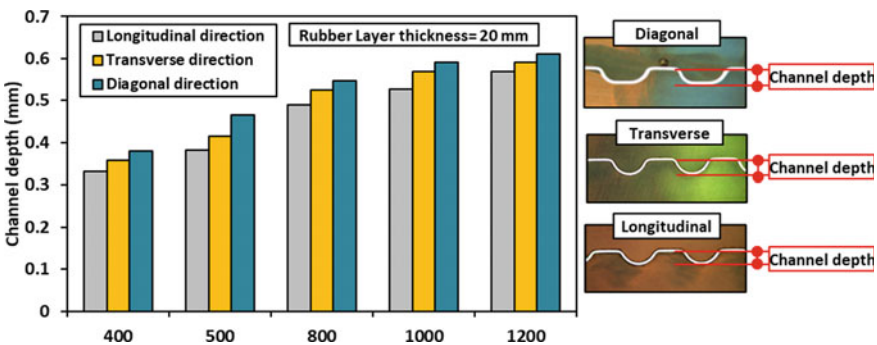

Fig. 9.4   Effect of applied force on channel depth

9.3.2 The Effect of Rubber Layer Hardness on the Channel Depth

Figures 9.5 and 9.6 show the results of investigating the effect of rubber hardness on the channel depth in the longitudinal and transverse directions, respectively. The results show an increase in the channel depth by decreasing rubber layer hardness at a low force of 400 kN. On the other hand, according to the observations, rubbers with low hardness slide from the space between the rubber layer chamber and the punch. This results in a considerable deformation of this region and the collapse of the rubber layer. In fact, this phenomenon avoids supplying the pressure required for forming by the rubber layer. Hence, the rubber layer with 60 Shore A cannot supply the pressure required in the chamber under the applied force of 800 kN. As a result, the highly-deformed rubber easily slides from the space between the punch and the rubber layer chamber and cannot form desired plates. The same process occurs when using a rubber layer with 85 Shore A and the applied force of 1000 kN force, which leads to inefficiency of the rubber layer and its collapse at higher forces. For this reason, the channel depth at forces above 1000 kN in the rubber layer with 85 Shore A was set at zero.

According to Figs. 9.5 and 9.6, the maximum channel depth (0.592 mm) was obtained in the rubber layer at 90 Shore A when applying a force of 1200 kN. The same results were also obtained in the longitudinal direction (Fig. 9.6). In this direction, the maximum channel depth (0.568 mm) was observed in the rubber layer at 90 Shore A when applying a force of 1200 kN.
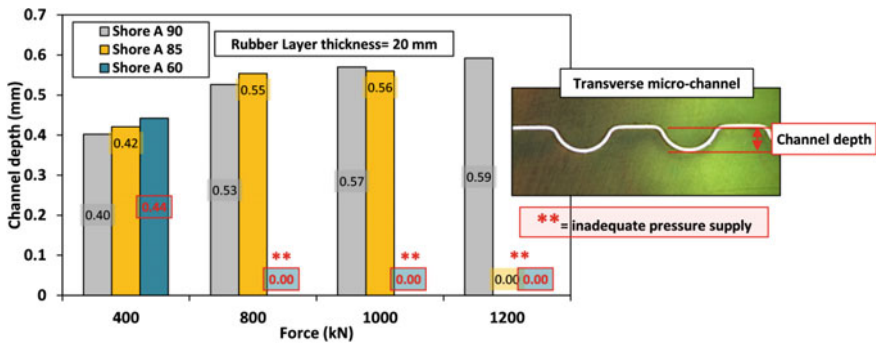
Fig. 9.5 Effect of rubber hardness on the channel depth in the transverse direction
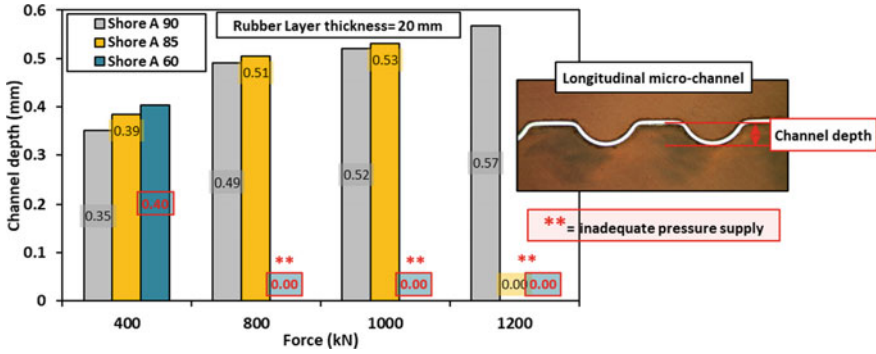
Fig. 9.6 Effect of rubber hardness on the channel depth in the longitudinal direction

9.3.3   Rupture Criterion

One of the most important parameters involved in the forming of metallic bipolar plates is predicting a rupture in the plate, which varies depending on the materials and their properties. Choosing a proper rupture criterion that agrees well with the experimental results can help to select an appropriate sheet metal to avoid any possible rupture. In this study, the "maximum thinning" parameter was employed to investigate rupture. The maximum thinning is determined using Eq. 9.2.

$$\text{Thininng} = \frac{t_0 - t_f}{t_0} \tag{9.2}$$

where t_0 is the plate's initial thickness. The final thickness (t_f) is obtained from Eq. 9.3.

$$t_f = t_0 \exp(\varepsilon_t) \tag{9.3}$$

On the other hand, the major engineering strain (e_θ) under the plane strain conditions is estimated by the empirical equation proposed by the North American Deep Drawing Research Group (NADDRG) according to Eq. 9.4:

$$e_\theta = \frac{\left[\left(23.3 + \frac{360}{25.4} t_0\right)\left(\frac{n}{0.21}\right)\right]}{100} \tag{9.4}$$

where n is the strain hardening and t_0 is the initial thickness of the sheet. On the other hand, under the plane strain condition, the major true strain and the thickness strain ε_t can be obtained from Eqs. 9.5 and 9.6.

$$\varepsilon_\theta = \ln(1 + e_\theta) \tag{9.5}$$

$$\varepsilon_t = -\varepsilon_\theta \tag{9.6}$$

The value t_f is obtained according to Eqs. 9.4–9.6 and calculating ε_t and then substituting it in Eq. 9.3. Then, the maximum thinning is obtained from Eq. 9.2. Concerning the above steps and calculations, the maximum thinning for SS316 sheet metal was estimated at 37%. To assess the accuracy of the results of the criterion utilized to determine rupture, specimens that were exposed to rupture in the experiments were employed. For this purpose, the thickness of the formed bipolar plate was measured in the regions adjacent to the rupture area. The minimum measurable thicknesses in the mentioned area were obtained, and their mean value (0.66 mm) was calculated as the minimum measurable thickness. In this study, the experimental thinning limit value was determined equal to 34% indicating a 3% error compared to the value determined by the proposed criteria (37%). The results indicate the compatibility of the experimental results with the criterion used for predicting rupture.

Accordingly, based on the results of the utilized rapture criterion, the strain hardening of the plates should exceed 0.53 to achieve thicknesses less than 0.66 mm (higher channel depth) without any rupture in fabricated microchannels.

9.4   Conclusions

In this study, the feasibility of forming SS316 bipolar plates with a thickness of 0.1 mm by the rubber pad forming process for use in PEMFCs was investigated. For this purpose, the effect of process variables, including force and rubber layer hardness, on the channel depth of the bipolar plates, which is among the factors affecting fuel cell performance and efficiency, was investigated.

The results showed the filling of the microchannels in the diagonal direction was higher than that in the other two directions. This was due to the larger channel space in this direction and the easier flow of the rubber layer. It was also found that at the applied force of 400 kN, harder rubbers are less efficient than softer rubbers in terms of channel depth. Nonetheless, at forces above 400 kN, softer rubbers are poorly efficient, while harder rubbers can supply the pressure required for forming the sheet, and therefore, the channel depth is increased by applying higher forces. For these reasons, the maximum channel depth (0.61 mm) was obtained in the diagonal direction in the rubber hardness of 90 Shore A and the applied force of 1200 kN. The utilized rapture criterion based on the initial thickness and the strain hardening exponent was capable of predicting the maximum allowable thinning during the rubber pad forming of metallic bipolar plates. Thus, this criterion can be used for designing this process.

References

Bar-On I, Kirchain R, Roth R (2002) Technical cost analysis for PEM fuel cells. J Power Sources 109:71–75. https://doi.org/10.1016/S0378-7753(02)00062-9

Blunk RH, Lisi DJ, Yoo YE, Tucker CL III (2003) Enhanced conductivity of fuel cell plates through controlled fiber orientation. AIChE J 49:18–29. https://doi.org/10.1002/aic.690490104

Jeong MG, Jin CK, Hwang GW, Kang CG (2014) Formability evaluation of stainless steel bipolar plate considering draft angle of die and process parameters by rubber forming. Int J Precis Eng Manuf 15:913–919. https://doi.org/10.1007/s12541-014-0417-7

Kolahdooz R, Asghari S, Rashid-Nadimi S, Amirfazli A (2017) Integration of finite element analysis and design of experiment for the investigation of critical factors in rubber pad forming of metallic bipolar plates for PEM fuel cells. Int J Hydrogen Energy 42:575–589. https://doi.org/10.1016/j.ijhydene.2016.11.020

Li X, Sabir I (2005) Review of bipolar plates in PEM fuel cells: flow-field designs. Int J Hydrogen Energy 30:359–371. https://doi.org/10.1016/j.ijhydene.2004.09.019

Lim SS, Kim YT, Kang CG (2013) Fabrication of aluminum 1050 micro-channel proton exchange membrane fuel cell bipolar plate using rubber-pad-forming process. Int J Adv Manuf Technol 65:231–238. https://doi.org/10.1007/s00170-012-4162-8

Liu Y, Hua L (2010) Fabrication of metallic bipolar plate for proton exchange membrane fuel cells by rubber pad forming. J Power Sources 195:3529–3535. https://doi.org/10.1016/j.jpowsour.2009.12.046

Modanloo V, Talebi-Ghadikolaee H, Alimirzaloo V, Elyasi M (2021) Fracture prediction in the stamping of titanium bipolar plate for PEM fuel cells. Int J Hydrogen Energy 46:5729–5739. https://doi.org/10.1016/j.ijhydene.2020.11.088

Müller A, Kauranen P, Von Ganski A, Hell B (2006) Injection moulding of graphite composite bipolar plates. J Power Sources 154:467–471. https://doi.org/10.1016/j.jpowsour.2005.10.096

Piccininni A, Cusanno A, Palumbo G, Zaheer O, Ingarao G, Fratini L (2022) Reshaping end-of-life components by sheet hydroforming: an experimental and numerical analysis. J Mater Process Technol 117650. https://doi.org/10.1016/j.jmatprotec.2022.117650

Sopian K, Daud WRW (2006) Challenges and future developments in proton exchange membrane fuel cells. Renewable Energy 31:719–727. https://doi.org/10.1016/j.renene.2005.09.003

Talebi-Ghadikolaee H, Elyasi M, Mirnia MJ (2020) Investigation of failure during rubber pad forming of metallic bipolar plates. Thin-Walled Struct 150:106671. https://doi.org/10.1016/j.tws.2020.106671

Talebi-Ghadikolaee H, Ahmadi Khatir F, Seddighi S (2022) Numerical-experimental study on the thickness distribution of metallic bipolar plates for PEM fuel cells. Iran J Hydrogen Fuel Cell 9:1–18. https://doi.org/10.22104/IJHFC.2021.5217.1230

Teng F, Wang H, Shi S, Jiang L, Sun J, Sun J, Zhang S (2022) Simulation and experimental researches on multi-plate rubber pad forming of two-step micro-channel based on different forming driving models. Int J Adv Manuf Technol 120:4147–4157. https://doi.org/10.1007/s00170-022-09007-4

Wang C, Wang H, Wang Y, Chen G, Zhu Q, Zhang P (2022) Investigation on forming methods in rubber pad forming process used for fabricating Cu/Ni clad foil microchannel. J Manuf Process 76:771–785. https://doi.org/10.1016/j.jmapro.2022.03.005

Zeinali MS, Naeini HM, Talebi-Ghadikolaee H, Panahizadeh V (2022) Numerical and experimental investigation of fracture in roll forming process using Lou–Huh fracture criterion. Arab J Sci Eng 1–12. https://doi.org/10.1007/s13369-022-06662-3

Zhang P, Pereira MP, Rolfe BF, Wilkosz DE, Hodgson P, Weiss M (2022) Investigation of material failure in micro-stamping of metallic bipolar plates. J Manuf Process 73:54–66. https://doi.org/10.1016/j.jmapro.2021.10.044

**Part VI
Joining**

Chapter 10
Numerical Investigation of the Influence of a Movable Die Base on Joint Formation in Semi-tubular Self-piercing Riveting

Fabian Kappe, Simon Wituschek, Vincenzo de Pascalis, Mathias Bobbert, Michael Lechner, and Gerson Meschut

Abstract Due to economic and ecological requirements and the associated trend towards lightweight construction, mechanical joining technologies like self-piercing riveting are gaining in importance. In addition, the increase in lightweight multi-material joints has led to the development of many different mechanical joining technologies which can only be applied to join a small number of material combinations. This leads to low process efficiency, and in the case of self-piercing riveting, to a large number of required tool changes. Another approach focuses on reacting to changing boundary conditions as well as the creation of customised joints by using adaptive tools, versatile auxiliary joining parts or modified process kinematics. Therefore, this study investigates the influence of increased die-sided kinematics on joint formation in self-piercing riveting process. The aim is to achieve an improvement of the joint properties by superimposing the punch feed. Furthermore, it is intended to reduce required tool changes due to the improved joint design. The investigations were carried out by means of a 2D-axisymmetric numerical simulation model using the LS-Dyna simulation software. After the validation of the process model, the die was extended to include driven die elements. Using the model, different kinematics as well as their effects on the joint formation and the internal stress concentration could be analysed. In principle, the increased actuator technology enabled an increase of the interlock formation for both pure aluminium and multi-material joints consisting of steel and aluminium. However, the resulting process forces were higher during the process phases of punching and spreading.

Keywords Self-piercing riveting · Versatility · Die-side kinematic · FEM

F. Kappe (✉) · M. Bobbert · G. Meschut
Laboratory for Material and Joining Technology (LWF), Paderborn University, Pohlweg 47-49, 33098 Paderborn, Germany
e-mail: kappe@lwf.uni-paderborn.de

S. Wituschek · M. Lechner
Institute of Manufacturing Technology (LFT), Friedrich Alexander University Erlangen Nuremberg, Erlangen, Germany

V. de Pascalis
Paderborn University, Paderborn, Germany

10.1 Introduction

The climate change is leading to the introduction of strict climate targets in various countries. For example, a reduction in greenhouse gases in the European Union of 55% of the 1990 level by 2030 is intended (European Commission 2022). The automotive sector is one major contributor to the generation of greenhouse gases. In the EU, for example, the automotive sector accounted for about 24% of all greenhouse gas emissions (OECD 2022). In order to reduce this proportion, various strategies are being pursued, such as the development of new drive concepts. Another approach pursues the increased use of multi-material constructions with the aim of reducing weight in vehicle structures and thus saving CO_2 emissions (Martinsen et al. 2015). Using a multi-material construction method, different materials like (high-strength) steel, magnesium and aluminium are combined with each other. These materials differ in their mechanical, thermal and geometric properties. The overarching objective is to adapt the structure to the application of load and thus reduce the weight required. However, the different properties of the materials used are causing the currently increasingly used thermal joining processes to reach their limits of application. For this reason, mechanical joining technologies are increasingly being used for such joints. Self-piercing riveting (SPR), mentioned in DIN 8593-5, is one of the mostly used mechanical joining processes. Some of the advantages of this process are the high load capacity behaviour that can be achieved as well as the joining of two or more sheets with similar or dissimilar materials in only one process step. To create a joint, an auxiliary joining element is used. After cutting through the punch-sided sheet, the rivet forms an interlock by expanding in the die-sided joining partner (see Fig. 10.1). Hereby, a force-fit and form-fit joint is created. The quality of a SPR joint can be determined by predefined geometric characteristics such as the interlock (f), the minimum die-side material thickness (t_r) and the rivet head position (p_h) which can be measured in a macrosection. In addition, the load-bearing capacity can be determined (DVS/EFB-Merkblatt 3410 2018).
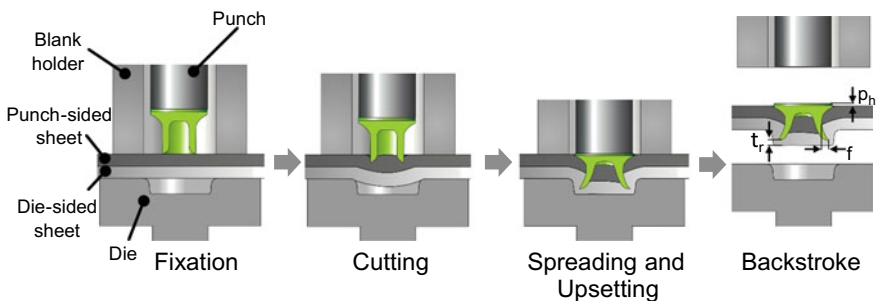
Fig. 10.1 Process sequence of the SPR process (Kappe et al. 2022a)

Initially, the SPR process was developed to join aluminium-aluminium joints. The development of modified rivet and die geometries also enables joining of (high-strength) steel-aluminium joints. However, if materials with brittle material such as aluminium castings or ultra-high-strength materials such as press hardened steels are to be joined, the conventional SPR process reaches its application limits (Meschut et al. 2022). One possibility for the expansion of the application limits is given by the development of new process routes. Local conditioning of the joining zone and the resulting change in the material structure enabled the use of conventional semi-tubular pierce riveting technology for press-hard materials, which are arranged as punch-sided material (Meschut et al. 2014). Brittle material imposes particular challenges on the mechanical joining technique due to its tendency to crack. Through the use of a rotating rivet and the resulting plasticisation of the material, brittle material can be arranged as a punch-sided material and joined in a process-safe manner (Li et al. 2013). Kappe et al. (2022b) have presented a new riveting technology that combines multi-range capable rivets with an extended punch-sided tool actuator technology. The V-SPR process presented here enables a flexible reaction to changes of the sheet thickness. At the same time, a load-bearing behaviour comparable to that of conventional semi-tubular self-pierce riveting was demonstrated in the investigation using pure aluminium joints.

The development of new joining processes can, as shown above, extend the process limits of the conventional semi-tubular riveting process and increase flexibility. However, this is also accompanied by increased complexity, and in some cases, a reduction in process efficiency. In particular, the necessary rivet and die changes increase the required process time. One way to prevent tool changes is the use of cluster analysis. Hereby, the required number of rivet-die combinations can be significantly reduced. In addition, investigations by Kappe et al. (2022a) showed that changing the rivet-die combination has only a slight influence on the joint load-bearing capacity. Another approach to reduce the number of rivets required is to influence the joint formation by means of driven die elements. Technical approaches to implement this technology in a mandrel die could already be demonstrated by Donhauser et al. (1998). Drossel and Jäckel (2014) were able to show that the joining of brittle aluminium material can be achieved by using motion in the bottom of the die. In addition, it could be demonstrated for the self-pierce riveting process with solid rivet that the use of a divided die could achieve some advantages with regard to the resulting process force, the deformation of the sheets as well as the process limits (Neugebauer et al. 2010).

In this study, the influence of moving die elements on the joint formation of an aluminium joint and a multi-material joint of aluminium and steel is analysed. The aim is to influence and extend the operating limits of a single rivet by changing its expansion behaviour.

10.2 Experimental Procedure

Materials

In this investigation, two different typical automotive material thickness combinations and materials are used. The first combination consists of a pure aluminium joint made of the aluminium alloy EN AW-6014 in temper T4 with sheet thickness 2.0 mm (Combination A). In addition, a multi-material joint made of EN AW-6014 with sheet thickness 2.0 mm as punch-sided material and the dual-phase steel HCT590X + Z with sheet thickness 1.5 mm as die-sided material is investigated (Combination B). The multi-material joint was selected against the preferred joining direction hard in soft to prevent the increasing spreading effect of a resulting steel slug. The chemical composition as well as the stress–strain curves of the two materials are given in Table 10.1

Numerical Set-up and Validation

The investigation of the influence of movable die base in SPR process is conducted using numerical methods. For this purpose, two 2D-axisymmetric simulation models using the finite element method are set up. Figure 10.2 shows exemplary the numerical design based on the multi-material joint. The models are set up in the LS-Dyna simulation software and calculated implicitly using the solver smp_d_R910.

The punch as well as the die are modelled as elastic components in order to measure the occurring process forces. The process is controlled by displacement of the punch. The movement is adapted to the material flow of the parts to be joined, the design of the joint in terms of minimum die-side material thickness, interlock and the rivet head position. The blank holder, which applies a constant load, is modelled as rigid body. After setting of the rivet, the joint is relieved by the simulated backstroke of the punch in order to evaluate the joining properties without load.
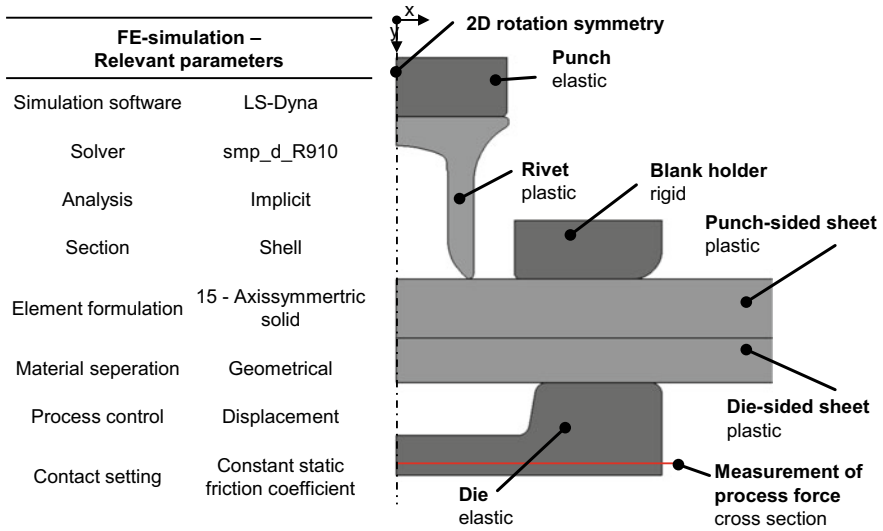
The material properties are implemented in the simulation using the experimentally determined flow curves, which were shown above. Static coefficients of friction were used to describe the contact behaviour between the different parts.

As large deformation takes place within the sheets and the rivet, a re-meshing algorithm is used for these elements to avoid local penetrations or distortions of the elements. The complete re-meshing of the parts to be joined takes place in previously defined time steps with a predefined element length of 0.05 mm.

In order to validate the simulation model, SPR-joints of both combinations are produced on a TOX TE-X joining system. This system enables maximum forces of up to 80 kN. The punch feed is realised using a servo-electric drive, which is controlled by force for all joints. To create the pure aluminium joint, a force of 40 kN is used. The multi-material joint was set with a force of 55 kN. To create the joints, a constant joining speed of 20 mm/s was selected. Both joints are created using a standard C-rivet of hardness H4, a rivet diameter 5.3 mm and a rivet length of 5.5 mm. In addition, for both joints, a flat die with a depth 1.8 mm and a diameter of 9.0 mm was used. The validation is carried out on the basis of the geometric design of the joint as well as the quality-relevant characteristics and the determined process curve.

Table 10.1 Chemical composition of the used aluminium alloy EN AW-6014 T4 (Novelis Global Automotive 2019) and the dual-phase steel HCT590X (Salzgitter Flachstahl GmbH 2017) and mechanical properties of both materials according to (Böhnke et al. 2021)

EN AW-6014 T4

Chemical composition (weight %)

Elements	Si	Fe	Cu	Mn	Mg	Cr	Zn	Ti	V
Min	0.30			0.05	0.40				
Max	0.60	0.35	0.25	0.20	0.80	0.20	0.10	0.10	0.10

HCT590X

Chemical composition (weight %)

Elements	C	Si	Mn	P	S	Al	Cr + Mo	Nb + Ti
Min						0.015		
Max	0.15	0.75	2.50	0.04	0.015	0.15	1.40	0.15

Mechanical properties

Test method	Quasistatic tensile test
Test speed	15 mm/min
Deformation measurement	GOM Aramis
Specimen geometry	According to DIN 50125

FE-simulation – Relevant parameters	
Simulation software	LS-Dyna
Solver	smp_d_R910
Analysis	Implicit
Section	Shell
Element formulation	15 - Axissymmertric solid
Material seperation	Geometrical
Process control	Displacement
Contact setting	Constant static friction coefficient

Fig. 10.2 Numerical design and simulation boundary conditions of the set-up self-piercing riveting process model based on the multi-material joint

Figure 10.3 shows the results of the validation for the pure aluminium joint as well as the multi-material joint. The validation is carried out by comparing the numerically calculated geometry with an exemplary macro section and the alignment of the determined force-displacement curves. In order to be able to map the experimental scattering, a sample number of 5 was chosen. The formation of the geometry shows a high degree of agreement. The filling of the die and the flow behaviour of the die-side material around the rivet foot are reproduced well. Slight deviations can be detected in the rising behaviour of the slug in the rivet shank. The spreading of the rivet in the simulation is marginally overestimated. The comparison of the force-displacement curves also shows a high degree of agreement. Overall, the resulting differences are within a reasonable range. For this reason, the simulation is considered to be valid and used for the further course of the investigation.

The validation of the multi-material combination is also carried out to the scheme mentioned above. The comparison of the simulation likewise reveals a high degree of agreement when comparing the calculated shape and the force-displacement curve. The simulation slightly overestimated the quality-relevant characteristics. The profile of the force-displacement curve as well as the maximum force is reproduced very well. The material flow within the die and into the rivet shank is accurately reproduced. Again, the simulation is considered to be valid and used for the further investigation.
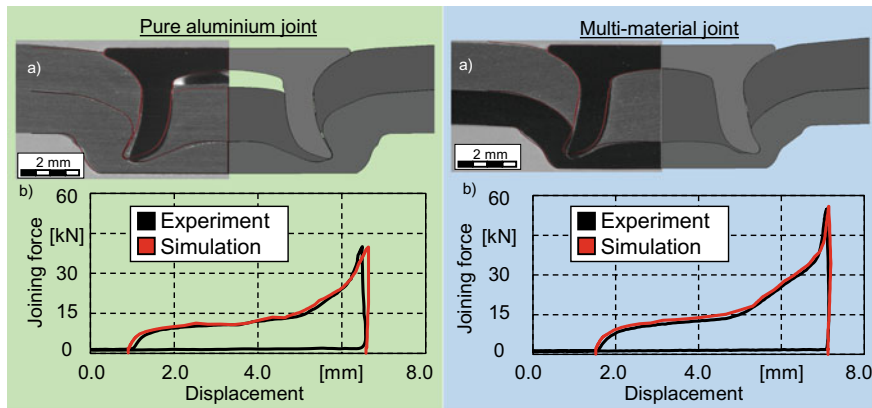
Fig. 10.3 Validation of the simulation model of the pure aluminium joint (green) as well as the multi-material joint (blue) by means of joint formation (**a**) and the comparison of the force-displacement curve (**b**)

10.3   Results and Discussion

In order to investigate the influence of die kinematics on joint formation in semi-tubular self-piercing riveting, the simulation model shown in Fig. 10.2 is adapted. The die, which is normally manufactured as one component, is divided into a rigid die sleeve and a movable die base in this numerical study. However, the diameter and depth of the die are maintained. This modified model is used to investigate two different kinematics, which are shown schematically in Figs. 10.4 and 10.5.

A continuously lowering die base is used in kinematic 1. At the beginning of the process, the movable base is at the same height as the rigid die diameter. An anvil die is created. After penetration of the rivet into the punch-sided joining part, the die base receives a feed and thus releases the die volume. During the entire joining process, the joining zone is superimposed with compressive stresses.
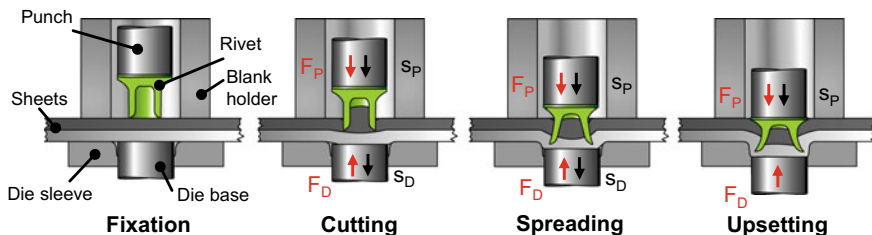
Fig. 10.4 Investigated die kinematic 1 with continuously lowering die base during the joining process
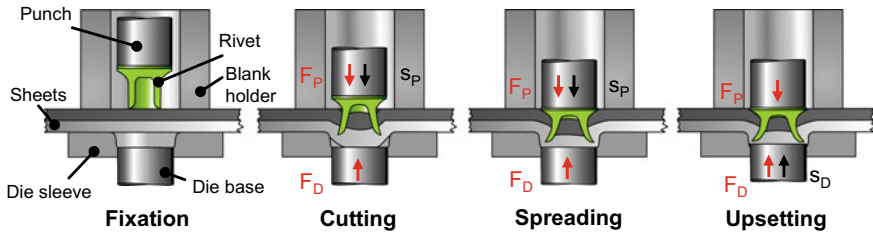
Fig. 10.5 Investigated die kinematic 2 with embossing process after the joint formation

Besides the continuously lowering die base, a post-embossing die base was additionally investigated (Kinematic 2). During the joining process, the die movement is not superimposed on the punch movement. After the joint has been formed, however, the die is driven towards the punch and thus carries out an embossing process. The aim is to increase the interlock formation and the force-fit components of the joint.

Figure 10.6 shows the changes in the quality-relevant parameters as a result of the die kinematics used. It can be seen that an increase in the interlock can be achieved by both kinematics for the pure aluminium joint as well as the multi-material joint. At the same time, the increase of the interlock is accompanied by a negative influence on the minimum die-side material thickness when using a multi-material joint. If kinematic 1 is used, the minimum die-side material thickness can be increased slightly in case of the pure aluminium joint. Especially regarding the multi-material joint, the use of the continuously lowering die leads to a strong decrease of the minimum die-side material thickness. This decreases from approx. 0.6 mm to 0.25 mm. However, the greatest increase in the interlock is also achieved with this joint using kinematic 1, from approx. 0.28 mm to 0.62 mm. This is more than twice as large as in the joint created without die kinematic. It can be assumed that this increase is related to a change in the expansion behaviour of the rivet. The rivet head position is only slightly influenced by both movements. Tendentially, kinematics 2 achieves larger values. This can be explained by the displacement of the material in the direction of the punch as well as the bending of the sheets.

In order to identify the cause-effect relationships between the quality-relevant parameters and the spreading behaviour of the rivet, the study is extended to the investigation of the material flow (Fig. 10.7). For this purpose, the process phases cutting, spreading and upsetting of the semi-tubular riveting process are considered. Since greater effects can be seen within the multi-material joint, this combination is further examined. Shown is the conventional process as well as both kinematics. Kinematic 2 is only visible in the process phase of upsetting, as the contour in the previous phases corresponds to that of the conventional process.

The comparison of the contours shows that the continuous lowering of the die results in a significantly changed material distribution. During the cutting phase, a greater volume of punch-side material is displaced into the rivet shank. At this point, the lowering die base has not released any die volume. Therefore, the punch-sided material can only flow into the shank and in the direction of the free ends of the
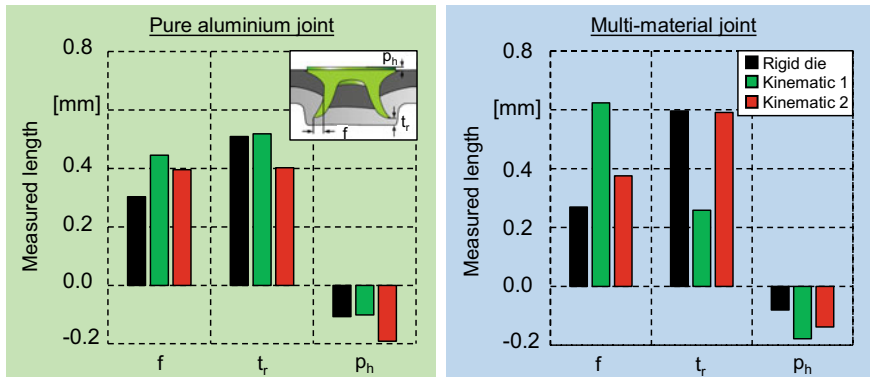
Fig. 10.6 Influence of the die kinematics 1 and 2 on the quality-relevant characteristics of the pure aluminium joint (green) and the multi-material joint (blue)
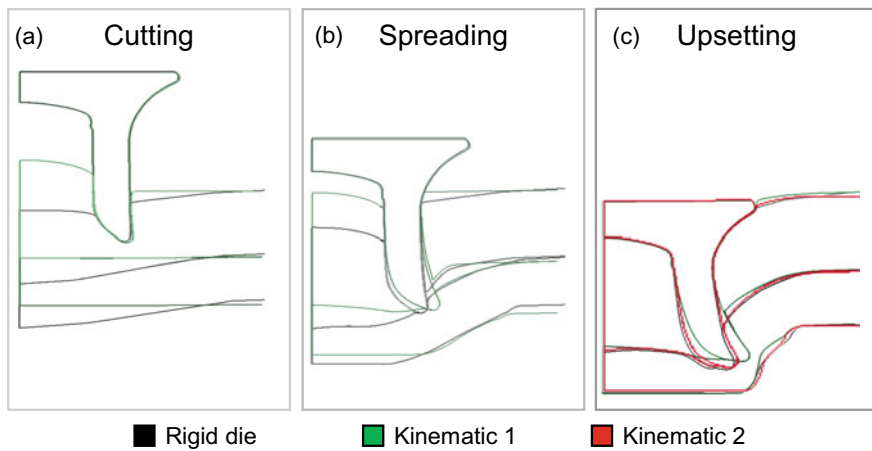
Fig. 10.7 Evaluation of the changed material flow by kinematics 1 and 2 within the three phases of cutting, spreading and upsetting of the multi-material joint (Combination B)

sheets. The lateral material flow also supports the expansion of the rivet at this early stage of the process, as Fig. 10.7a illustrates. When the die volume is released, the material flow into the rivet shank is still increased, as the die-sided joining part is in continuous contact with the die base. The joining zone seems to be superimposed with compressive stresses and the material flow into the shank and in the lateral direction is reinforced. In particular, the lateral material flow supports the spreading of the rivet. In the process phase of upsetting, the significantly increased interlock as well as the relocation of the minimum die-side material thickness to the edge area of the joint, which was already shown in the analysis of the stress and strain distribution, becomes apparent. The filling of the die remains unchanged.
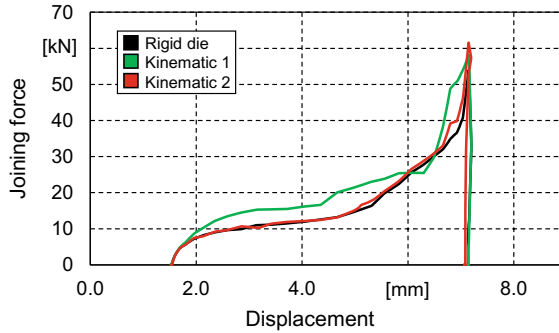
Fig. 10.8 Evaluation of the changes in the force-displacement curve induced by kinematics 1 and 2 within the joining process of Combination B

The changed material flow can also be detected in the plotted force-displacement curves (Fig. 10.8). Due to the induced compressive stresses before lowering the bottom of the die, a higher force is required in the front area of the curve when looking at the curve of kinematics 1. The force for punching through the punch-sided sheet is approx. 5 kN higher than the curve recorded for joining using a rigid die. A higher process force also occurs in the further process phases due to the changed expansion behaviour of the rivet and the increased interlock formation. However, the maximum joining force is at a comparable level at the end of the joining process. The changed kinematics therefore do not seem to have a significant effect on the load on the tools used.

Kinematics 2 shows a comparable curve characteristic compared to the conventional process with a rigid die. In the beginning of the upsetting phase, an increase of the process force is detected. At this point, the kinematics of the die starts to move. Especially at the end of the movement, a significantly increased force is recorded. These consist of the joining force of 55 kN as well as an additional holding force due to the embossing of the die base. The die movement thus causes a significantly higher tool load. Increasing wear as well as the damage of the punch could result.

The changed contour of the kinematics 2 in the upsetting phase (Fig. 10.7c) indicates that the increase of the interlock is mainly caused by a deformation of the auxiliary joining part. This could cause higher stresses within the rivet and lead to cracking and premature failure of the joint. In addition, the process curve suggests that the increased joining forces could lead to a change in stress distribution. For this reason, the simulation model is examined with regard to the occurring stresses, strains and triaxialities.

The investigation of the occurring stress and triaxiality values (Fig. 10.9a and b) shows that by using a continuously lowering die base, large areas of compressive stress are achieved in the base of the die-sided joining part as well as the slug. These are located centrally and decrease towards the sides. This correlation illustrates the supporting spreading effect of the material on the rivet as a result of the kinematics used. The supporting spreading effect is also evident when looking at the effective
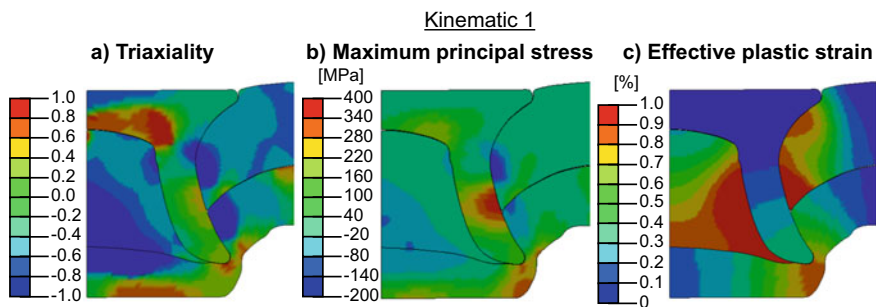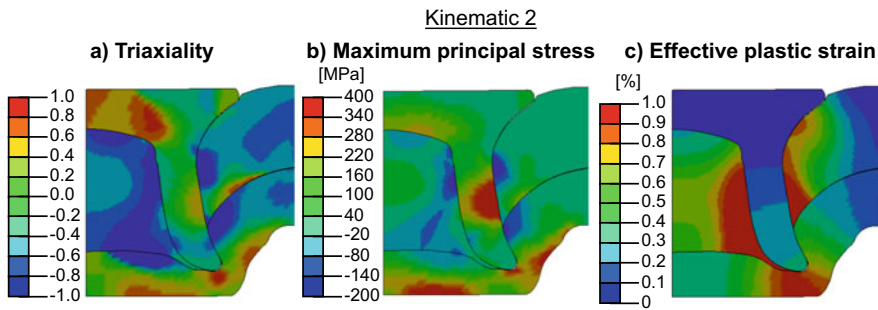
Fig. 10.9 Occurring triaxialities as well as stress and strain distribution when using a continuously lowering die base applied to the used multi-material joint

plastic strain (Fig. 10.9c). These are correspondingly high, especially in the area near the rivet foot. This shows that a considerable amount of material has laterally been displaced and thus supported the rivet during spreading. The deformation in the rivet foot is continuous, so that a compression of the rivet can be excluded. Particularly in the head area of the rivet, increased tensile stress values can be detected. These can be traced back to the rising of the slug as a result of the compressive stresses and the resulting internal pressure. However, the tensile stress values are within an acceptable range.

In the case of kinematic 2, enlarged compression areas can also be identified, which are indicated by the embossing after the joining process (Fig. 10.10). However, these areas are increasingly located in the edge area of the slug. In particular, the consideration of the occurring plastic strains shows that the use of kinematic 2 has led to an increase in the material displacement below the rivet foot. This leads to the reduced minimum die-side material thickness which has been detected above. As already suspected in the section of the material flow, the increase of the interlock can be attributed in particular to the deformation of the rivet foot. The deformation can be explained by both, the higher strain values in the rivet foot area as well as in an increased tensile stress in the outer area of the rivet shank. The use of this kinematics thus leads to an increased rivet load, which might have a negative effect under cyclic load.

10.4   Conclusion

In this investigation, the influence of a movable die base on the joint formation in semi-tubular self-piercing riveting process was examined. For this purpose, a numerical simulation model for a pure aluminium and a multi-material joint of aluminium and steel was set up and validated. The model was modified according to two different die kinematics. On the one hand, the influence of a continuously lowering die base during the joining process was investigated. On the other hand, a post-embossing

Fig. 10.10 Occurring triaxialities as well as stress and strain distribution when using a post-embossing die base applied to the used multi-material joint

through the die base after the joining process was examined. The models were analysed according to the joint formation as well as the resulting stress distribution. Using both kinematics, a significant increase in interlock formation was observed. At the same time, the minimum die-side material thickness decreased, which should be taken into account when implementing and designing the process parameters. In addition to the influence on the quality-relevant characteristics, a change in the occurring triaxiality values as well as the stress and strain distribution during the joint formation could be proven. In particular, increased compressive stresses could be shown within the slug, which support the spreading of the rivet if the kinematic with a constantly lowering die base is used. The improvement of the quality-relevant characteristics with post-embossing die element is mainly achieved by the deformation of the auxiliary joining part. This might have a negative effect on the joint load-bearing capacities. The in-depth investigation of both kinematics with regard to the material flow was able to show the effects occurring in the various process stages. Already at the early stage of cutting, a changed material flow occurred if kinematic 1 is used. The modification of the joint formation could also be shown in the force-displacement curve during the joining process. A higher load on the tools used is not to be expected when the joining process is superimposed by using a continuously lowering die base. The subsequent embossing process results in higher process forces and thus tool loads. This should be taken into account when designing the systems and tools.

References

Böhnke M, Kappe F, Bobbert M, Meschut G (2021) Influence of various procedures for the determination of flow curves on the predictive accuracy of numerical simulations for mechanical joining processes. Mater Test 63:493–500. https://doi.org/10.1515/mt-2020-0082

Commission E (2022) Paris agreement. https://ec.europa.eu/clima/eu-action/international-action-climate-change/climate-negotiations/paris-agreement_de. Accessed 15 June 2022

Donhauser G, Mauermann R, Quaißer G et al (1998) Stamping rivet upsetting tool comprises die endface which is radially divided into sectors outside raised area, (DE19847980 A1)

Drossel WG, Jäckel M (2014) New die concept for self-pierce riveting materials with limited ductility. Key Eng Mater 611–612:1452–1459. https://doi.org/10.4028/www.scientific.net/KEM.611-612.1452

DVS/EFB-Merkblatt 3410 (2018) Merkblatt Stanznieten—Überblick

Kappe F, Schadow L, Bobbert M, Meschut G (2022a) Increasing flexibility of self-piercing riveting by reducing tool–geometry combinations using cluster analysis in the application of multi-material design. Proc Inst Mech Eng Part L J Mater Des Appl 146442072110709. https://doi.org/10.1177/14644207211070992

Kappe F, Wituschek S, Bobbert M, Meschut G (2022b) Determining the properties of multi-range semi-tubular self-piercing riveted joints. Prod Eng 16:363–378. https://doi.org/10.1007/s11740-022-01105-2

Li Y, Wei Z, Li Y et al (2013) Friction self-piercing riveting (F-SPR) of AA6061-T6 to AZ31B. In: Advanced manufacturing, vol 2B. American Society of Mechanical Engineers, pp 1–7

Martinsen K, Hu SJ, Carlson BE (2015) Joining of dissimilar materials. CIRP Ann Manuf Technol 64:679–699. https://doi.org/10.1016/j.cirp.2015.05.006

Meschut G, Matzke M, Hoerhold R, Olfermann T (2014) Hybrid technologies for joining ultra-high-strength boron steels with aluminum alloys for lightweight car body structures. Procedia CIRP 23:19–23. https://doi.org/10.1016/j.procir.2014.10.089

Meschut G, Merklein M, Brosius A et al (2022) Review on mechanical joining by plastic deformation. J Adv Join Process 5:100113. https://doi.org/10.1016/j.jajp.2022.100113

Neugebauer R, Jesche F, Israel M (2010) Enlargement of the application range of solid punch riveting by two-piece dies. Int J Mater Form 3:999–1002. https://doi.org/10.1007/s12289-010-0938-2

Novelis Global Automotive (2019) Datasheet: Novelis Advanz^{TM} 6F—e170; aluminium sheet for exterior applications

OECD (2022) Climate change. https://www.oecd.org/climate-change/. Accessed 28 June 2022

Salzgitter Flachstahl GmbH (2017) Datasheet: HCT590X+Z (HCT600XD/HC340XD*/CR330Y590T-DP**); Mehrphasenstähle zum Kaltumformen—Dualphasenstähle

Chapter 11
Finite Element Analysis to Determine Pull-Out Strength of Fixation Around Large Defect Site in Femur Reconstruction Surgery

Check for updates

Varatharajan Prasannavenkadesan and Ponnusamy Pandithevan

Abstract During the process of bone fracture fixation and reconstruction surgery, bone screws and or fixation plates are used by surgeons. Preliminary experiment showed that the micro-motion of the bone screw leads to loosening and causes the implant to dislocate from its location. Several experimental procedures such as push-in, pull-out, screwing torque and bending tests are used to evaluate the strength of the screw fixation. Although pull-out tests are widely used by researchers, the interaction between the screw fixation and bone surface is largely unexplored until now. This paper aimed at assessing the screw pull-out using homogenized finite element analysis. Owing to the need for longer computational time, screw threads were not considered in most of the finite element analyses done until now. So, it is unclear how different screw types affect the screw–bone interaction. In this paper, finite element analyses were used to compare different types of the screw–bone interfaces. Analyses were performed using buttress and reverse buttress screws, and then the resulting stress distributions around the bone–screw interfaces were analysed. To resemble the actual scenario, screws were pulled out from the bone considering the physiological loading conditions. The obtained results showed that the influence of screw type on stress distribution in the bone-implant interface is significant. As a conclusion, the use of longer screw rods could provide an increased anchoring effect to the fixation device. However, increasing the number of screws potentially cause the stress concentration on the rod which should be take into account. The developed model was also extended to a three-dimensional case study by considering the bone plate, bone screws and the cortical bone. The result obtained from the three-dimensional finite element analysis showed only about 7% error from the experimental counterpart under same conditions.

V. Prasannavenkadesan
Centre for Sustainable Polymers, Indian Institute of Technology Guwahati, Guwahati, Assam 781039, India

P. Pandithevan (✉)
Department of Mechanical Engineering, Indian Institute of Information Technology, Design and Manufacturing Kancheepuram, Chennai, Tamilnadu 600127, India
e-mail: ppthevan@iiitdm.ac.in

11.1 Introduction

In orthopaedics, bone fracture treatment and reconstruction surgery are the two main procedures widely performed. During orthopaedic procedure, surgeons use the bone screws and dynamic compression plate to connect the broken/fractured bone and thus to immobilize it (Bolliger Neto et al. 1999).

As the biomechanical stability of the screws and plates play vital role in the bone healing process, insertion of screws with suitable torque is very much essential (Cleek et al. 2007). It was observed that the regular activities of a person sometimes lead to micro-motion and screw dislocation (Fulkerson et al. 2006). In connection to that, research group conducted experimental tests on human bones and bone surrogates to investigate the dislocation of screws (Zdero et al. 2008; Tankard et al. 2013).

Shelton and Loukota (1996) investigated the pull-out strength on the bovine tibial bone and showed three main reasons for the bone failure, namely cortical thickness and shear strength of the bone and drill bit geometry. It was also revealed that the pull-out failure observed in the maxillo-facial region could be avoided by fixing screws in region where the cortical bone thickness is more.

In the study done by Hou et al. (2004), the holding power of tibial screws on bone was investigated through the experiments and simulation. Low-density polyurethane foams were considered for the experiment, and numerical analysis was performed to determine the reaction force. It was found from their study that the contribution of outer diameter showed significant effect on screw holding power.

Similarly, in the year 2005, Steeves et al. (2005) investigated the influence of pilot hole on pull-out strength of the cancellous screws in the human cadaveric bones. In their study, the authors utilized the femoral and tibial bones and tested using 6.50 mm cancellous screws with pilot holes in the size of 3.20 and 2.50 mm. The mean value based on all the femurs and tibias was reported as 360.60 N when using 2.50 mm diameter pilot holes and 313.50 N when using 3.20 mm diameter pilot holes. It was observed from their study that the use of 2.50 mm pilot hole showed stronger pull-out strength.

In Cleek et al. (2007) study, the authors investigated the effect of screw tightening factor and torque on the screw pull-out strength using ovine tibias. As a procedure, a custom-made test rig was used to calculate the maximum stripping torque. The authors conducted pull-out tests at the levels of 90, 70 and 50% of maximum torque and identified 7–13% decrease in the pull-out strength when using 90% of maximum torque.

In the year 2010, Ricci et al. (2010) investigated the cancellous bone and determined the effect of screw pitch on maximum screw insertion torque and pull-out strength. In that work, stainless steel screws with constant diameter for different pitches were analysed. The study revealed that the effect of screw pitch on maximum screw insertion torque was significant. However, the pull-out strength was not significantly affected by screw thread.

Similarly, Feerick and McGarry (2012) conducted a pull-out study on cortical bone. Two different sets of pull-out experiments, namely one along the direction of osteon alignment and another one perpendicular to the osteon alignment were conducted. Their study concluded that the external force required to pull out the screw in the transverse direction was greater than that of the longitudinal direction.

Study about the reduction in pull-out strength by reinsertion of 3.50 mm cortical screws was conducted by Matityahu et al. (2013). In that study, experimental tests were performed on synthetic bone, human cadaveric diaphyseal tibias, distal tibias and calcanei. From the study, it was concluded that the repeated reinsertion of cortical bone screws could significantly reduce the pull-out strength in both synthetic as well and natural bones.

Liu et al. (2014) investigated the stress distribution and the region of effect during the pull-out tests. Foam material analogous to the cancellous bone was considered for the investigation. The stress distribution and the von Mises stress during the pull-out of pedicle screw were simulated by a numerical method. The pedicle screw of 6.50 mm diameter showed influence of stress over 4.73, 5.06 and 5.40 mm for the bones of ages > 75, 75 > ages > 50 and ages < 50 years old, respectively, which was performed using numerical simulation.

Some researchers investigated the pedicle screw fixations in the lumbar spine (Gupta et al. 2017). But, only very few researchers worked on pull-out strength of fixations used in fracture treatment of femur.

For instance, Varghese et al. (2016) proposed a predictive model for pull-out strength of pedicle screw using polyurethane foam as bone surrogate. However, this model is applicable only for spine surgery. Because of the variation in apparent density of bone, a different model needs to be developed for human femur.

In Gupta et al. (2017) work, the comparison between rotary ultrasonic drilling and conventional drilling was carried out on porcine bones. Their study aimed at the performance of rotary ultrasonic drilling using pull-out tests. Result revealed that the selection of high speed with low feed rate attained lesser bone damage than the other combinations. It was observed that the use of rotary ultrasonic drilling on porcine bones increased the pull-out strength from 55 to 385% compared with conventional drilling.

In Joffre et al. (2017) work, the authors emphasized the complexity in the insertion of screws in bones, especially in the trabecular because of the high porous nature. In that work, 4.0 mm commercial screws were inserted in to the lapine femoral bone. Through μCT, the visualization of the screw pull-out was performed. Stress and strain developed in the bone and the interaction between the screw threads and the bone was investigated. It was reported that the shear strain developed is not only because of the friction, but also dependent on the screw inclination. Similarly, Moser et al. (2017) used synthetic bone to compare the pull-out strength of cortical and cancellous bone screws.

In Shen et al. (2018) work, comparison between the use of bio-absorbable cortical screws and interference screws (BCIS and BIS) on the goat knee was conducted. Their study showed that the cortical interference screws are better than the general

interference screws in the case of femur reconstruction. However, as the density of the goat bone is higher than that of the human bone, the result obtained from their study cannot be directly applied to the human bone without further experiment.

Hu et al. (2021) determined the surface quality and pull-out strength of the holes generated using the ultrasonic drilling process. In their study, the pig cortical femoral bone was used. The authors concluded that the holes drilled using ultrasonic drilling possessed better pull-out strength than the one obtained from conventional drilling process.

In Mejia et al. (2018) study, pull-out strength after multiple reinsertions of self-tapping screws was experimentally evaluated. Their study concluded that, the reinsertions of self-tapping screws showed considerable difference in pull-out strength between first and second reinsertion. But, no significance difference was observed from third insertion to fifth insertions.

Feng et al. (2021) evaluated the pull-out strength and lateral migration resistance of buttress, square and triangular thread screws in polyurethane foam block. But in their study, the apparent density of the bone was not accounted, and thus, the result cannot be directly used for bone.

In Weidling et al. (2022) study, the effect of thread design on anchorage was evaluated. Two factors, namely bone compacting and thread flank area were considered to assess the anchorage of the pedicle screws in cancellous bone. Their study reported that the quality of bone and screw which had high bone compacting possessed a better anchorage.

In this study, a non-invasive method to determine the suitable pull-out strength around the defect site using finite element analysis is proposed. To resemble the actual scenario, a pull-out strength using a compression plate assembled with cortical bone screws was computationally evaluated and then validated with the experiment.

11.2   Materials and Methods

In this study, a method to evaluate the pull-out strength of the fixation was developed using the Ansys® workbench structural module. As a procedure, first a 2D finite element analysis was performed, and then the study was extended to a 3D finite element analysis. Finally, the results obtained from the computational study were compared with the experiments.

11.2.1   Two-Dimensional Finite Element Analysis

For the present study, a two-dimensional axisymmetric model of the bone–screw assembly was developed in Ansys® workbench. Due to high computational time, first, the investigation is limited to a 2D analysis using a 10 mm × 40 mm rectangular bone block. Two different types of screws, namely buttress and reverse buttress were

Table 11.1 Material properties used for the analysis

Sl. No.	Material	Density (kg/m^3)	Young's modulus (GPa)	Poisson's ratio
1	Cortical bone	2000	20	0.28
2	316L steel plate and screw	8000	200	0.30

used, and they were considered as a rigid body as followed in Feng et al. (2021) study. The geometric behaviour was set as axisymmetric, and then the contact between the bone and screw was established. In Table 11.1, the material properties used for the analysis is given.

The discretization of bone and screw were carried out using the program-controlled options at first. Later, meshing with different element sizes was manually performed as an iterative procedure, and then the entire model of the bone–screw assembly was meshed with the linear tetrahedral elements. A region at a distance of around 1.50 mm from the bone–screw interface was meshed again with fine elements using a mesh refinement technique. Based on the mesh-convergence study, a 30 μm sized elements were used to mesh around the screw and bone interface, and coarse mesh was used for the remaining region.

The degrees of freedom at the bottom and side edges of the bone block were arrested in all directions. In reference to the actual scenario, the displacement of the screw was allowed only along the vertical direction. As shown in Fig. 11.1, a point load was applied on the screw head in the vertical direction (Feng et al. 2021). The interaction between the screw and the bone was established with Coulomb's friction law and then the friction coefficient of 0.20 was considered as recommended (Lin et al. 2009).

11.2.2   Three-Dimensional Finite Element Analysis

The finite element analysis of the bone plate pull-out was simulated using Ansys® V18.2. The geometry of the required bone plate, bone and the screws were modelled in the Design Modeler. The material properties provided in the simulation is given in Table 11.1. Throughout the simulation, the isotropic and homogeneous assumption was followed.

The boundary conditions provided to the geometry is shown in Fig. 11.2a. The degrees of freedom on the side faces of the bone block were arrested in all directions. The displacement rate of 5 mm/min to replicate the experimental pull-out test was provided in the simulations. Initially, mesh-convergence study was performed to identify the optimal mesh size. Thus, the minimum element length of 180 μm was used. Totally, 23,374 nodes and 114,492 linear tetrahedral elements were used to mesh the geometry (Fig. 11.2b).
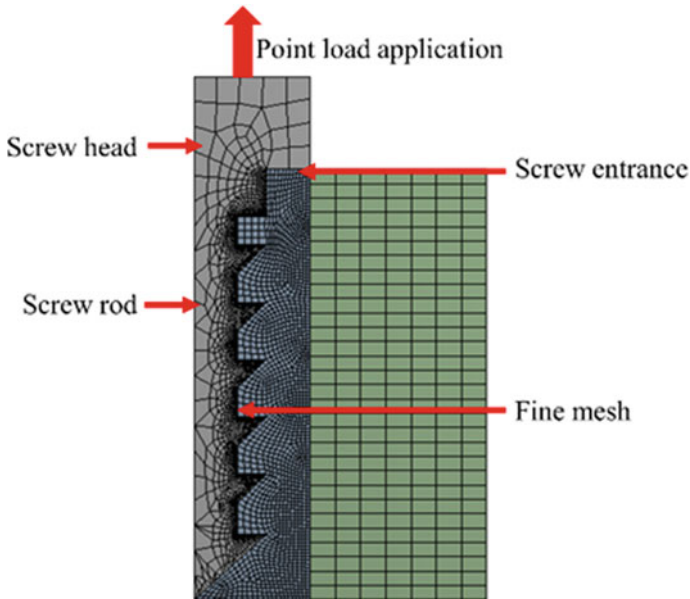
**Fig. 11.1** Meshed model of the screw inserted into the bone

The bone block was considered as two pieces and bonded using the frictional contact to mimic the broken bone considered during experiments. The contact between the screw and the bone was simulated using bonded condition to represent proper adhesion between the implant and the bone. A frictional contact was assumed with between the bottom side of bone plate and the top face of the bone.

11.2.3 Validation Experiments

The experimental setup used to validate the simulation results is shown in Fig. 11.3a. The fractured femur was aligned in position using the compression plate and screws (Fig. 11.3b). This was kept inside a customized fixture (Fig. 11.3c) fabricated for this purpose and clamped in the universal testing machine (UTM).

11.3 Results and Discussions

The stress distribution observed for the different screw types is considered for comparison. In Fig. 11.4, the distribution of the von Mises stress obtained from the finite element analysis is shown. It is evident from the results that the higher
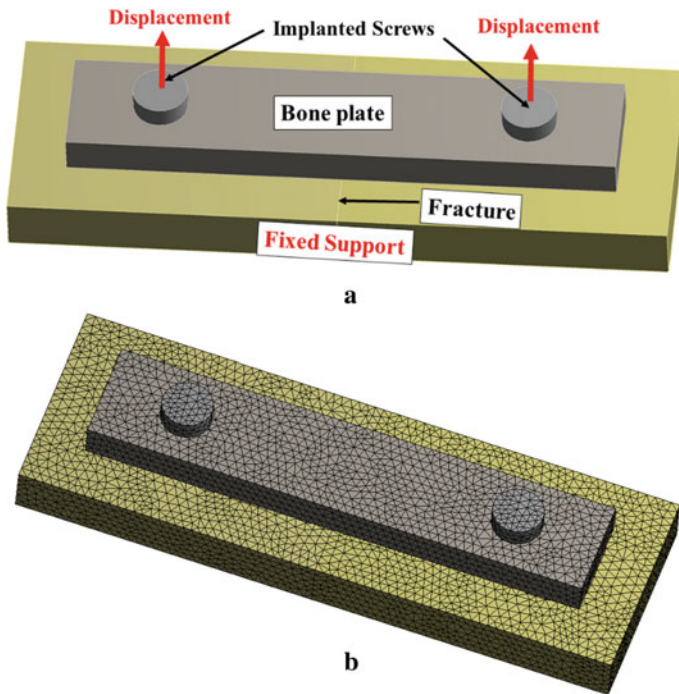
Fig. 11.2 Fracture fixation with plate and screws for pull-out strength **a** loading and boundary conditions and **b** bone block, compression plate and screws meshed for the finite element analysis

stress occurred at the entrance region of the screw. It was observed that the stress distribution is concentrated more on the screw rod. This might be due to the application of point load. From the study, it was clear that the maximum stress values of 34.77 MPa and 34.79 MPa were developed from the buttress and reverse buttress threads, respectively.

Thus, no significant variation in the maximum stress was observed between the different screw types. However, from Fig. 11.4, it is evident that the stress concentration on the screw rod is lesser for the reverse buttress screw. Moreover, the stress concentration is lower in the region away from the applied load. From the simulation results, it is clear that longer screw rod could provide better pull-out strength than the shorter screw rod.

The pull-out simulations were performed at the displacement rate of 5 mm/min applied on the screw head. Figure 11.5 shows the equivalent von Mises stress and overall deformation observed at the end of the simulation. The maximum pull-out force obtained for the considered broken bone was around 885 N. Thus, the simulation showed around a 7% error when compared with the experiment.

It is evident from the results that the stress region is more at the screw shaft and the bone–screw interface. The maximum observed von Mises stress was around
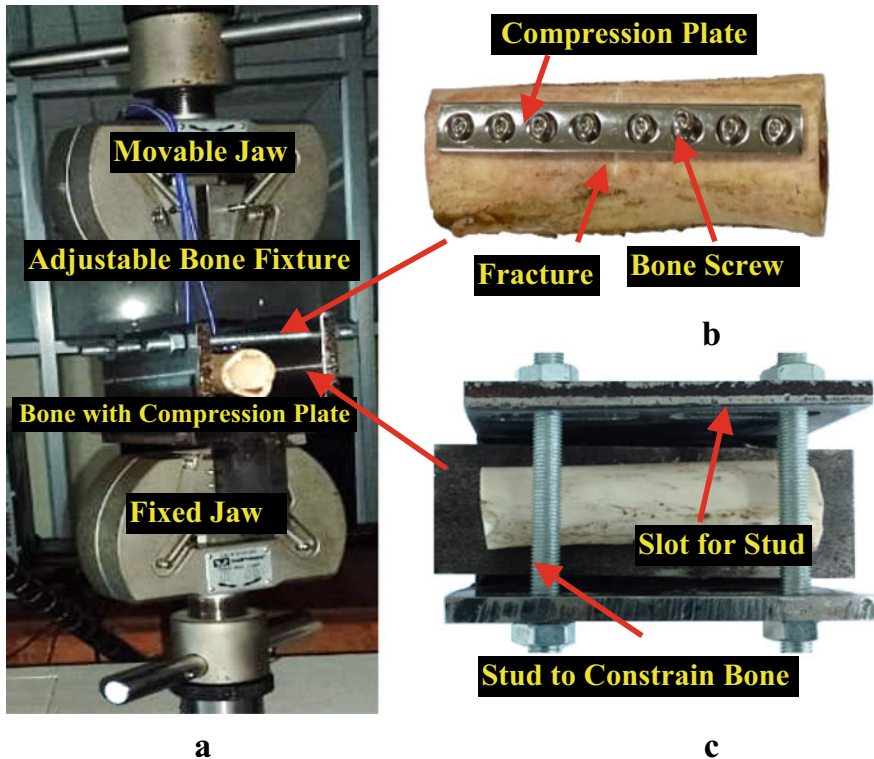
Fig. 11.3 Experimental setup used to conduct the pull-out strength in the Instron® universal testing machine: **a** fractured femur with compression plate and bone screws and **b** bone fixture fabricated to perform pull-out test in the UTM

282 MPa (Fig. 11.5a). It is observed that the pull-out load was transferred from the screw through the bone plate and caused the deformation and dislocation to bone (Fig. 11.5b).

The limitations of the present work are the assumption of homogeneous properties in the finite element model, and linear elastic model used to describe the material behaviour and a simplified 2D approach. So, in future, the authors intend to perform experiments and to develop a finite element model with anisotropic properties to investigate the pull-out process.
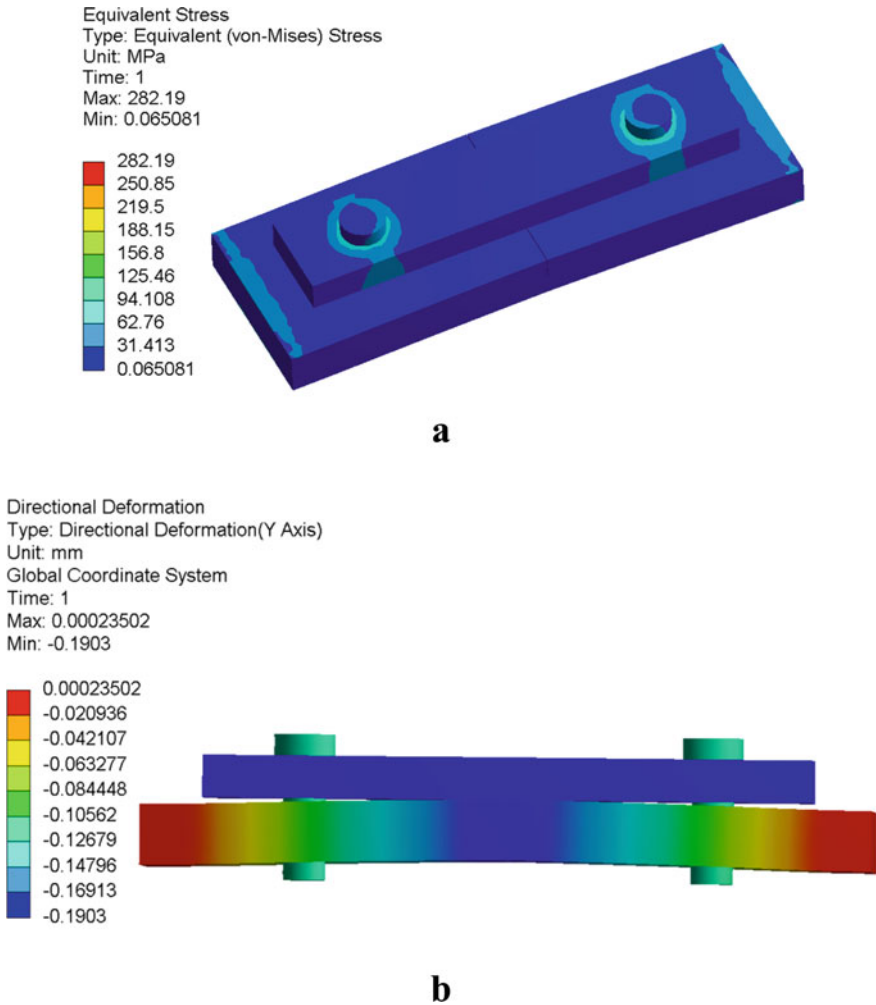
11.4 Conclusions

In this study, finite element analysis to evaluate the pull-out strength of the compression plate fixed through bone using cortical bone–screws was performed. The 2D finite element analysis performed in this study showed a lesser stress distribution for
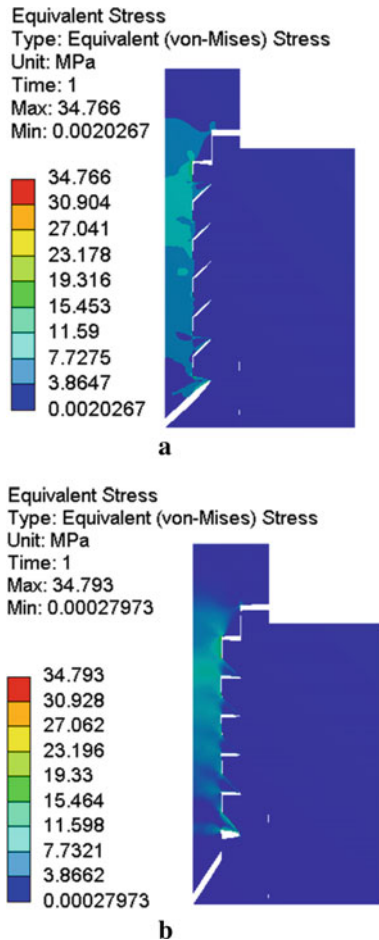
Fig. 11.4 von Mises stress obtained from the finite element analysis conducted for pull-out strength: **a** buttress screw and **b** reverse buttress screw

the reverse buttress screw type than the buttress screw type, under similar conditions. It was drawn from the study that the 3D finite element analysis conducted using the bone-compression plate and screw assembly could potentially predict the pull-out strength as the deviation found in the experimental counterpart was very minimal. In most of the fracture fixation, the purpose of implant fixation is to support the fractured bone and to facilitate the healing process; the computational method used in this study could play a vital role to decide suitable location around the defect site for better pull-out strength. The outcome of the work can be used to investigate the screw geometry, pull-out strength and location of fixation in the *in-silico* environment before performing in-vivo fracture fixation and immobilization procedure.

Equivalent Stress
Type: Equivalent (von-Mises) Stress
Unit: MPa
Time: 1
Max: 282.19
Min: 0.065081

282.19
250.85
219.5
188.15
156.8
125.46
94.108
62.76
31.413
0.065081

a

Directional Deformation
Type: Directional Deformation(Y Axis)
Unit: mm
Global Coordinate System
Time: 1
Max: 0.00023502
Min: -0.1903

0.00023502
-0.020936
-0.042107
-0.063277
-0.084448
-0.10562
-0.12679
-0.14796
-0.16913
-0.1903

b

Fig. 11.5 Results obtained from the pull-out simulation: **a** distribution of von Mises stress and **b** deformation obtained from the analysis

References

Bolliger Neto R, Rossi JD, Leivas TP (1999) Experimental determination of bone cortex holding power of orthopedic screw. Revista Do Hospital Das Clínicas 54(6):181–186. https://doi.org/10.1590/s0041-87811999000600003

Cleek TM, Reynolds KJ, Hearn TC (2007) Effect of screw torque level on cortical bone pullout strength. J Orthop Trauma 21(2):117–123. https://doi.org/10.1097/BOT.0b013e318030261e

Feerick EM, McGarry JP (2012) Cortical bone failure mechanisms during screw pullout. J Biomech 45(9):1666–1672. https://doi.org/10.1016/j.jbiomech.2012.03.023

Feng X, Qi W, Zhang T, Fang C, Liang H, Chen B, Leung F (2021) Lateral migration resistance of screw is essential in evaluating bone screw stability of plate fixation. Sci Rep 11(12510):1–10. https://doi.org/10.1038/s41598-021-91952-3

Fulkerson E, Koval K, Preston CF, Iesaka K, Kummer FJ, Egol KA (2006) Fixation of periprosthetic femoral shaft fractures associated with cemented femoral stems: a biomechanical comparison of locked plating and conventional cable plates. J Orthop Trauma 20(2):89–93. https://doi.org/10.1097/01.bot.0000199119.38359.96

Gupta V, Pandey PM, Gupta RK, Mridha AR (2017) Rotary ultrasonic drilling on bone: a novel technique to put an end to thermal injury to bone. Proc Inst Mech Eng Part H J Eng Med 231(3):189–196. https://doi.org/10.1177/0954411916688500

Hou SM, Hsu CC, Wang JL, Chao CK, Lin J (2004) Mechanical tests and finite element models for bone holding power of tibial locking screws. Clin Biomech 19(7):738–745. https://doi.org/10.1016/j.clinbiomech.2004.04.012

Hu Y, Fan Z, Zhang H, Zhang C, Fu W (2021) Surface quality and pullout strength of ultrasonically-assisted drilling cortical bone. Proc Inst Mech Eng Part H J Eng Med 235(4):378–388. https://doi.org/10.1177/0954411920983662

Joffre T, Isaksson P, Procter P, Persson C (2017) Trabecular deformations during screw pull-out: a micro-CT study of lapine bone. Biomech Model Mechanobiol 16(4):1349–1359. https://doi.org/10.1007/s10237-017-0891-9

Lin D, Li Q, Li W, Swain M (2009) Dental implant induced bone remodeling and associated algorithms. J Mech Behav Biomed Mater 2(5):410–432. https://doi.org/10.1016/j.jmbbm.2008.11.007

Liu S, Qi W, Zhang Y, Wu ZX, Yan YB, Lei W (2014) Effect of bone material properties on effective region in screw-bone model: an experimental and finite element study. Biomed Eng Online 13(1):83. https://doi.org/10.1186/1475-925X-13-83

Matityahu A, Hurschler C, Badenhop M, Stukenborg-Colsman C, Waizy H, Wentz B, Marmor M, Krettek C (2013) Reduction of pullout strength caused by reinsertion of 3.5-mm cortical screws. J Orthop Trauma 27(3):170–176. https://doi.org/10.1097/BOT.0b013e31825490b1

Mejia A, Solitro G, Gonzalez E, Parekh A, Gonzalez M, Amirouche F (2018) Pullout strength after multiple reinsertions in radial bone fixation. Hand 15(3):393–398. https://doi.org/10.1177/1558944718795510

Moser JE, Kunkel KA, Gerard PD (2017) Pullout strength of 2.0 mm cancellous and cortical screws in synthetic bone. Vet Surg 46(8):1110–1115. https://doi.org/10.1111/vsu.12692

Ricci WM, Tornetta P III, Petteys T, Gerlach D, Cartner J, Walker Z, Russell TA (2010) A comparison of screw insertion torque and pullout strength. J Orthop Trauma 24(6):374–378. https://doi.org/10.1097/BOT.0b013e3181c4a655

Shelton JC, Loukota RA (1996) Pull-out strength of screws from cortical bone in the maxillo-facial region. J Mater Sci Mater Med 7(4):231–235. https://doi.org/10.1007/BF00119736

Shen XZ, Qu F, Li CB, Qi W, Lu X, Li HL, Guo Q, Wang JT, Zhao G, Liu YJ (2018) Comparison between a novel human cortical bone screw and bioabsorbable interference screw for graft fixation of ACL reconstruction. Eur Rev Med Pharmacol Sci 22(1 Suppl):111–118. https://doi.org/10.26355/eurrev_201807_15372

Steeves M, Stone C, Mogaard J, Byrne S (2005) How pilot-hole size affects bone-screw pullout strength in human cadaveric cancellous bone. Can J Surg 48(3):207. 16013624

Tankard SE, Mears SC, Marsland D, Langdale ER, Belkoff SM (2013) Does maximum torque mean optimal pullout strength of screws? J Orthop Trauma 27(4):232–235. https://doi.org/10.1097/BOT.0b013e318279791f

Varghese V, Ramu P, Krishnan V, Kumar GS (2016) Pull out strength calculator for pedicle screws using a surrogate ensemble approach. Comput Methods Programs Biomed 137:11–22. https://doi.org/10.1016/j.cmpb.2016.08.023

Weidling M, Heilemann M, Schoenfelder S, Heyde CE (2022) Influence of thread design on anchorage of pedicle screws in cancellous bone: an experimental and analytical analysis. Sci Rep 12:8051. https://doi.org/10.1038/s41598-022-11824-2

Zdero R, Olsen M, Bougherara H, Schemitsch EH (2008) Cancellous bone screw purchase: a comparison of synthetic femurs, human femurs, and finite element analysis. Proc Inst Mech Eng Part H J Eng Med 222(8):1175–1183. https://doi.org/10.1243/09544119JEIM409